Max-Planck-Institut für Polymerforschung

Exzellenz-Graduiertenschule "Materials Science in Mainz" (MAINZ)

Ultrafast Carrier Dynamics in Quantum Dot Sensitized Systems

Dissertation

zur Erlangung des Grades

“Doktor der Naturwissenschaften”

am Fachbereich Chemie, Pharmazie und Geowissenschaften der

Johannes Gutenberg-Universität in Mainz

Mainz, 2016

Hai Wang

Geboren in Yunnan province, China

Dekan: Prof. Dr.

1. Berichterstatter:

2. Berichterstatter: Prof. Dr.

Tag der mündlichen Prüfung: 19/02/2016

Die vorliegende Arbeit wurde in der Zeit von 01/2012 bis 12/2015 im Max-Planck-Institut für Polymerforschung in Mainz unter der Betreuung von Dr. und Prof. Dr. durchgeführt.

知之为知之，不知为不知，是知也！ -论语

“When you know a thing, to recognize that you know it;

and when you do not know a thing, to recognize that you do not know it.

That is knowledge!

-Analects of Confucius, translated by Arthur Waley

Table of Contents

Abstract

In spite of their potential, photovoltaic-based energy sources currently represent only a tiny fraction of current global energy sources a t the moment.. To change this status quo, it is necessary to achieve low-cost, high-efficiency solutions for the direct conversion of sunlight into electricity. *Quantum dot-sensitized solar cells (QDSSCs) represent a promising low-cost photovoltaic technology that has demonstrated a sharp rise in efficiency performance in the past decade. Despite these efforts, the <10% efficiency of current QDSSCs designs is still too low to be competitive with established technologies.*

The work included in this thesis is dedicated to identify, understand and potentially overcome the constraints limiting QDSSC device efficiencies. The primary focus of this work is to elucidate the very first step following absorption of photons: we focus primarily on unveiling the nature and tuning of interfacial electron transfer (ET) processes from the quantum dot (QD) sensitizer towards the mesoporous oxide electrode. The charge carrier dynamics at the QD-sensitized oxide interfaces is primarily investigated by femtosecond time-resolved optical-pump terahertz-probe spectroscopy. The results discussed and summarized in this thesis have revealed new pathways in order to boost efficiencies of QDSSCs by targeting: (i) improvements in the device's open circuit voltages (V_{OC}) by reducing thermal energy losses at QD/oxide interfaces and in the QDs themselves; (ii) improvements in short-circuit currents (J_{SC}) by suppressing trapping processes in QD/oxide electrodes. Specifically, for reducing energy losses from thermalization processes, several novel strategies have been proposed and tested in this thesis, including *enhancing the donor-acceptor coupling strength (chapter 3)*, reducing interfacial donor-acceptor energetics by dipolar capping at QD surfaces (chapter 5), multiexciton generation and collection (chapter 6), and interfacial extraction of hot carriers (chapter 7). From a kinetic point of view, all of these strategies share a common aspect: boosting the coupling strength between the quantum dot and the oxide is shown to represent a key characteristic of high-performance devices. *On the other hand, for boosting J_{SC} in QDSSCs, we have shown that atomic (chapter 4) and organic ligand* (chapter 5) *passivation of QDs* are both suitable for boosting QDSSCs performance. Atomic passivation can be r*eadily achieved via stoichiometric control in QDs;* ligand passivation is enabled, and tunable by the rich functionality of organic molecules (dipole moment etc.). These different approaches bring new design principles for optimizing charge transfer dynamics at QD/oxide interfaces.

In summary, the results discussed within this thesis contribute to a better understanding of interfacial charge transfer dynamics in sensitized systems; furthermore several novel design principles for boosting the power conversion efficiency in QDSSCs were analyzed and discussed herein.

Zusammenfassung

Trotz ihres Potentials stellen Energiequellen, die auf Photovoltaik basieren, derzeit nur einen winzigen Bruchteil der global genutzten Energiequellen. Um diesen Status quo zu ändern, ist es notwendig, kostengünstige und hocheffiziente Lösungen für die direkte Umwandlung von Sonnenlicht in Elektrizität zu entwickeln. Quantenpunktsensibilisierte Solarzellen (QDSSCs) stellen eine vielversprechende kostengünstige Photovoltaik-Technologie dar, die innerhalb der letzten zehn Jahre einen starken Anstieg in ihrer Effizienz gezeigt haben. Trotz dieser Bemühungen ist die Effizienz der gegenwärtigen QDSSCs Designs mit <10% immer noch zu niedrig, um gegen etablierte Technologien wettbewerbsfähig zu sein.

Diese Doktorarbeit beschäftigt sich damit die Grenzen der QDSSC-Effizienz zu identifizieren, sie zu verstehen und zu zeigen, wie sie möglicherweise sogar zu überwinden sind. Der Schwerpunkt dieser Arbeit liegt auf den Prozessen, welche sich direkt an die Absorption von Photonen anschließen: Wir konzentrieren uns primär auf die Art des Elektronentransferprozesses (ET), der sich an der Grenzfläche von Quantenpunktsensibilisator und mesoporöser Oxid-Elektrode abspielt und wie dieser justiert werden kann. Die Ladungsträgerdynamik an den quantenpunktsensibilisierten Oxidgrenzflächen wird hauptsächlich durch optische Pump- Terahertz-Spektroskopie mit Zeitauflösung im Femtosekundenbereich untersucht. Die in dieser Arbeit diskutierten und zusammengefassten Ergebnisse zeigen neue Wege auf, um die Effizienz von QDSSCs zu steigern, durch: (i) Verbesserungen in der Leerlaufspannung des Geräts (V_{OC}) durch Reduktion thermischer Energieverluste an den Quantenpunkt (QD)/Oxidgrenzflächen und in den QDs selbst; (ii) die Verbesserung der Kurzschlussströme (J_{SC}) durch die Unterdrückung von Einfangprozessen in den QD/Oxid-Elektroden. Insbesondere werden in dieser Arbeit mehrere neue Strategien zur Verringerung von Energieverlusten aus Thermalisierungsprozessen, einschließlich der Verbesserung der Donor-Akzeptor-Kopplungsstärke, vorgeschlagen und getestet (Kapitel 3), der Verringerung der Donor-Akzeptor-Energetik an Grenzflächen durch dipolares Capping von QD Oberflächen (Kapitel 5), der Generierung und Extraktion von Multi-Exzitonen (Kapitel 6), und Extraktion heißer Ladungsträger (Kapitel 7). Aus kinetischer Sicht haben alle diese Ansätze eine Gemeinsamkeit: die Steigerung der Kopplungsstärke zwischen Quantenpunkt und Oxid stellt ein wesentliches Merkmal von Hochleistungsgeräten dar. Andererseits, um den J_{SC} in QDSSCs zu steigern, haben wir gezeigt, dass die Passivierung von QDs sowohl mit atomaren (Kapitel 4) als auch organischen Liganden (Kapitel 5) für die Leistungssteigerung der QDSSCs geeignet ist. Atomare Passivierung kann leicht über die stöchiometrische Kontrolle in QDs erreicht werden; anpassbare Liganden-Passivierung kann durch die reichen Funktionalität von organischen Molekülen (Dipolmoment etc.) erreicht werden. Diese

unterschiedlichen Ansätze zeigen neue Design-Prinzipien für die Optimierung der Ladungstransferdynamik an den QD/Oxid-Grenzflächen.

Zusammenfassend tragen die im Rahmen dieser Arbeit diskutierten Ergebnisse zu einem besseren Verständnis der Ladungstransferdynamik an Grenzflächen von sensibilisierten Photovoltaik-Systemen bei; außerdem wurden mehrere neuartige Konstruktionsprinzipien für die Steigerung des Energieumwandlungseffizienz in QDSSCs analysiert und diskutiert.

Chapter 1 Introduction

The global energy consumption is increasing in proportion with the world population expansion. At present, the world energy supply is mainly based on burning fossil fuels (oil, coal and natural gas); energy sources that are non-renewable and non-sustainable. Moreover, emissions of harmful byproducts when consuming fossil fuels have caused many environmental issues. One of the most concerning examples is the scientifically established relationship between CO_2 emissions and global warming.[1-3] Within this pressing scenario, searching for novel cost-effective, abundant and environmentally friendly energy sources for sustainable development represents a great challenge worldwide.

According to "*World Energy Assessment Report: Energy and the Challenge of Sustainability*" from the United Nations in 2003*, the total energy contained in one hour of solar radiation incident on the earth could already fulfill our yearly global energy consumption demand. Much scientific effort has been spent during the last 5 decades attempting to harness efficiently the energy from the sun. While the sun is the source of many renewable energies, e.g. wind energy, hydroelectric power, biomass energy and non-sustainable such as fossil fuels. In principle, the direct conversion of solar energy into electricity represents a unique way to harness solar radiation without intermediate steps. Unfortunately, the efficiency/costs ratio for solar cells at present is not competitive yet with current energy supply technologies regarding exploiting fossil fuels. In this respect, substantial advances to reduce costs and increase efficiency for photovoltaic applications are necessary for the realization of an era based on clean and limitless solar energy.

* http://www.undp.org/content/undp/en/home/librarypage/environment-energy/sustainable_energy/world_energy_assessmentenergyandthechallengeofsustainability.html

1.1 Solar cells: loss mechanisms and Shockley-Queisser limit

In this thesis, we will focus our discussion on the development of solar cells: a photovoltaic (PV) device converting solar energy directly into electricity. Normally, solar cells are made out of semiconductors: a type of materials which combines a good absorption and good conduction for photogenerated charges. When a semiconductor is illuminated by sunlight, an electron from the valence band (VB) can be promoted to the conduction band (CB), leaving a hole behind in the VB. As the binding energy of excitons in inorganic semiconductors is normally lower than the thermal energy[4], photogenerated electrons and holes appear as the free charges. To harvest these free charges for producing electricity, it is mandatory that electrons and holes move in opposite directions within the device, and this can be achieved by p/n junctions (a junction between 2 semiconductors with an excess of holes and electrons respectively). Away from the p/n junction the free charges can move by drift to the metal contacts. By connecting the metal contacts between the electron and hole side of the solar cell through an external circuit, electricity can be generated.

Understanding the fundamental limits defining energy conversion efficiency of a PV device is essential. Independently on the chemical and geometrical design of the solar cell, two loss mechanisms are commonly shared in all solar cells consisting of a single junction: the transmission loss and thermal energy loss.

***(1) Transmission loss*:** Absorption of sunlight is the first key step for an efficient photo-conversion process. In figure 1 (A), the solar irradiation spectrum reaching earth surface is shown. As we can see, although sunlight intensity peaks at visible range, the infrared energies (> 800 nm) represent a substantial portion of the solar spectrum. In order to achieve an efficient absorption in the active layer for solar cells, a good match between available solar radiation at earth surface and the materials' bandgap is a requirement. As sunlight hits in the solar cells, only photons with energies that are above the bandgap energy (E_g) can excite an electron from valence band (VB) to generate free charges. On the other hand, photons with energy lower than the bandgap will be transmitted through, not contributing to the solar power conversion process. As depicted in figure 1(B), for solar cell based on a wide bandgap semiconductor (*e.g.* E_g >3 eV), absorption of sunlight is inefficient: only high-energy photons at the blue side of the solar spectrum are absorbed, and sunlight from the red portion of the solar spectrum is totally lost. This is in contrast to the case of narrow bandgap semiconductors (*e.g.* with E_g <1 eV), in which absorption can start from the infrared side of the spectrum (see illustration in figure 1.1 (C), allowing for strong absorption and thus potentially high current density (J_{SC}) in the cells.

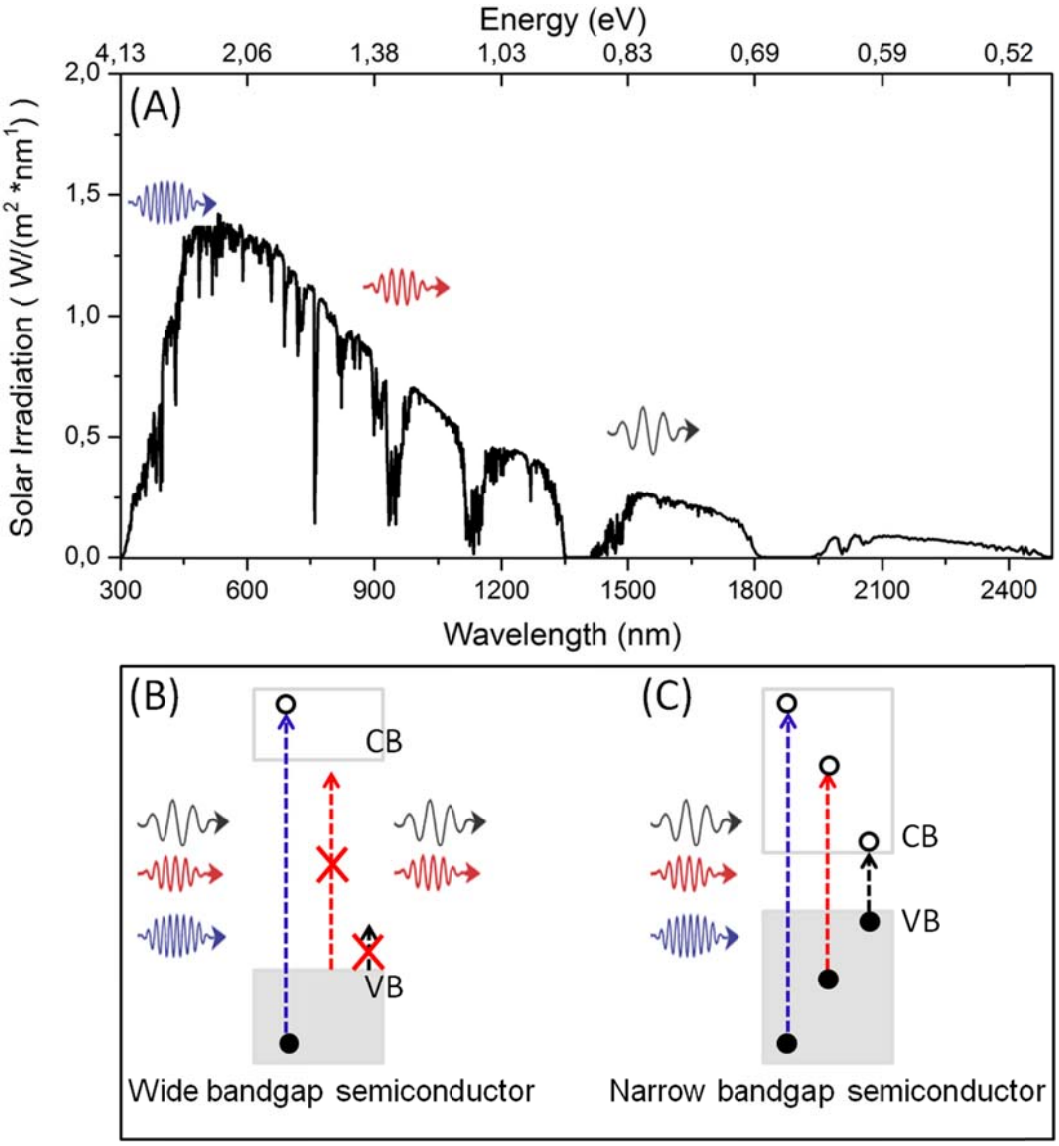

Figure 1.1 (A) Solar irradiation spectrum at earth surface. Data are adapted from PV EDUCATION.ORG at: *http://www.pveducation.org/pvcdrom/appendices/standard-solar-spectra*. (B) The sub-bandgap transmission of solar radiation for the case of a wide bandgap semiconductor as a major loss in a solar cell. Three resonances (with arrows) represent light with different frequencies, and the vertical dashed lines indicate the corresponding photon energies. (C) The case of a narrow bandgap semiconductor.

(2) Thermal energy loss: After photoexcitation of a semiconductor with photon energies larger than the bandgap leads to the generation of the so-called "hot carriers" with excess energy (E_{ex}).[5, 6]. Subsequently, the system relaxes towards thermal equilibrium by the cooling of hot carriers, via multiple electron-phonon scattering processes[7-9] (as depicted in figure 1.2) within characteristic ultrafast timescales of ~1 eV/ps. This hot cooling process is also called thermalization or hot carriers relaxation in the literature. After thermalization, the excess energy in hot carriers is lost as heat. Fundamentally the bandgap of the materials determines the carrier energies and the open circuit potential (V_{OC}) of a solar cell.

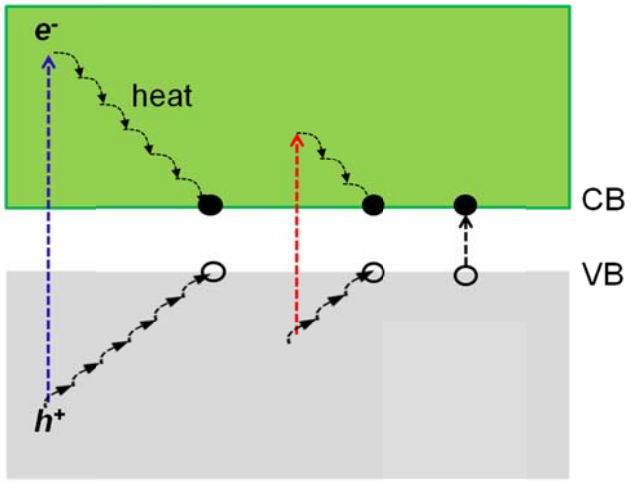

Figure 1.2 An illustration of the process of thermalization in a semiconductor. Three vertical dashed lines refer to excitations with different excess energies above the bottom of the CB (for electrons) or below the top of the valence band (for holes).

While solar cells based on narrow band gap semiconductors, show a characteristic combination of a low V_{OC} (due to the thermal energy loss) and high J_{SC} (owing to high absorption), in the case of wide band gap semiconductors a combination of a low J_{SC} with a high V_{OC} is expected for the same reasoning. Therefore, empirically an intermediate bandgap for balancing the absorption loss and thermalization lose is expected to give the optimized power conversion efficiency.

For a precise prediction of solar cell efficiencies for materials with different bandgaps, factors other than the fundamental loss mechanisms discussed above such as black body radiation and radiative recombination, have to be taken into account.[10, 11] In 1961, Shockley and Queisser determined the theoretical efficiency of a solar cell by the detailed balance arguments, as a function of the semiconductor bandgaps.[10] According to this so-called Shockley-Queisser (S-Q) limit, the highest power conversion efficiency of a single junction solar cell is ~33%, and can be realized at materials with a bandgap of ~ 1.35 eV. As illustrated in figure 1.3, the theoretical efficiency of Si based PV devices (with a bandgap ~1.11 eV) is ~31%. State-of-the-art Si solar cells in research labs can reach efficiencies as high as ~25%; approaching S-Q limit and demonstrating the maturity of Si PV technology. However, PV devices with such high efficiency are based on high quality single crystal Si which is expensive to produce. For the further development of Si-based PV technology, reduction of production costs is an ongoing effort.

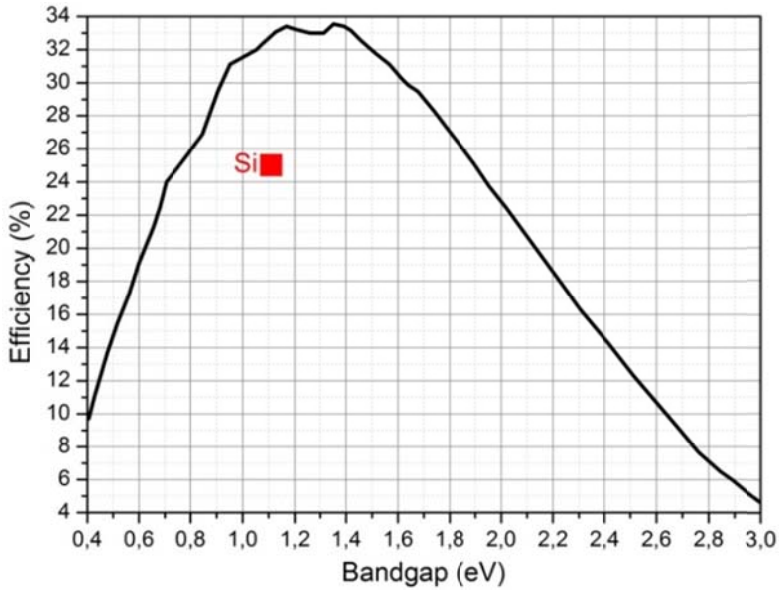

Figure 1.3 Shockley-Queisser (S-Q) limit (adapted from [10]) in one sun conduction and recorded efficiency for Si according to the chart of "Research Cell Efficiency Records" from National Renewable Energy Laboratory (NREL) (http://www.nrel.gov/ncpv/)

1.2 Quantum dot sensitized solar cells: basic principles and their Shockley-Queisser limit

Alternatively, cost-efficient PV systems could also be realized by increasing the efficiency of solar cells based on cheap materials. In this respect, the recent research focus on room T-solution processed solar cells represents a promising path towards reducing the cost of producing solar power. As one of the most promising candidates, colloidal quantum dots (QDs) employed as absorbers are currently under investigation for energy conversion applications. Quantum dots possess appealing electronic and optical properties that are suitable for solar cell applications, such as size dependent electronic and optoelectronic properties along with strong light absorption and emission.[12]

1.2. 1 A brief introduction to semiconducting quantum dots

Quantum dots are semiconducting nanocrystals with typical diameters of 2-10 nanometers. The size dependent properties of QDs are a consequence of strong physical confinement of excitons imposed by the boundary of the particle. In a bulk semiconductor, if excitons are formed after photoexcitation, the physical separation between the electron and the hole is a natural length, the so called Bohr radius. When the size of semiconductor nanocrystal is smaller than the Bohr radius, excitons are constrained

by the physical boundary. The effect of such confinement to the kinetic energy in the very small dot can be simply understood though de Broglie equation:

$E = \frac{p^2}{2m} = \frac{(\frac{h}{\lambda})^2}{2m} = \frac{h^2}{2m*\lambda^2}$, Equation 1.1,

in which p is the momentum, λ the wavelength, m the effective mass of charges and h as the Planck constant. For a given dot with diameter R, the electronic wavelength in the dot can only take a discrete number of wavelengths by considering the boundary condition of a standing wave:

$R = n * \lambda,\ n = 1, 2, 3 \ldots \ldots \ldots$, Equation 1.2

By combining equation 1.1 and 1.2, finally one can obtain:

$E = \frac{h^2*n^2}{2m*R^2}$, Equation 1.3

Although equation 1.3 is rather simple, it contains the essence of the confinement effect in QDs. According to equation 1.3, the energy levels in these "quantum dot" are discrete, in analogy to the electronic orbitals in a single atom. As a result, QDs are often seen as an "artificial atoms". For a more accurate theoretical calculation of the size dependent bandgap, other factors besides the confinement effect such us Coloumbic interactions between electrons (e) and holes (h) have to be considered.

$$E_g\,(\mathrm{QD}) = E_g(bulk) + E_{confiment\ for\ e} + E_{confiment\ for\ h} - E_{e-h}$$
$$= E_g(bulk) + \frac{h^2}{2*R^2}\left(\frac{1}{m_e} + \frac{1}{m_h}\right) - \frac{1.8}{\varepsilon*R}, \quad \text{Equation 1.4}$$

In which, E_g (QD) and $E_g(bulk)$ are the bandgaps of the quantum dot and bulk counterpart, m_e and m_h the effective masses for electrons and holes respectively, ε the dielectric constant for quantum dots.[13] As we can see from equation 1.4, with decreasing QD size, the confinement energies (scaling with $1/R^2$) dominate over Coloumbic interactions (scaling with $1/R$): i.e. the smaller the size, the larger of the bandgap. As a result, the bandgap of quantum dots shifts to blue in energy with decreasing size, as shown in the figure 1.4 (A) (CdSe quantum dots ranging from 2.3 to 3 nm as an example). The corresponding electronic structural changes are depicted schematically in figure 1.4 (B). Owing to their "artificial atom" nature, the first two electronic transitions in QDs are labeled as 1S and 1P orbitals, in analogy to the electronic transitions in atoms.

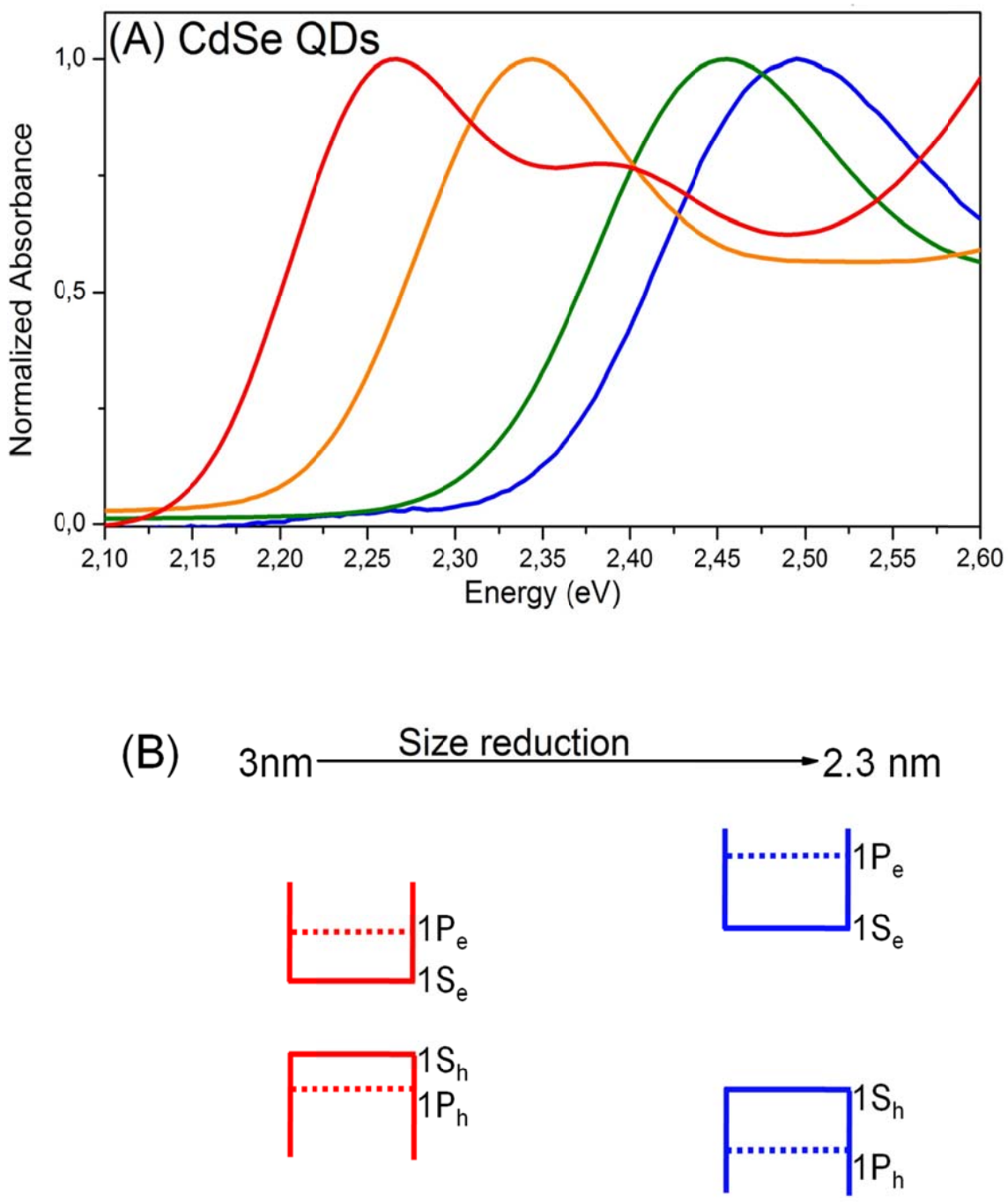

Figure 1.4 (A) Absorption spectrum of 4 different sizes of CdSe QDs (from 2.3nm to 3.0 nm) normalized to the first excitonic peak illustrating quantum confinement effects. (B) Schematic band structure changes with decreasing the size of QDs.

1.2. 2 Quantum dot sensitized solar cell

The size-dependent electronic and optical properties of QDs are by far the most appealing aspects for many optoelectronic applications based on QDs. For instance, light-emitting technologies based on QDs have been developed owing to their tunable size dependent emission.[14-18] For solar cells, such size tunability of QD electronic properties can be applied for material bandgap optimization to match the solar spectrum, making QDs extremely attractive absorbers for solar energy conversion.

After photoexcitation, efficient extraction of electrons from QDs is a pre-requirement for energy conversion applications, and can be achieved by a sensitization protocol stemming from the concept of dye sensitized solar cells (DSSCs).[19] DSSCs were introduced by Grätzel's group in the early 90's as a potential route for developing highly efficient, low cost photovoltaic devices. Owing to the high porosity of nanostructured TiO_2 film, a high loading of the sensitizer is possible thus resulting in large absorption of sunlight. Under illumination conditions, dyes are exploited as sensitizers for light absorbing to generate excitons. The excitons are further separated by injecting of electrons into nanostructured wide bandgap oxide particles (eg. TiO_2, SnO_2, ZnO, process 1 in the figure 5(A)), and by transferring hole into a hole-conducting material (*e.g.* the iodide electrolyte[19], process 3).[20-22] Subsequently, the separated electrons and holes are collected at electrodes and recombined in the external circuits to generate electricity. Owing to the excellent optical properties of QDs (strong absorption cross sections[12, 23-25], *etc*.), they have been considered as promising candidates for replacing the dyes. Sensitized solar cells based on QDs were proposed back to early 90s.[26, 27] The general working principle of sensitized solar cells based on QDs is similar to that based on dyes. In the last decade, considerable effort has put into optimizing QDSSC fabrication. However, the highest reported power conversion efficiency of quantum dot sensitized solar cells (QDSSCS) is still modest ~8.5%[28] when compared to >12% for DSSCs.[29] In this respect, understanding and minimizing efficiency losses associated with the charge transfers at different interfaces (QD/oxide, QD/electrode etc.), and charge transport at different electrodes are essential for boosting efficiency of QDSSCs, to be competitive to their dye counterparts. In the following, charge transfer/transport processes and their corresponding recombination mechanisms that limit the cell performance in QDSSCs will be discussed with some more details.

(1) Electron transfer (ET) from QD to oxide interfaces

Electron transfer from sensitizer to oxide interface is one of the most important steps in quantum dot sensitized solar cells (QDSSCs) as it is the first key process for efficient exciton dissociation. In figure 1.5 (B), we show the energetics and possible charge transfer dynamics at QD/oxide interfaces. In principle, after photoexcitation, electron transfer dynamics from the LUMO states of QDs to oxides can be described as ET between a discrete molecular state in the donor to dense conduction band states

in the acceptor.[30] ET largely depends on interfacial energetics, and can occur only if the conduction band (CB) of the oxide is lower than that the positions of QD excited states where injection takes place. This energy difference between these 2 states involved in ET (ΔG), acts as the driving force for ET: the bigger the ΔG, the faster the ET rate (i.e. higher efficiency of electron extraction).[31] However, accompanying ET, ΔG represents also a channel of thermal energy loss in the cell. Therefore a detailed balance between efficient charge harvesting and corresponding thermal energy consumption (ΔG) needs to be considered in the solar cell design. One of the main *focuses in this thesis is the fundamental understanding of how to control the electron transfer efficiency and minimize the thermal energy loss during ET to improve the power conversion efficiency of QDSSCs.*

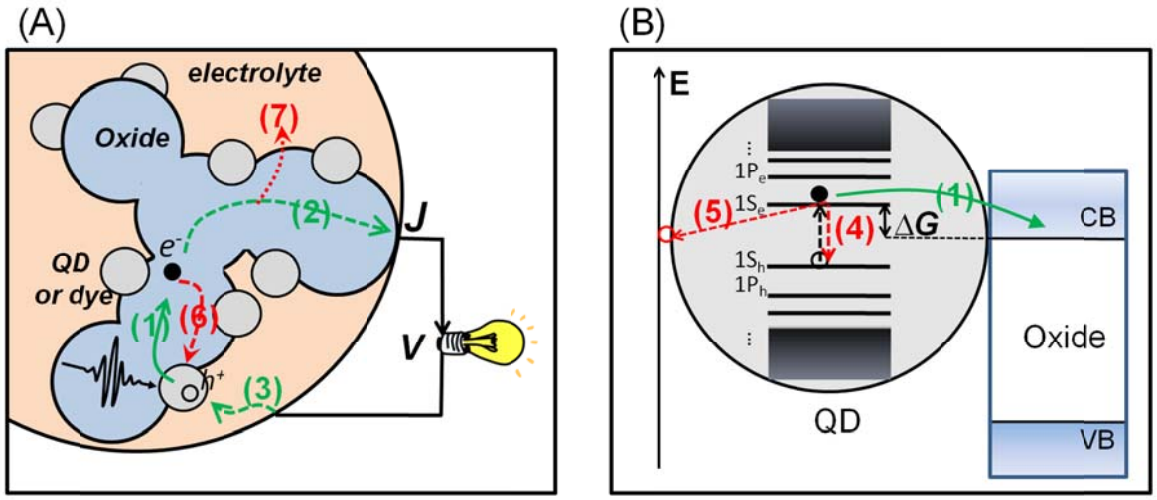

Figure 1.5 (A) schematic representation of the working principle for Quantum dot/dye sensitized solar cells. Green arrows indicate the desired direction of current flow in cells (processes 1-3), and red arrows show the loss mechanism owing to various sources of recombination (processes 4 and 5); (B) a zoom-in energetics at the QD/oxide interfaces.

Generally, extraction of photo-generated electrons in sensitizers to oxide acceptors needs to be sufficiently fast to effectively compete with recombination processes to achieve high solar energy conversion efficiency.[32] At QD/oxide interfaces, radiative recombination (process 4 in figure 1.5 (B), ns life time[33-35]) and, ultrafast surface trapping (process 5, in the timescale of ps[36]) can be operative, and both processes are detrimental to the currents (J_{SC}) in the cells. Achieving efficient surface passivation in quantum dot (QD) nanocrystals is therefore mandatory towards their practical implementation in QDSSCs.[28] Capping semiconducting nanocrystals with molecular shells[37-39], inorganic layers[28, 40, 41], or just atoms (e.g. by stoichiometry control[42-44]) have proven as accessible approaches for the passivation of non-radiative relaxation paths at QD surfaces, and these will be discussed later in section 1.3.1.

(2) Electron transport in the film of TiO_2 nanoparticles is mediated by diffusion towards the back contact.[45] On the way towards the metal electrode, charge recombination processes at QD/oxide, oxide/electrolyte can be active. At the QD/oxide interfaces, injected electrons can recombined with the hole left in sensitizer, a process we call "*back electron transfer (BET)"* in this thesis; shown in figure 1.5 (A) as process 6. Another detrimental interfacial recombination exists between electrons in *oxide and holes in electrolyte,* illustrated as process 7 in figure 1.5(A). For regenerating of QDs by electrolyte, holes are transferred from QDs to electrolyte and further transport towards the counter electrode. As oxide surfaces are intimately contacted with electrolyte, such interfacial recombination can be very efficient and is harmful for charge collections in solar cells.[46] A strategy to prevent this recombination path in sensitized solar cell was proposed for solving this problem; coating an insulating layer in between the 2 electrodes, by this approach interfacial recombination at oxide/electrolyte interface can be largely suppressed.[47] By applying this approach in QDSSCs, with our collaborators we have reported a world-record solar cell with 8.2% certified efficiency.[28]

(3) Charge regeneration in QDs by hole-conducting materials for the sustainable operation of QDSSCs. The redox couple is a key component of the DSSC, as its redox potential can affect the extracted charge energetics and V_{OC} in the final devices. Conventionally, an electrolyte consisting of iodide/triiodide in an organic solvent has been widely used, owing to their ability of fast hole scavenging in comparison to other redox couples.[48, 49] However, for QDSSC iodide/triiodide can induce a big corrosion in QDs, which affects the stability of the cells. Exploiting solid-state hole transporting materials, such as 2,2',7,7'-tetrakis(*N*,*N*-di-*p*-methoxyphenyl-amine)9,9'-spirobifluorene (spiro-OMeTAD) [50] has been proven an useful approach for QDSSCs. Generally, compared with ET dynamics studied in QD/oxide interfaces, much less attention have been given to hole scavenging processes and developing of new hole-conducting materials in the sensitized solar cells' community. Future works on these aspects will be important for the overall solar cell device optimizations.

1.2.3 Shockley-Queisser limit for QDSSCs

Considerable advance in enhancing the power conversion efficiency of QDSSC has been made in the last 5 years, with record power conversion efficiency ~8.2% being reported recently.[28] However, such values are still much lower than that for dyes (~13% for DSSCs[29]) and bulk semiconductor solar cells (Si with 26% power conversation efficiency, for instance). According to S-Q limit, for QDSSC the maximum power conversion efficiency can be achievable for QDs with an absorption bandgap ~1.35 eV.[10] As we discussed previously, the interfacial energetics (ΔG) for triggering charge transfer are lost with charge extraction, representing a thermal energy dissipation channel in the final devices with a consequent drop in power conversion efficiency. By taking the ET energy loss contribution into account, Giebink *et.al.* have recalculated the S-Q limit in the situation of excitonic solar cells

(including QDSSCs).[11] The results adapted from the reference [11] are shown in figure 1.6. Given a driving force (or energy loss) ΔG from 0.1 eV to 0.5 eV, the theoretical solar energy conversion efficiency goes down dramatically from ~31% to only 22%. The drop of efficiency is mainly associated with the decrease of open circuit potential in the device shown in the inset, originating from the thermal energy loss accompanying charge transfer.

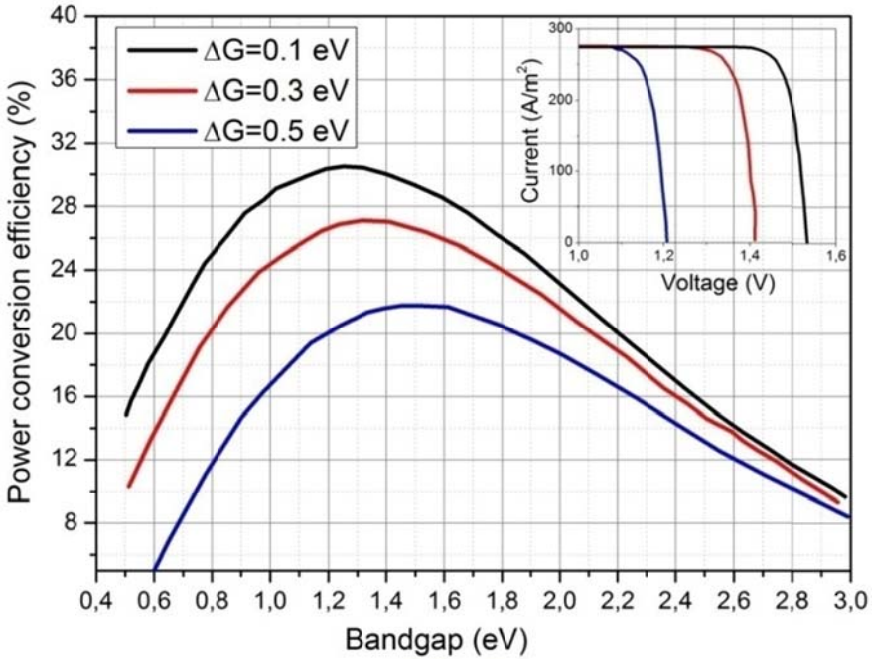

Figure 1.6 The S-Q limit for QDSSCs for considering additional thermal energy loss (ΔG) during ET. Inset shows the change of open circuit potential with respective energy loss.

1.3 Strategies for boosting power conversation efficiency in QDSSCs

Boosting power conversion efficiencies of QDSSCS requires an optimization of parameters regarding to enhance J_{SC} and V_{OC}. In principle, the optimizations regarding J_{SC} and V_{OC} should be achieved for all interfaces where charge transfer/transport is involved (QD/oxide, oxide-electrolyte, QD/electrolyte etc.). In this thesis, we will mainly limit our discussion to the charge separation processes at QD/oxide interfaces.

1.3.1 Boosting J_{SC} by reducing trapping process in QDs: the role of surface chemistry

QDs have a great potential for their application in solar cells owing to appealing optoelectronic properties.[12, 51] Their promise for the optoelectronics is, however, largely hindered by the complex surface chemistry due to high density of dangling bonds at QD surfaces. Understanding the physic-chemistry of QD surfaces is a topic of intense interests. QD surface plays a key role in many usual

properties, such as electronics structures[52, 53], optical properties[54] and their chemical stability.[24] Relevant to solar cell applications, uncoordinated atoms at QD surfaces can introduce high densities of trap states, promoting recombination centers which are detrimental to efficient extraction of photogenerated charges.[55]

Surface passivation of QDs is therefore of paramount importance and has been reported essential for improving the photocurrent J_{SC} and thus efficiencies of QDSSCs.[56-58] Different passivation strategies have been proposed and reported to cure the surface states in QDs. One of the most popular approaches for passivating QDS is to grow a shell of wide band gap materials (such as ZnS as reported by Guyot-Sionnest's [59] and Bawendi's group[60]). This results in notable improvement of QD photoluminescence yield and long-term stability[61-63]. Nevertheless, QDSSC devices with this passivation strategy showed only moderate efficiency (~5%)[56-58], plausibly due to a thick tunneling barrier for the hole extraction to electrolyte imposed by the inorganic capping. Alternatively, other passivation approaches by capping QDs with *atoms* [44, 64], *short organic ligands* [57, 65, 66] and *short inorganic ligands*[67, 68] have recently attracted much research attention owing to simplicity of these treatments, and tunable barriers for charge transfer. More importantly, the extra advantage for exploiting atomic and organic/inorganic molecules for QD passivation lies in the power of synthetic chemistry: a great variety of candidate materials with designed electronic structures can be synthesized. Beyond the passivation effect, surface ligands can bring new functionality and provide flexibility in design parameters, such as workfunction tuning via QD capping with molecular dipoles, surface wetting and the tuning of dielectric environment etc. *In chapters 3 and 4, the role of surface chemistry (atomic passivation and molecular passivation) on ET dynamics and thus surface passivation will be discussed.*

1.3.2 Increasing the V_{OC} by reducing thermal energy losses

1.3.2.1 Decreasing the ET energy loss at QD/oxide interfaces

As discussed in section 1.2, the dissociation of exciton confined in QDs into free electrons relies on interfacial energy transfer. Such transfer is driven by the excess energy between the QD LUMO and the bottom of the oxide CB (ΔG in figure 1.5 (B)), establishing a new thermal energy loss channel which limits the obtainable energy in the cell. In a state-of-the-art QDSSC with efficiencies up to 8.2 % as reported recently [28], alloyed QDs $CdSe_xTe_{1-x}$ with a bandgap of ~1.4 eV have been employed. In the champion device, a V_{OC} of 0.65 V has been obtained, indicating a serious thermal energy loss of ~0.75 eV in the devices. In order to prevent such a big voltage loss, an Ohmic contact should be established between sensitizer and an oxide electrode, leading to $\Delta G \rightarrow 0$. However, one should take into account that the delicate charge kinetic balance of the system can be dramatically affected. A reduced ΔG implies slower ET,[31, 69] and then ultimately radiative relaxation within the QD could

compete kinetically. This kinetic competition is at the core of the tradeoff between sensitized solar cells showing low voltage and high current or vice versa.

1.3.2.1.1 Tuning the donor-acceptor coupling strength

In order to decrease the driving force ΔG for ET, other mechanisms and factors regarding ET need to be explored. Besides ΔG, [31, 69, 70] the rate of interfacial ET has been reported to be governed by other few factors, such us the donor-acceptor coupling strength,[71-73] reorganization energy in the Marcus theory framework[30, 74, 75] (phonons and the dielectric environment) and temperature. Controlling the length and nature of bridging molecules between QD and oxide is an extremely convenient and useful means for varying the coupling strength in a systematic way. In both dye and QD sensitized oxide systems, attempts on understanding the bridge length dependent interfacial ET rate have been reported.[71, 72, 76] There is certain consensus in these reports that the charge transfer rate through the linking bridges decays exponentially with the donor-acceptor separation. However, there are also some controversies regarding to reported ET rates in similar systems from different groups, spanning from the sub-ps to the μs regime.[69-72, 77] Additionally, for a given length of the molecule, the structure of the backbone has been reported not to impact the ET rate,[72] being in contrast to the observations that the molecular nature has a big influence on the electron conductance and transfer through molecular wires. [78, 79] *In chapter 3, the role of the bridge molecule, both the length and the nature, on tuning the donor-acceptor coupling strength will be investigated.*

1.3.2.1.2 Tuning the donor-acceptor energetics

Another way to reduce the energy consumption during charge transfer is to achieve a tunable interfacial energetics *via* control by synthetic chemistry. For a given size of the QD, energetics modification to reduce ΔG can be achieved by either down-shifting QD energy levels or up-shifting the oxide conduction band. For the latter case, doping has been reported as a useful means for modifying the work function in the oxide electrode[80, 81].

Recent research interests on exploiting organic small molecules for tuning the electronic structures of QDs though mixing of the frontier orbitals at the QD–ligand interface, offer a convenient path for controlling the QD energetics. [44, 52-54, 82, 83] Especially, the introduction of ligand dipole effects at QD surfaces to modulate energy levels has resulted in the shift of energy levels up to ~1 eV in a controlled manner.[52] Such tuning of the energetics in QDs is extremely appealing for solar cell applications for controlling the interfacial exciton dissociation efficiency by tuning interfacial energetics. Indeed a few recent reports exploit dipole effect for improving the solar cell performance based on QDs.[22, 84-86] It is worth to comment that the dipole effects in principle can be also applicable for oxide surfaces.[87, 88] In a recent report from Sargent's group,[89] a new world record efficiency of ~10.7% in QD bulk junction solar cells was achieved. This achievement was reached by tailoring the energy levels of the oxide

substrate by a monolayer of self-assembled ligands to decrease the energy cost for charge splitting thus increasing the voltage output in the devices. Given the availability and abundance of the ligand molecules, it offers an indispensable and rich tool box for further optimizing interfacial energetics for exciton dissociations in solar cell applications. *In chapter 4, besides the passivation effect discussed in section 1.3.1, the effect of dipole moments on energetics tuning and corresponding ultrafast ET dynamics is investigated.*

1.3.2.2 Exploiting the excess energy of hot carriers: for QDSSC efficiency beyond the S-Q limit

As discussed in the section 1.1, one major loss channel in the solar power conversion efficiency of single absorber solar cells is the ultrafast cooling (~ps time scales) of hot carriers. Preventing cooling processes governed by multi-phonon emission could, in principle, leads to efficiency gain for solar energy conversion.[90] Various strategies for overcoming the release of hot carrier excess energy as heat have been proposed[90-94] and will be discussed in the following sections. If realized, they can pave the way towards solar cells with power conversion efficiencies exceeding the S-Q limit.

1.3.2.2.1 Hot carrier solar cells

Nozik *et. al*[90] proposed that a direct extraction of carriers from hot states by selective contacts can result in both high open circuit potentials (E_{ex}+E_g as an example depicted in figure 7, *vs.* only E_g if thermalization takes place efficiently before extracting hot carriers) and photocurrents in the so called "hot carrier solar cells". This would enable an energy conversion efficiency of 66% under 1 sun illumination, a nearly 100% improvement *vs.* the Shockley-Queisser limit estimated for a single absorber solar cell.[90] Despite the potential of hot carrier solar cells, suitable cell designs allowing the harvesting of hot carriers have remained elusive. One of the reasons relate with finding suitable absorbers where carrier thermalization is inhabited. Once this is achieved, one should also consider whether the efficient extraction of charges from hot states can take place.

In this respect, QDs with discrete energy states had been long considered as potential candidates for hot carrier solar cells.[92] In principle, carrier cooling rates in QDs can be decreased, as the energy spacing for QD intraband transitions can be as large as several longitudinal optical (LO) phonon energies, hence requiring emission of multiple phonons: a many-body process with very low probability (so called phonon-bottleneck effect).[95, 96] However, It was reported that the phonon-bottleneck effect can be bypassed in QDs by Auger-like process regarding columbic interactions between charges, resulting in a size dependent QD hot carrier relaxation in ultrafast time scales, ~ 0.5-2 ps between $1P_e$-$1S_e$ states.[97, 98] By engineering QD core-shell with type II band alignment, it has been shown that electron-hole interactions can be reduced by exciton splitting, and then the bottleneck

effect is recovered [99]. This result illustrates the importance of surface engineering for preventing carrier cooling losses in nanocrystals.

Alternatively, besides searching for new materials with intrinsic or engineered slow hot carrier cooling rates, tuning kinetic competition between hot carrier transfer towards an electrode and QD intra-band relaxation can offer a new perspective for harvesting hot carriers. In this regard, QD sensitized oxides represent a great platform for extraction of hot electrons as sub-ps electron injection rates from QDs to the oxide can be reached by tuning interfacial QD/oxide chemistry.[74, 77, 100] Reducing the QD/oxide separation allows boosting the QD/oxide coupling and hence ET rate process (as fast as ~6 fs ET rate has been suggested[77]). Tisdale *et. al.* demonstrated sub-50 fs hot electron transfer (HET) in a QD sensitized oxide system[74, 100]. However, in this work, HET processes where only observed when inhibiting carrier thermalization in the QDs, e.g. at liquid N_2 temperatures. Furthermore, an estimate of the efficiency of the process was lacking; aiming efficient HET transfer goes by the hand with aiming improved photoconversion efficiencies. *Realization of efficient HET efficiencies at room temperature and understanding the physics for tuning the efficiency at electrodes are fundamental aspects for the realization of a hot carrier solar cell based on a QD sensitized system, and will be the focus of chapter 6 in this thesis.*

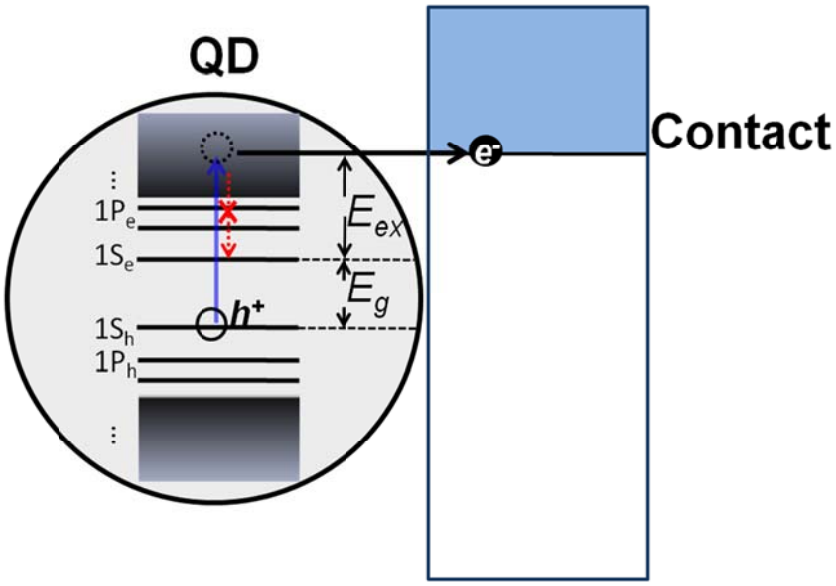

Figure 7 Scheme for hot electron extraction at the QD/oxide interface before thermalization of hot carriers. As a result, the maximum obtainable open circuit voltage (V_{OC}) is $E_{ex}+E_g$, rather than E_g if the hot carrier cooling occurs.

1.3.2.2.2 Multiexciton generation (MEG)

As an alternative approach to the hot carrier concept, the excess energy of the hot carriers can be exploited for promoting a second (or more) electron(s) from the QD HOMO to the QD LUMO orbitals, resulting in two (or more) excitons populating the QD per incident photon. This process is called multiexciton generation (MEG, also referred as carrier multiplication);[94] an sketch of the kinetic processes involved in MEG are illustrated in figure 8(A). For energy conservation reasons, MEG can only take place for phonons impinging the QD absorber with an excess energy at least twice of the bandgap.

Observation of the MEG effect in QDs by ultrafast spectroscopy was first reported in 2004 in a PbSe QDs[94], and was *verified* by following reports in several different QD systems consisting of PbS,[101] PbSe,[102] PbTe,[103], CdSe,[104] Si,[105] InAs,[106] $CuInSe_2$[107] etc. These studies gained great research attention in the photovoltaic community, because harvesting multiple excitons per absorbed photon can improve the performance of solar energy conversion devices (e.g. solar cells and solar fuel devices). The main gain here is the conversion of potential thermal losses into a gain in photocurrent (one photon, 2 electrons). The maximum theoretical efficiency of quantum dot solar cells exhibiting optimal MEG can reach 42% (at one sun for an absorber with a bandgap of 0.7eV)[93, 108]: well above the Shockley-Queisser limit of 33%. However, the yield efficiency of the MEG process is a topic of intense debate: early reports on the MEG efficiency showed extremely high quantum efficiencies up to 700% (1 photon, seven excitons)[101, 104, 109-112], while many follow-up experiments have shown that the MEG effect in QDs is quite moderate, and sometimes is very weak or even absent.[110, 113-116]. It has been proposed that part of the large efficiency gain discrepancies stemmed from experimental pitfalls such us photocharging and sample degradation.[110, 117] On top of that debate, it is still controversial whether the MEG efficiency is enhanced on not in QDs owing to confinement effects when compared with their bulk counterpart phases.[108, 110, 118, 119] Despite all these debates, the occurrence of MEG has been unambiguously addressed and demonstrated on a device level.[120-124] External quantum yields above unity have been reached for wavelengths close or in the UV region of the solar spectrum in solar cells (both bulk junction[122, 123] and sensitized type[121]) and photodetectors[120], demonstrating the relevance of the MEG concept for optoelectronic applications.

The origin of the MEG effect in QDs has been theoretically addressed by atomistic pseudo-potential calculations. These works concluded that a model of impact ionization (II) was capable to explain the MEG effect in QDs.[119, 125] In a simple picture, the generation yield of multiexcitons is controlled by a competition between II and thermalization processes for the hot carriers. If MEG is effective, the ultrafast harvesting of excitons is a request towards practical implementations. This aspect is a very challenging task, as strong Coulomb interactions between multiple charges lead to a decay *via* an ultrafast nonradioactive three-particle process called Auger recombination (a reverse version of MEG

process, as shown in figure 8 (B)). In an Auger process, an electron can recombine with a hole quickly by giving its energy to a third charge (electron or hole), resulting in a quick loss of an exciton, typically within 10-100 ps depending on QD size and nature.[117, 126-129] For an efficient extraction of multiple excitons generated by MEG, dissociation of excitons is necessary to be faster than the time scale of the Auger process. Despite of a great advance in the field, most current studies on MEG still focus on the generation process and quantify its corresponding efficiency. Independent of the efficiency of MEG, for utilizing MEG in solar cells, efficient collection of multiple excitons towards an electrode is a prerequisite. This is a topic which has not yet been extensively investigated.[128, 130] *In chapter 7, we will focus on studying dynamics of multiexciton dissociation in strongly coupled QD and oxide system.*

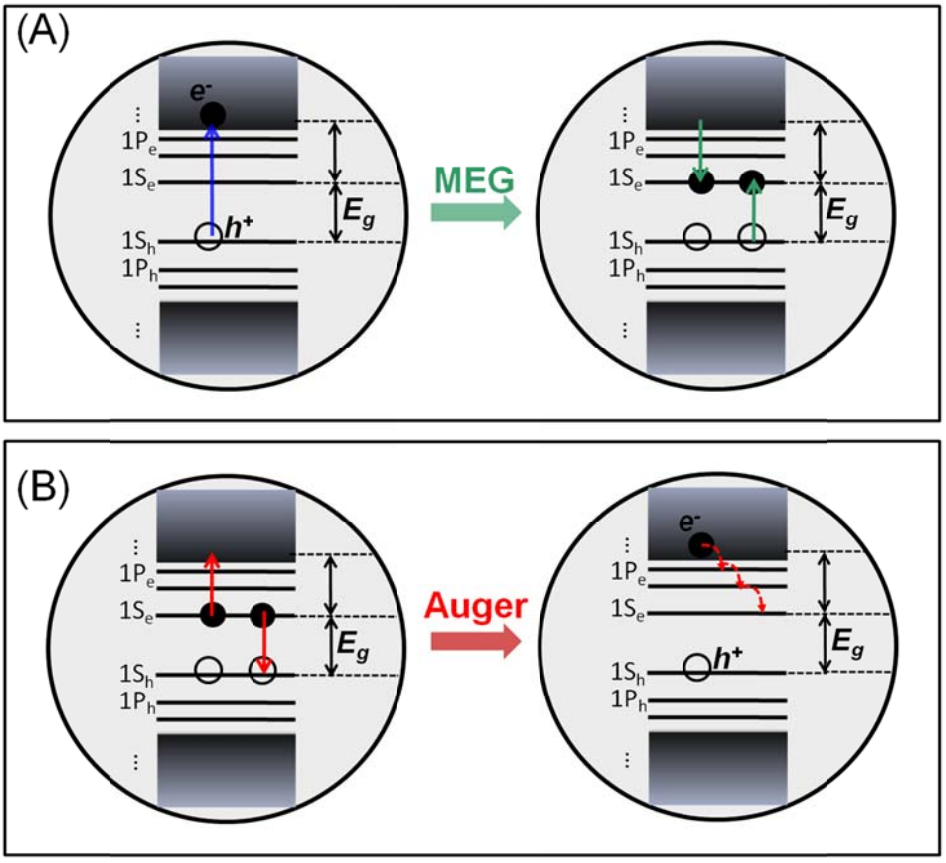

Figure 8 (A) Illustration of a MEG process in a quantum dot, in which absorption of a high energy photon results in two excitons; (B) scheme of the reverse process of MEG: Auger recombination, in which one exciton recombines nonradiatively by transferring its energy to a third charge (*e.g.* an electron in this case).

1.4 Outline of this thesis

In chapter 1 we present a general *introduction* to solar cells, and quantum dot sensitized solar cells (QDSSCs). The theoretical power conversion efficiencies in both cases are analyzed, and strategies for boosting power conversion efficiency in QDSSC are discussed. In *chapter 2*, the *experimental setup* THz spectroscopy for monitoring ET dynamics in QD sensitized oxide is introduced. Material synthesis and *sample preparation* for this study are described in details.

Our specific discussion on strategies for boosting power conversion efficiency in QDSSC is presented in different chapters of this thesis. In chapter 3, and chapters 5-7 we focus on the concept of reducing thermal energy losses in the QDs or in QD/oxide interfaces for enhancing solar cell's open circuit voltages (V_{OC}); in chapter 4 and a small part of chapter 5 we discuss the role of surface chemistry on interfacial QD/oxide electron transfer efficiency (related to improved short circuit currents, $J_{SC,}$ in the devices).

More specifically:

In *chapter 3* we have investigated the role of coupling strength on the ET rate at QD/oxide interfaces, by tuning the length and nature of linkers between QD and oxide. This investigation was performed for a given donor-acceptor energetics (e.g. for a given QD size). Ultrafast charge transfer can be achieved by tuning interfacial chemistry. This approach may hold the potential to allow fast transfer while paying little to none energy in the exciton interfacial dissociation (preventing thermal losses at the electrode);

In *chapter 4*, we show that the passivation of QDs surface can be done by tuning their surface atomic composition, e.g. by controlling deposition steps via successive ionic layer absorption and reaction (SILAR) method. The origin the atomic passivation relates with fine tuning of QD *stoichiometry. The passivation effect* is size-dependent, illustrating that traps in QDs are primarily at the surfaces as discussed in this chapter;

Chapter 5 discusses a unique approach in this thesis, in the sense that, it involves potential gains in both photocurrent and voltage with a single chemical treatment, by molecular capping at QD surfaces. The impact in interfacial QD/oxide dynamics of capping the QDs with ligands defined by different dipole moments is interrogated;

In chapter 6 and 7, hot electron transfer, and multiexciton generation and collection at the electrodes are analyzed for QD/oxide systems. These approaches have the potential of power conversion efficiency beyond S-Q limit are tested in sensitized system.

Chapter 6 explores *multiexciton generation and dissociation* processes at QD/oxide systems. We demonstrate that capturing two 2 electrons from biexciton states in QDs can be realistic, and that the competition between ET and Auger rates dictates the efficiency of the interfacial dissociation.

Additionally, we will show that ultrafast hot electron transfer can effectively compete with the process of MEG, leading to ~0% MEG quantum yield in the system;

Chapter 7 focuses on *harvesting hot electrons*. We show that, ultrafast sub-100fs hot electron transfer can be achieved in QD/oxide systems, notably with unity quantum efficiency yield at room temperature. The effect of excess energy and temperature on QD to oxide interfacial hot transfer efficiency is interrogated;

Chapter 8 summarizes the results and main conclusions of this thesis.

Reference

1. Santer, B. D.; Taylor, K. E.; Wigley, T. M. L.; Johns, T. C.; Jones, P. D.; Karoly, D. J.; Mitchell, J. F. B.; Oort, A. H.; Penner, J. E.; Ramaswamy, V.; Schwarzkopf, M. D.; Stouffer, R. J.; Tett, S. *Nature* **1996,** 382, (6586), 39-46.
2. Hegerl, G. C.; vonStorch, H.; Hasselmann, K.; Santer, B. D.; Cubasch, U.; Jones, P. D. *J Climate* **1996,** 9, (10), 2281-2306.
3. Karl, T. R.; Trenberth, K. E. *Science* **2003,** 302, (5651), 1719-1723.
4. Green, M. A. *Aip Adv* **2013,** 3, (11).
5. Wurfel, P. *Sol Energ Mat Sol C* **1997,** 46, (1), 43-52.
6. Othonos, A. *J Appl Phys* **1998,** 83, (4), 1789-1830.
7. Vardeny, Z.; Tauc, J. *Phys Rev Lett* **1981,** 46, (18), 1223-1226.
8. Linde, D. V. D.; Lambrich, R. *Phys Rev Lett* **1979,** 42, (16), 1090-1093.
9. Shah, J.; Pinczuk, A.; Gossard, A. C.; Wiegmann, W. *Phys Rev Lett* **1985,** 54, (18), 2045-2048.
10. Shockley, W.; Queisser, H. J. *J Appl Phys* **1961,** 32, (3), 510-&.
11. Giebink, N. C.; Wiederrecht, G. P.; Wasielewski, M. R.; Forrest, S. R. *Phys Rev B* **2011,** 83, (19).
12. Murray, C. B.; Kagan, C. R.; Bawendi, M. G. *Annu Rev Mater Sci* **2000,** 30, 545-610.
13. Brus, L. E. *J Chem Phys* **1984,** 80, (9), 4403-4409.
14. Yang, Y. X.; Zheng, Y.; Cao, W. R.; Titov, A.; Hyvonen, J.; Manders, J. R.; Xue, J. G.; Holloway, P. H.; Qian, L. *Nat Photonics* **2015,** 9, (4), 259-266.
15. Shirasaki, Y.; Supran, G. J.; Bawendi, M. G.; Bulovic, V. *Nat Photonics* **2013,** 7, (1), 13-23.
16. Mashford, B. S.; Stevenson, M.; Popovic, Z.; Hamilton, C.; Zhou, Z. Q.; Breen, C.; Steckel, J.; Bulovic, V.; Bawendi, M.; Coe-Sullivan, S.; Kazlas, P. T. *Nat Photonics* **2013,** 7, (5), 407-412.
17. Anikeeva, P. O.; Halpert, J. E.; Bawendi, M. G.; Bulovic, V. *Nano Lett* **2009,** 9, (7), 2532-2536.

18. Dai, X. L.; Zhang, Z. X.; Jin, Y. Z.; Niu, Y.; Cao, H. J.; Liang, X. Y.; Chen, L. W.; Wang, J. P.; Peng, X. G. *Nature* **2014,** 515, (7525), 96-99.

19. Oregan, B.; Gratzel, M. *Nature* **1991,** 353, (6346), 737-740.

20. O'Regan, B. C.; Durrant, J. R. *Accounts Chem Res* **2009,** 42, (11), 1799-1808.

21. Grätzel, M. *Journal of Photochemistry and Photobiology C: Photochemistry Reviews* **2003,** 4, (2), 145-153.

22. Barea, E. M.; Shalom, M.; Gimenez, S.; Hod, I.; Mora-Sero, I.; Zaban, A.; Bisquert, J. *J Am Chem Soc* **2010,** 132, (19), 6834-6839.

23. Alivisatos, A. P.; Katari, J. B. *Abstr Pap Am Chem S* **1995,** 210, 36-Phys.

24. Alivisatos, A. P. *J Phys Chem-Us* **1996,** 100, (31), 13226-13239.

25. Wise, F. W. *Accounts Chem Res* **2000,** 33, (11), 773-780.

26. Vogel, R.; Pohl, K.; Weller, H. *Chem Phys Lett* **1990,** 174, (3-4), 241-246.

27. Zaban, A.; Micic, O. I.; Gregg, B. A.; Nozik, A. J. *Langmuir* **1998,** 14, (12), 3153-3156.

28. Zhao, K.; Pan, Z.; Mora-Seró, I.; Cánovas, E.; Wang, H.; Song, Y.; Gong, X.; Wang, J.; Bonn, M.; Bisquert, J.; Zhong, X. *J Am Chem Soc* **2015**.

29. Yella, A.; Lee, H. W.; Tsao, H. N.; Yi, C. Y.; Chandiran, A. K.; Nazeeruddin, M. K.; Diau, E. W. G.; Yeh, C. Y.; Zakeeruddin, S. M.; Gratzel, M. *Science* **2011,** 334, (6056), 629-634.

30. Anderson, N. A.; Lian, T. Q. *Annu Rev Phys Chem* **2005,** 56, 491-519.

31. Canovas, E.; Moll, P.; Jensen, S. A.; Gao, Y. A.; Houtepen, A. J.; Siebbeles, L. D. A.; Kinge, S.; Bonn, M. *Nano Lett* **2011,** 11, (12), 5234-5239.

32. Schnadt, J.; Bruhwiler, P. A.; Patthey, L.; O'Shea, J. N.; Sodergren, S.; Odelius, M.; Ahuja, R.; Karis, O.; Bassler, M.; Persson, P.; Siegbahn, H.; Lunell, S.; Martensson, N. *Nature* **2002,** 418, (6898), 620-623.

33. Chae, W. S.; Choi, E.; Jung, Y. K.; Jung, J. S.; Lee, J. K. *Appl Phys Lett* **2014,** 104, (15).

34. Nishikawa, K.; Takeda, Y.; Yamanaka, K.; Motohiro, T.; Sato, D.; Ota, J.; Miyashita, N.; Okada, Y. *J Appl Phys* **2012,** 111, (4).

35. van Driel, A. F.; Allan, G.; Delerue, C.; Lodahl, P.; Vos, W. L.; Vanmaekelbergh, D. *Phys Rev Lett* **2005,** 95, (23).

36. Boehme, S. C.; Azpiroz, J. M.; Aulin, Y. V.; Grozema, F. C.; Vanmaekelbergh, D.; Siebbeles, L. D. A.; Infante, I.; Houtepen, A. J. *Nano Lett* **2015,** 15, (5), 3056-3066.

37. Wuister, S. F.; Donega, C. D.; Meijerink, A. *J Phys Chem B* **2004,** 108, (45), 17393-17397.

38. Anderson, N. C.; Hendricks, M. P.; Choi, J. J.; Owen, J. S. *J Am Chem Soc* **2013,** 135, (49), 18536-18548.

39. de la Fuente, M. S.; Sanchez, R. S.; Gonzalez-Pedro, V.; Boix, P. P.; Mhaisalkar, S. G.; Rincon, M. E.; Bisquert, J.; Mora-Sero, I. *J Phys Chem Lett* **2013,** 4, (9), 1519-1525.

40. Kuno, M.; Lee, J. K.; Dabbousi, B. O.; Mikulec, F. V.; Bawendi, M. G. *J Chem Phys* **1997,** 106, (23), 9869-9882.

41. Hines, M. A.; Guyot-Sionnest, P. *J Phys Chem-Us* **1996,** 100, (2), 468-471.

42. Oh, S. J.; Berry, N. E.; Choi, J. H.; Gaulding, E. A.; Paik, T.; Hong, S. H.; Murray, C. B.; Kagan, C. R. *Acs Nano* **2013,** 7, (3), 2413-2421.

43. Wang, H.; Barcelo, I.; Lana-Vilarreal, T.; Gomez, R.; Bonn, M.; Canovas, E. *Nano Lett* **2014,** 14, (10), 5780-5786.

44. Tang, J.; Kemp, K. W.; Hoogland, S.; Jeong, K. S.; Liu, H.; Levina, L.; Furukawa, M.; Wang, X. H.; Debnath, R.; Cha, D. K.; Chou, K. W.; Fischer, A.; Amassian, A.; Asbury, J. B.; Sargent, E. H. *Nat Mater* **2011,** 10, (10), 765-771.

45. Hagfeldt, A.; Gratzel, M. *Chem Rev* **1995,** 95, (1), 49-68.

46. Listorti, A.; O'Regan, B.; Durrant, J. R. *Chem Mater* **2011,** 23, (15), 3381-3399.

47. Palomares, E.; Clifford, J. N.; Haque, S. A.; Lutz, T.; Durrant, J. R. *J Am Chem Soc* **2003,** 125, (2), 475-482.

48. Boschloo, G.; Hagfeldt, A. *Accounts Chem Res* **2009,** 42, (11), 1819-1826.

49. Wu, J. H.; Lan, Z.; Lin, J. M.; Huang, M. L.; Huang, Y. F.; Fan, L. Q.; Luo, G. G. *Chem Rev* **2015,** 115, (5), 2136-2173.

50. Bach, U.; Lupo, D.; Comte, P.; Moser, J. E.; Weissortel, F.; Salbeck, J.; Spreitzer, H.; Gratzel, M. *Nature* **1998,** 395, (6702), 583-585.

51. Carey, G. H.; Abdelhady, A. L.; Ning, Z.; Thon, S. M.; Bakr, O. M.; Sargent, E. H. *Chem Rev* **2015**.

52. Brown, P. R.; Kim, D.; Lunt, R. R.; Zhao, N.; Bawendi, M. G.; Grossman, J. C.; Bulovic, V. *Acs Nano* **2014,** 8, (6), 5863-5872.

53. Knowles, K. E.; Frederick, M. T.; Tice, D. B.; Morris-Cohen, A. J.; Weiss, E. A. *J Phys Chem Lett* **2012,** 3, (1), 18-26.

54. Frederick, M. T.; Amin, V. A.; Swenson, N. K.; Ho, A. Y.; Weiss, E. A. *Nano Lett* **2013,** 13, (1), 287-292.

55. Hines, D. A.; Kamat, P. V. *Acs Appl Mater Inter* **2014,** 6, (5), 3041-3057.

56. de la Fuente, M. S.; Sánchez, R. S.; González-Pedro, V.; Boix, P. P.; Mhaisalkar, S. G.; Rincón, M. E.; Bisquert, J.; Mora-Seró, I. *The Journal of Physical Chemistry Letters* **2013**, 1519-1525.

57. Guijarro, N.; Lana-Villarreal, T.; Lutz, T.; Haque, S. A.; Gómez, R. *The Journal of Physical Chemistry Letters* **2012,** 3, (22), 3367-3372.

58. Santra, P. K.; Kamat, P. V. *Journal of the American Chemical Society* **2012,** 134, (5), 2508-2511.

59. Hines, M. A.; Guyot-Sionnest, P. *The Journal of Physical Chemistry* **1996,** 100, (2), 468-471.

60. Dabbousi, B. O.; Rodriguez-Viejo, J.; Mikulec, F. V.; Heine, J. R.; Mattoussi, H.; Ober, R.; Jensen, K. F.; Bawendi, M. G. *The Journal of Physical Chemistry B* **1997,** 101, (46), 9463-9475.

61. Liu, Y.; Gibbs, M.; Perkins, C. L.; Tolentino, J.; Zarghami, M. H.; Bustamante, J.; Law, M. *Nano Lett* **2011,** 11, (12), 5349-5355.

62. Liu, Y.; Tolentino, J.; Gibbs, M.; Ihly, R.; Perkins, C. L.; Liu, Y.; Crawford, N.; Hemminger, J. C.; Law, M. *Nano Lett* **2013,** 13, (4), 1578-1587.

63. Peng, X. G.; Schlamp, M. C.; Kadavanich, A. V.; Alivisatos, A. P. *J Am Chem Soc* **1997,** 119, (30), 7019-7029.

64. Thon, S. M.; Ip, A. H.; Voznyy, O.; Levina, L.; Kemp, K. W.; Carey, G. H.; Masala, S.; Sargent, E. H. *Acs Nano* **2013,** 7, (9), 7680-7688.

65. Pattantyus-Abraham, A. G.; Kramer, I. J.; Barkhouse, A. R.; Wang, X.; Konstantatos, G.; Debnath, R.; Levina, L.; Raabe, I.; Nazeeruddin, M. K.; Grätzel, M.; Sargent, E. H. *ACS Nano* **2010,** 4, (6), 3374-3380.

66. de la Fuente, M. S.; Sánchez, R. S.; González-Pedro, V.; Boix, P. P.; Mhaisalkar, S. G.; Rincón, M. E.; Bisquert, J.; Mora-Seró, I. *The Journal of Physical Chemistry Letters* **2013,** 4, (9), 1519-1525.

67. Kovalenko, M. V.; Scheele, M.; Talapin, D. V. *Science* **2009,** 324, (5933), 1417-1420.

68. Dirin, D. N.; Dreyfuss, S.; Bodnarchuk, M. I.; Nedelcu, G.; Papagiorgis, P.; Itskos, G.; Kovalenko, M. V. *J Am Chem Soc* **2014,** 136, (18), 6550-6553.

69. Robel, I.; Kuno, M.; Kamat, P. V. *J Am Chem Soc* **2007,** 129, (14), 4136-+.

70. Kongkanand, A.; Tvrdy, K.; Takechi, K.; Kuno, M.; Kamat, P. V. *J Am Chem Soc* **2008,** 130, (12), 4007-4015.

71. Dibbell, R. S.; Watson, D. F. *J Phys Chem C* **2009,** 113, (8), 3139-3149.

72. Hyun, B. R.; Bartnik, A. C.; Sun, L. F.; Hanrath, T.; Wise, F. W. *Nano Lett* **2011,** 11, (5), 2126-2132.

73. Hines, D. A.; Forrest, R. P.; Corcelli, S. A.; Kamat, P. V. *J Phys Chem B* **2015,** 119, (24), 7439-7446.

74. Tisdale, W. A.; Zhu, X. Y. *P Natl Acad Sci USA* **2011,** 108, (3), 965-970.

75. Marcus, R. A. *Rev Mod Phys* **1993,** 65, (3), 599-610.

76. Asbury, J. B.; Hao, E. C.; Wang, Y. Q.; Lian, T. Q. *J Phys Chem B* **2000,** 104, (50), 11957-11964.

77. Yang, Y.; Rodriguez-Cordoba, W.; Xiang, X.; Lian, T. Q. *Nano Lett* **2012,** 12, (1), 303-309.

78. Tao, N. J. *Nat Nanotechnol* **2006,** 1, (3), 173-181.

79. Nitzan, A.; Ratner, M. A. *Science* **2003,** 300, (5624), 1384-1389.

80. Martinez, U.; Giordano, L.; Pacchioni, G. *J Chem Phys* **2008,** 128, (16).

81. Lee, G. I.; Nath, N. C. D.; Sarker, S.; Shin, W. H.; Ahammad, A. J. S.; Kang, J. K.; Lee, J. J. *Phys Chem Chem Phys* **2012,** 14, (15), 5255-5259.

82. Soreni-Hararl, M.; Yaacobi-Gross, N.; Steiner, D.; Aharoni, A.; Banin, U.; Millo, O.; Tessler, N. *Nano Lett* **2008,** 8, (2), 678-684.

83. Frederick, M. T.; Amin, V. A.; Weiss, E. A. *J Phys Chem Lett* **2013,** 4, (4), 634-640.

84. Chuang, C. H. M.; Brown, P. R.; Bulovic, V.; Bawendi, M. G. *Nat Mater* **2014,** 13, (8), 796-801.

85. Santra, P. K.; Palmstrom, A. F.; Tanskanen, J. T.; Yang, N.; Bent, S. F. *J Phys Chem C* **2015,** 119, (6), 2996-3005.

86. Shalom, M.; Ruhle, S.; Hod, I.; Yahav, S.; Zaban, A. *J Am Chem Soc* **2009,** 131, (29), 9876-+.

87. Ashkenasy, G.; Cahen, D.; Cohen, R.; Shanzer, A.; Vilan, A. *Accounts Chem Res* **2002,** 35, (2), 121-128.

88. Cahen, D.; Kahn, A.; Umbach, E. *Materials Today* **2005,** 8, (7), 32-41.

89. Kim, G.-H.; García de Arquer, F. P.; Yoon, Y. J.; Lan, X.; Liu, M.; Voznyy, O.; Yang, Z.; Fan, F.; Ip, A. H.; Kanjanaboos, P.; Hoogland, S.; Kim, J. Y.; Sargent, E. H. *Nano Lett* **2015,** 15, (11), 7691-7696.

90. Ross, R. T.; Nozik, A. J. *J Appl Phys* **1982,** 53, (5), 3813-3818.

91. Hanna, M. C.; Nozik, A. J. *J Appl Phys* **2006,** 100, (7).

92. Nozik, A. J. *Physica E* **2002,** 14, (1-2), 115-120.

93. Klimov, V. I. *Appl Phys Lett* **2006,** 89, (12).

94. Schaller, R. D.; Klimov, V. I. *Phys Rev Lett* **2004,** 92, (18).

95. Inoshita, T.; Sakaki, H. *Physica B* **1996,** 227, (1-4), 373-377.

96. Geiregat, P.; Delerue, C.; Justo, Y.; Aerts, M.; Spoor, F.; Van Thourhout, D.; Siebbeles, L. D. A.; Allan, G.; Houtepen, A. J.; Hens, Z. *Acs Nano* **2015,** 9, (1), 778-788.

97. Klimov, V. I.; McBranch, D. W. *Phys Rev Lett* **1998,** 80, (18), 4028-4031.

98. Hendry, E.; Koeberg, M.; Wang, F.; Zhang, H.; Donega, C. D.; Vanmaekelbergh, D.; Bonn, M. *Phys Rev Lett* **2006,** 96, (5).

99. Pandey, A.; Guyot-Sionnest, P. *Science* **2008,** 322, (5903), 929-932.

100. Tisdale, W. A.; Williams, K. J.; Timp, B. A.; Norris, D. J.; Aydil, E. S.; Zhu, X. Y. *Science* **2010,** 328, (5985), 1543-1547.

101. Ellingson, R. J.; Beard, M. C.; Johnson, J. C.; Yu, P. R.; Micic, O. I.; Nozik, A. J.; Shabaev, A.; Efros, A. L. *Nano Lett* **2005,** 5, (5), 865-871.

102. Aerts, M.; Sandeep, C. S. S.; Gao, Y. A.; Savenije, T. J.; Schins, J. M.; Houtepen, A. J.; Kinge, S.; Siebbeles, L. D. A. *Nano Lett* **2011,** 11, (10), 4485-4489.

103. Murphy, J. E.; Beard, M. C.; Norman, A. G.; Ahrenkiel, S. P.; Johnson, J. C.; Yu, P. R.; Micic, O. I.; Ellingson, R. J.; Nozik, A. J. *J Am Chem Soc* **2006,** 128, (10), 3241-3247.

104. Schaller, R. D.; Petruska, M. A.; Klimov, V. I. *Appl Phys Lett* **2005,** 87, (25).

105. Beard, M. C.; Knutsen, K. P.; Yu, P. R.; Luther, J. M.; Song, Q.; Metzger, W. K.; Ellingson, R. J.; Nozik, A. J. *Nano Lett* **2007,** 7, (8), 2506-2512.

106. Pijpers, J. J. H.; Hendry, E.; Milder, M. T. W.; Fanciulli, R.; Savolainen, J.; Herek, J. L.; Vanmaekelbergh, D.; Ruhman, S.; Mocatta, D.; Oron, D.; Aharoni, A.; Banin, U.; Bonn, M. *J Phys Chem C* **2008,** 112, (12), 4783-4784.

107. Stolle, C. J.; Schaller, R. D.; Korgel, B. A. *J Phys Chem Lett* **2014,** 5, (18), 3169-3174.

108. Beard, M. C.; Midgett, A. G.; Hanna, M. C.; Luther, J. M.; Hughes, B. K.; Nozik, A. J. *Nano Lett* **2010,** 10, (8), 3019-3027.

109. Schaller, R. D.; Agranovich, V. M.; Klimov, V. I. *Nat Phys* **2005,** 1, (3), 189-194.

110. Nair, G.; Chang, L. Y.; Geyer, S. M.; Bawendi, M. G. *Nano Lett* **2011,** 11, (5), 2145-2151.

111. Trinh, M. T.; Houtepen, A. J.; Schins, J. M.; Hanrath, T.; Piris, J.; Knulst, W.; Goossens, A. P. L. M.; Siebbeles, L. D. A. *Nano Lett* **2008,** 8, (6), 1713-1718.

112. Schaller, R. D.; Sykora, M.; Pietryga, J. M.; Klimov, V. I. *Nano Lett* **2006,** 6, (3), 424-429.

113. Nair, G.; Bawendi, M. G. *Phys Rev B* **2007,** 76, (8).

114. Nair, G.; Geyer, S. M.; Chang, L. Y.; Bawendi, M. G. *Phys Rev B* **2008,** 78, (12).

115. Ben-Lulu, M.; Mocatta, D.; Bonn, M.; Banin, U.; Ruhman, S. *Nano Lett* **2008,** 8, (4), 1207-1211.

116. Miaja-Avila, L.; Tritsch, J. R.; Wolcott, A.; Chan, W. L.; Nelson, C. A.; Zhu, X. Y. *Nano Lett* **2012,** 12, (3), 1588-1591.

117. McGuire, J. A.; Sykora, M.; Joo, J.; Pietryga, J. M.; Klimov, V. I. *Nano Lett* **2010,** 10, (6), 2049-2057.

118. Pijpers, J. J. H.; Ulbricht, R.; Tielrooij, K. J.; Osherov, A.; Golan, Y.; Delerue, C.; Allan, G.; Bonn, M. *Nat Phys* **2009,** 5, (11), 811-814.

119. Allan, G.; Delerue, C. *Phys Rev B* **2006,** 73, (20).

120. Sukhovatkin, V.; Hinds, S.; Brzozowski, L.; Sargent, E. H. *Science* **2009,** 324, (5934), 1542-1544.

121. Sambur, J. B.; Novet, T.; Parkinson, B. A. *Science* **2010,** 330, (6000), 63-66.

122. Semonin, O. E.; Luther, J. M.; Choi, S.; Chen, H. Y.; Gao, J. B.; Nozik, A. J.; Beard, M. C. *Science* **2011,** 334, (6062), 1530-1533.

123. Böhm, M. L.; Jellicoe, T. C.; Tabachnyk, M.; Davis, N. J. L. K.; Wisnivesky-Rocca-Rivarola, F.; Ducati, C.; Ehrler, B.; Bakulin, A. A.; Greenham, N. C. *Nano Lett* **2015**.

124. Davis, N. J. L. K.; Bohm, M. L.; Tabachnyk, M.; Wisnivesky-Rocca-Rivarola, F.; Jellicoe, T. C.; Ducati, C.; Ehrler, B.; Greenham, N. C. *Nat Commun* **2015,** 6.

125. Franceschetti, A.; An, J. M.; Zunger, A. *Nano Lett* **2006,** 6, (10), 2191-2195.

126. Robel, I.; Gresback, R.; Kortshagen, U.; Schaller, R. D.; Klimov, V. I. *Phys Rev Lett* **2009,** 102, (17), 177404.

127. Klimov, V. I.; Mikhailovsky, A. A.; McBranch, D. W.; Leatherdale, C. A.; Bawendi, M. G. *Science* **2000,** 287, (5455), 1011-1013.

128. Zhu, H. M.; Yang, Y.; Lian, T. Q. *Accounts Chem Res* **2013,** 46, (6), 1270-1279.

129. Yang, Y.; Lian, T. Q. *Coordination Chemistry Reviews* **2014,** 263, 229-238.

130. Zidek, K.; Zheng, K. B.; Abdellah, M.; Lenngren, N.; Chabera, P.; Pullerits, T. *Nano Lett* **2012,** 12, (12), 6393-6399.

Chapter 2

Experimental Technique and Sample Preparation

Understanding the dynamics of interfacial electron transfer in QD sensitized oxides is essential to design and optimize QDSSCs. However, for monitoring charge flow at QD/oxide interfaces is a non-trivial task for the following reasons: (i) If one aim to measure conductance across a given interface, metallic contacts are required: an aspect that is extremely challenging (if not impossible) when aiming contacting nanostructures with sizes of few nanometers in diameter; (2) Nano-contacts could dramatically modify the native properties of the semiconductor nanocrystals; (3) Conventional electronics could be too slow to resolve events happening in ultrafast time scales[1-3]. For all these reasons accessing information about the conductance across a nano-sized interfaces in a non-contact fashion seems mandatory. These constrains can be circumvented by employing ultrafast THz spectroscopy for monitoring interfacial electron transfer dynamics. This tool is able to resolve with sub-ps resolution and in a non-contact fashion the pump induced conductivity of a system, and as described in detail below, is perfectly suited to measure interfacial charge transfer processes in QD sensitized oxides.

In this chapter, we will discuss briefly some experimental optical pump Terahertz probe (OPTP) spectroscopy, the basics for THz generation and detection, and how to monitor and interpret the data regarding the electron transfer dynamics at interfaces. Finally, we describe in some detail the procedures for the preparation of the samples analyzed in this thesis e.g. QD synthesis, oxide sensitization.

2.1 Introduction to Terahertz spectroscopy

Terahertz (THz) frequencies are located between the far-infrared and the microwave region in the electromagnetic spectrum. The energy of the photons in the 0.1-30 THz region comprises energies ranging between~0.4-123 meV. The interaction of THz light with materials offers a powerful spectroscopic tool for investigating many fundamental aspects of matter including molecular rotations, vibrations and particularly charge motion. Methods for the emission and detection of THz radiation are well established up to date and exploited for time-resolved studies, in a pump-probe scheme, allowing interrogating the photoconductivity of samples with sub-ps resolutions. There are several good reviews in the literature summarizing the technical aspect and applications for THz

spectroscopy[4-6]. In this chapter we will only briefly introduce the specific characteristics of our setup and measurements when applied to our particular samples (QD sensitized oxides).

2.1.1 Optical pump terahertz probe (OPTP) spectroscopy: the setup

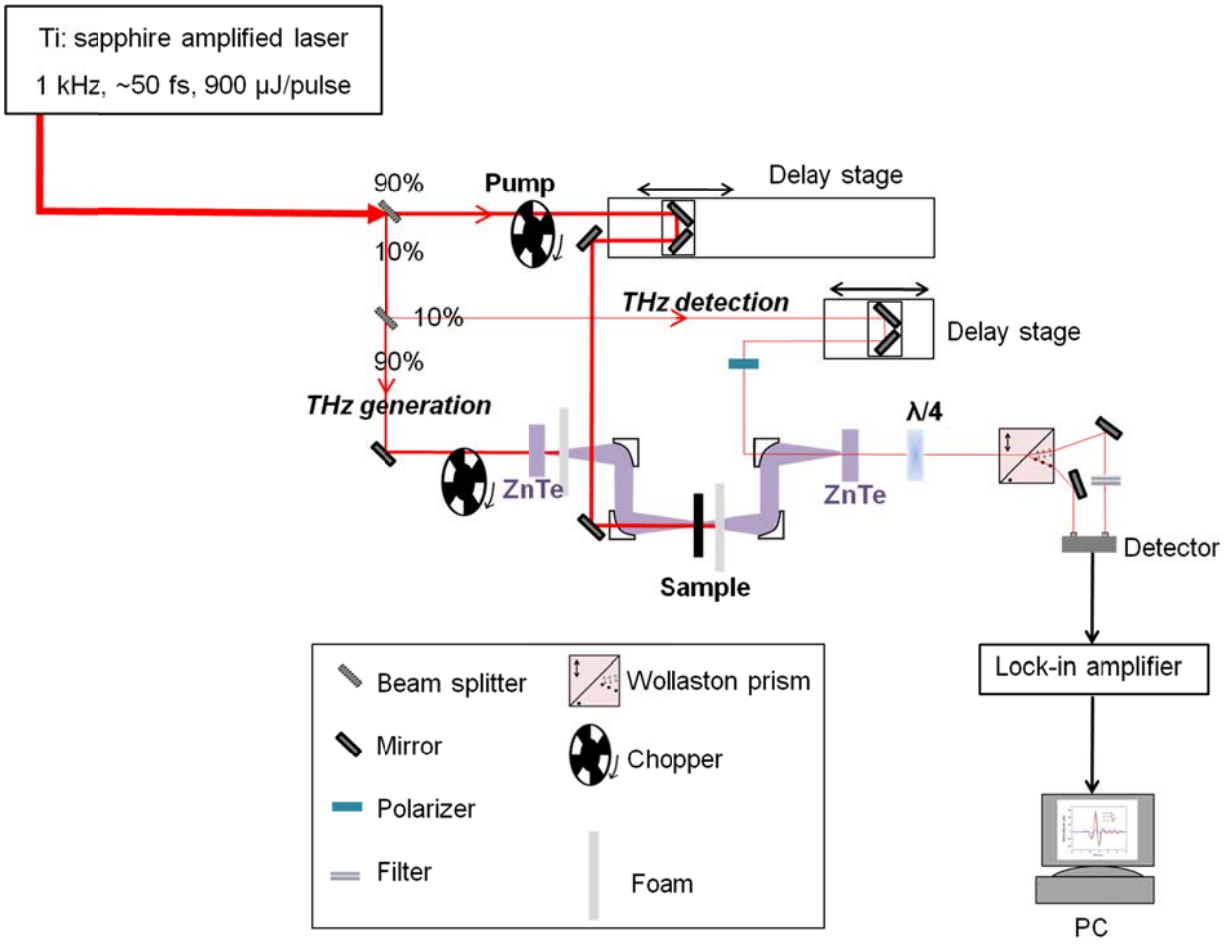

Figure 2.1 Layout of an Optical Pump THz probe (OPTP) spectrometer.

The schematic of the THz spectrometer employed in this work is shown in figure 2.1. In our setup, the ultrafast THz pulse with ~1 ps duration is generated through optical rectification (OR) of a near infrared 800nm (50fs FWHM) femtosecond laser pulse in a ZnTe crystal. OR is a second-order nonlinear process, in which low-frequency polarization with DC offset is developed when an extremely intense femtosecond laser pulse propagates through a nonlinear crystal (*eg.* ZnTe). This process can be also seen as difference-frequency generation between the frequencies within the bandwidth of a short optical pulse. [4, 5, 7] For an efficient THz generation, a so called "phase matching" condition needs to be fulfilled. In a perfect phase matching condition, the newly produced THz wave at the frontier of laser propagation travels across the entire generation crystal together with the laser

pump at the same speed. When the latter condition is not fulfilled, THz wave fronts generated at different time-space positions in the sample result in a deconstructive interference. At the same time, the detection of THz pulses is also based on a nonlinear process called Pockels effect which also occurs in a $\chi^{(2)}$crystal like ZnTe. The Pockels effect consists in the change of the refractive index of the detection crystal induced by the THz electric field. The THz induced birefringence is linearly proportional to the applied THz electric field. By time delaying an ultra-short optical pulse (sampling beam) respect to the THz pulse, the THz field can be readily mapped out in the detection crystal in time-domain. Additionally, for monitoring the dynamics of photo-excited carriers in the sample, a pump pulse in the uv-vis range is employed for sample excitation.

2.1.2 Optical pump terahertz probe (OPTP) spectroscopy: the measurements on QD-sensitized oxide

Using optical pump-terahertz probe (OPTP) spectroscopy for monitoring ET at QD/oxide interfaces, is based on exciting QD donors by a femtosecond optical laser pulse and subsequently probing the induced transient terahertz (THz) wave absorption with sub-picosecond time resolution. This approach has been proven to be a powerful tool for monitoring ET at the QD/oxide interface.[8-10] *The working principle of OPTP, when applied to sensitized samples, is schematically shown in figure 2.2 (A) and based on the fact that THz probe can only be absorbed by free electrons in the oxide CB for our samples due to its low energy bandwidth (2 THz, is equivalent to 8 meV, well below intraband transitions in the QDs).* After visible pump photo-excitation of the QDs, if electrons have not been transferred to the oxide (case I), the transmitted THz probe does not experience any absorption (the THz signal before and after photo-excitation is identical); however, if electrons are transferred from the QD to the oxide phase (case II), the THz probe is absorbed by the free electrons populating the oxide conduction band (where they become mobile). The latter process can be traced with a picosecond time resolution just by changing the time between sample excitation and detection (e.g. by changing the pump-probe delay). More precisely, the photo induced transient THz absorption *ΔE* (*E* represents the amplitude of the THz electric field) is related to the photo-induced real conductivity *ΔRe(σ)* in the sample which can be obtained as following:

$$\frac{d}{dt}Re(\sigma)(t) = \frac{d}{dt}(e * n(t) * \mu(t)) = e * \frac{d}{dt}(n(t) * \mu(t))$$

$$= e * \frac{d}{dt}n(t) * \mu + e * n(t) * \frac{d}{dt}\mu(t), \quad \text{Equation 2.1}$$

in which *n(t)* is the electron density injected into oxides for a given time delay, *e* is the electron charge and μ stands for the intrinsic mobility of electrons in the oxide CB and $\frac{d}{dt}\mu(t)$ as the possible mobility modulation due to carrier-carrier interactions. By pumping QDs with fluences allowing in the low

excitation range, carrier-carrier interaction can be neglected and mobility in the material can be treated as constant. Then equation 2.1 can be re-written as:

$$\frac{d}{dt}Re(\sigma)(t) = e * \mu * \frac{d}{dt}n, \quad \text{or } \Delta\, Re(\sigma)(t) = e * \mu * \Delta n(t), \quad \text{Equation 2.2}$$

In other words, by monitoring the photo-induced ΔE as a function of pump-probe delay time, one can obtain OPTP dynamics and from them the electron transfer rate. Note as well that as evident from equation 2.2, the amplitude of the signal reflect carrier density in the oxide. Taking into account that the density of impinging photons is known (when reflection and transmission losses are considered) one can get an estimate or even quantify the efficiency of the process.

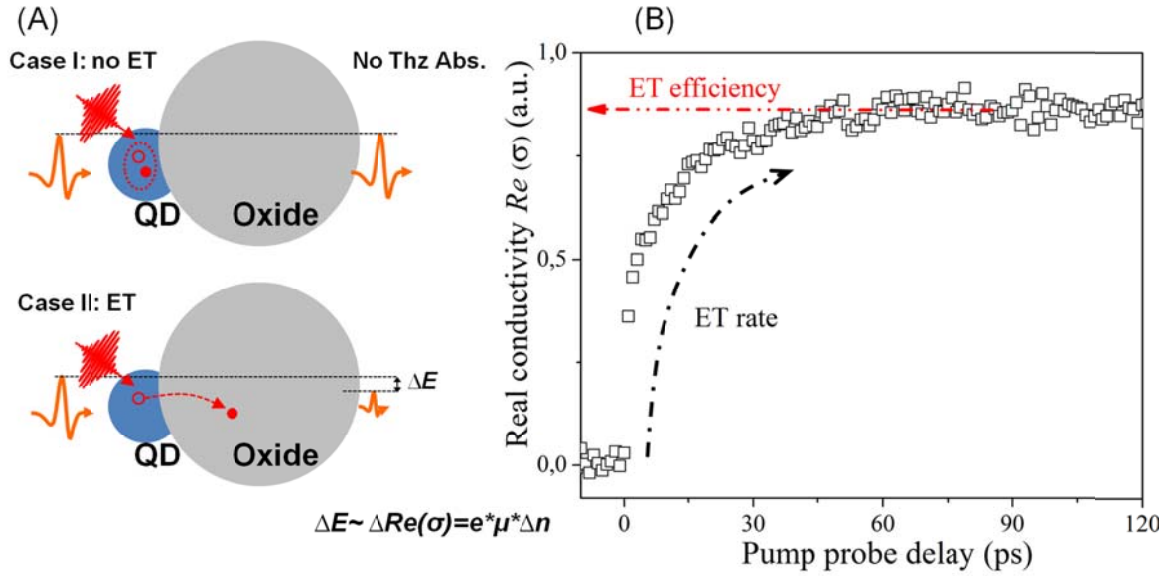

Figure 2.2 (A) Sketch illustrating the working principle of OPTP measurements on QD-sensitized oxides; (B) typical increase of the real conductivity component as a function of pump probe delay for case II (when ET occurs at the QD/oxide interface); while the rise of the signal after photo-excitation time resolved the ET dynamics from the QD to the oxide, the real conductivity value at the plateau (when ET has ended) is an indication of the process efficiency.

2.2 Sample preparation protocols

In this thesis we have followed 2 protocols for sensitizing the mesoporous oxide films by QDs. based on ex-situ synthesis of colloidal QDs and then functionalization of electrodes by a anchoring via a molecular linker. The second is based on in-situ nucleation of the dots onto oxide phases (bridgeless systems).

2.2.1 Preparation of metal oxide films

Commercial nanopowders of SnO_2 (Aldrich, < 100 nm), TiO_2 (Solaronix, Ti-Nanoxide) and ZnO (99%, Alfa Aesar, 20-30 nm) were used in this thesis for preparing thin oxide films. Two different kinds of substrates were employed: fused silica for optical pump-terahertz probe (OPTP) measurements. Prior to their use, the fused silica substrates were sand-blasted in order to enhance the adhesion of the films, this treatment do not affect THz transmission. The silica substrates were cleaned with ethanol (30 min) and acetone (30 min) in an ultrasonic bath before any deposition of oxide layers. Metal oxide films were deposited by doctor-blading aqueous slurry of the corresponding oxide over the cleaned substrates. The slurry was prepared by grinding 1 g of the oxide, 2 mL of H_2O, 30 μL of acetylacetone (99+%, Aldrich) and 30 μL of Triton X-100 (Aldrich). The samples were dried in air and sintered at 150 ºC (for 30 min) and 450 ºC (for 2 h) subsequently. The resulting films were measured to be ~7 μm in thickness by profilometry.

2.2.2 Ex-situ QD sensitization (QD-bridge-oxide system)

In the protocol of QD-linker-oxide sensitization, the colloidal QDs have to be produced first by wet-chemistry. For the CdSe QD used in the chapter 3, we have synthesized it by following the recipe from Mekis *et.al*. [11] Briefly, two precursors were prepared in the glovebox by dissolving 0.474 g Se powder (325 mesh) in 6 ml TOP (trioctylphosphine) and 0.36 g $Cd(Ac)_2$ in 9 ml TOP, respectively. Then, 24g TOPO (Trioctylphosphine oxide) was heated up to 180 °C in vacuum under periodic flushing with N_2. After cooling down to 100 °C, 15 g HDA (1-hexadecylamine) and 0.45 g TDPA (1-tetradecylphosphonic acid) were added and dried at 120 °C in vacuum during 30 min under periodic flushing with N_2. The TOP-Se precursor was subsequently injected and the solution was heated to 300 °C with N_2 protection. Under vigorous stirring, the TOP-$Cd(Ac)_2$ precursor was injected to induce nucleation of CdSe nanoparticles. During the growth at 280 °C aliquots were taken to monitor the growth rate. After 550 s the reaction was stopped by cooling down the remaining reaction volume to room temperature. At 55 °C 30 ml of toluene was injected to avoid solidification of the TOPO. The obtained dispersion was purified by repeated washing with MeOH and precipitation of particles in a centrifuge at 3000 rpm for 5 min. The wash process was repeated 3 times to get rid of extra capping molecules absorbing on the QD surface. The final stock of particles was dispersed in toluene and waiting for further usage.

For sensitization of oxides by QDs, the oxide films were firstly immersed for 12 h in a solution of 2 ml of acetonitrile containing 0.2ml of targeted molecular bridges. Afterwards, the films were washed thoroughly with acetonitrile and toluene to remove unbound bridges. As COOH groups are selectively linked to oxide surfaces,[12] the resulting bridge sensitized oxide surface is characterized by the presence of free SH groups that act as anchoring points for the QDs. The sensitization of the oxide film by QDs

is achieved by immersing it in a suspension of CdSe QDs in toluene for 12 h. Absorption measurements (Figure 2.3) evidenced that QD quantum confinement and QD size distribution is preserved on our sensitized samples (an example for CdSe QDs with ~3 nm diameter).

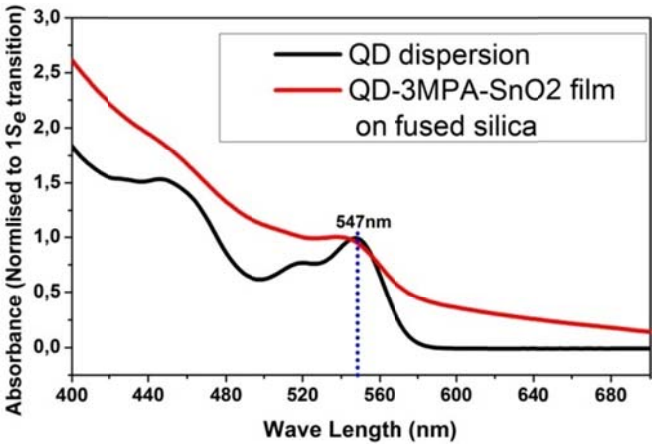

Figure 2.3 Absorption spectrum for 3nm diameter CdSe QDs in toluene (black trace) and when sensitizing a mesoporous SnO_2 film (bridge = 3-mercaptopropionic acid – 3MPA)

2.2.3 In-situ PbS QD sensitization by SILAR

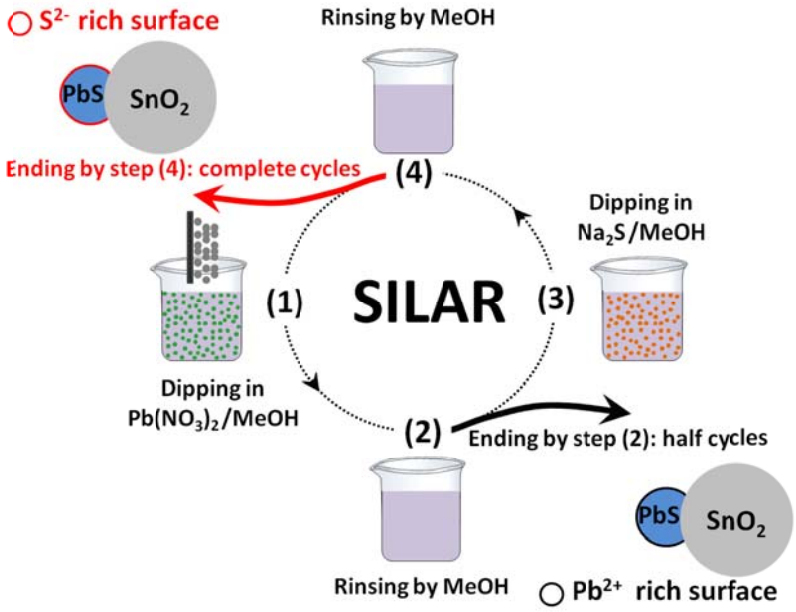

Figure 2.4 Sketch illustrating the steps for QD nucleation by SILAR process. The QD stoichiometry can be controlled (S- or Pb-rich surfaces) by finishing QD nucleation after immersion in the sulfur (complete cycle) or lead (half cycles) precursor solutions.

PbS QDs were directly grown on the mesoporous metal oxides films by the succesive ionic layer adsorption and reaction (SILAR) method in a glovebox with an O_2 level lower than 5 ppm. This procedure involves the adsorption of the cationic precursor (Pb^{2+}) on the oxide surface and, subsequently, its reaction with the anionic precursor (S^{2-}) leading to the formation of PbS on the surface of the corresponding oxide nanoparticles. Concretely, as schematically shown in figure 2.4(growing PbS on SnO_2 as an example), the samples were (1) dipped in a saturated solution of 0.1 M $Pb(NO_3)_2$ (99+%, Aldrich) in methanol (99.9 %, Scharlau), (2) rinsed in pure methanol, (3) inmersed into a solution 0.1 M Na_2S (Aldrich) in methanol and, finally (4) rinsed in pure methanol. This set of steps is called a SILAR cycle. The films were soaked in each solution for 1 min.

UV-visible diffuse reflectance spectra were recorded using a Shimadzu UV-2401 with an integrating sphere using $BaSO_4$ (Wako) as background. Figure 2.5 shows the Kubelka-Munk transformation of the reflectance spectra for SnO_2 films on fused silica before and after being sensitized with different number of SILAR cycles. As the number of cycles increases, the entire spectrum shifts toward the red indicating that the nanocrystal size grows.

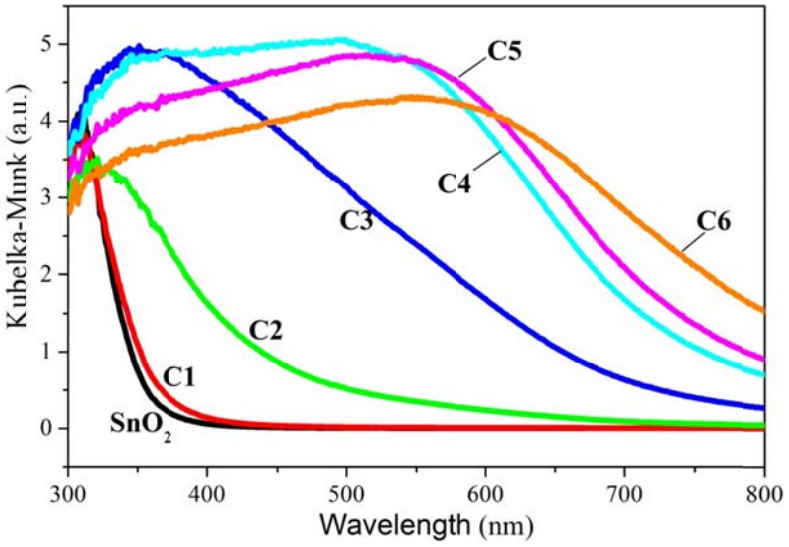

Figure 2.5 UV-vis diffuse reflectance spectra (Kubelka-Munk transformation)for SnO_2 films before and after deposition of PbS QDs with different SILAR cycles (Cn with n=1-6).

2.2.4 Molecular passivation of PbS QDs

In the charpter 5, we will disucss the effect of ligands at QD surfaces on interfacila ET dynamics. For that, various molecules have been used and the procedure is described in the following. The passivating of QDs is done by dipping sensitized film into 0.1 M molecular solution (in methonal) of interested by 120 minutes with stering (300 rpm). All molecules are perchased from Sigma Aldrich.

2.2.5 Coating of SiO_2 at SnO_2 surfaves

Coating of SiO_2 at SnO_2 nanoparticle has been reported before.[13] All coating poresecure is finished inside glovebox. In short, 0.15 M of silicon methoxide in dry methanol is used as precursor solutions. We then dip SnO_2 porous film into the precusor solution for 5 mins and baked for another 5 minute. This procedure is repeated once for 2 layer of coating. Eventually, the coated film is transferred to an oven out side of glove box, and a sintering at 435 °C for 30 min is followed.

2.3 Differential analysis: error estimation and reproducibility tests in ET efficiency measurements

An important part of this thesis has been devoted to correlate the ET efficacy and device performance in QDSSCs. For that, the magnitude of dynamics has been compared with/without certain treatments. For making the comparison statistically meaningful, we have (1) put samples into high vacuum ($1.4*10^{-4}$ mbar) during measurements to avoid oxidation; (2) The measurement reproducibility has been tested by measuring the variation of signal for a given sample at different points (5-10 points). As given an example in figure 2.6 for a 2 SILAR cycle PbS QDs on SnO_2 before passivation, the ET dynamics of 5 different points A-E (a schematic illustration shown in the inset) of a pre-marked spots gives a *mean square error* of ~3%. The variation of signal at plateau ranges from 3 and 10% from sample to sample (depending on the smoothness of the oxide film), which is statistically much smaller than the relatively change of ET efficiency after molecular passivation (~50% -120% increase)

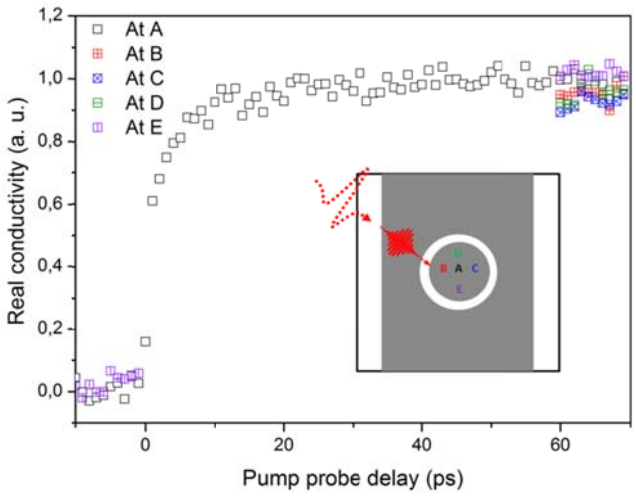

Figure 2.6 The reproducibility test of ET dynamics on 2 SILAR cycle PbS QDs on SnO_2. The inset illustrates how we measure and estimate the variation of signal by keeping measuring at 5 different points of the same spot.

References

1. Yang, Y.; Rodriguez-Cordoba, W.; Xiang, X.; Lian, T. Q. *Nano Lett* **2012,** 12, (1), 303-309.
2. Tisdale, W. A.; Williams, K. J.; Timp, B. A.; Norris, D. J.; Aydil, E. S.; Zhu, X. Y. *Science* **2010,** 328, (5985), 1543-1547.
3. Tisdale, W. A.; Zhu, X. Y. *P Natl Acad Sci USA* **2011,** 108, (3), 965-970.
4. Ulbricht, R.; Hendry, E.; Shan, J.; Heinz, T. F.; Bonn, M. *Rev Mod Phys* **2011,** 83, (2), 543-586.
5. Schmuttenmaer, C. A. *Chem Rev* **2004,** 104, (4), 1759-1779.
6. Ferguson, B.; Zhang, X. C. *Nat Mater* **2002,** 1, (1), 26-33.
7. Rui, L.; Gu, C. M.; He, L. R.; Sen, W.; Shen, W. Z.; Hiroshi, O.; Guo, Q. X. *Acta Phys Sin-Ch Ed* **2004,** 53, (4), 1217-1222.
8. Pijpers, J. J. H.; Koole, R.; Evers, W. H.; Houtepen, A. J.; Boehme, S.; Donega, C. D.; Vanmaekelbergh, D.; Bonn, M. *J Phys Chem C* **2010,** 114, (44), 18866-18873.
9. Canovas, E.; Moll, P.; Jensen, S. A.; Gao, Y. A.; Houtepen, A. J.; Siebbeles, L. D. A.; Kinge, S.; Bonn, M. *Nano Lett* **2011,** 11, (12), 5234-5239.
10. Zidek, K.; Zheng, K. B.; Abdellah, M.; Lenngren, N.; Chabera, P.; Pullerits, T. *Nano Lett* **2012,** 12, (12), 6393-6399.
11. Mekis, I.; Talapin, D. V.; Kornowski, A.; Haase, M.; Weller, H. *J Phys Chem B* **2003,** 107, (30), 7454-7462.
12. Robel, I.; Subramanian, V.; Kuno, M.; Kamat, P. V. *J Am Chem Soc* **2006,** 128, (7), 2385-2393.
13. Palomares, E.; Clifford, J. N.; Haque, S. A.; Lutz, T.; Durrant, J. R. *J Am Chem Soc* **2003,** 125, (2), 475-482.

Chapter 3

Tuning Electron Transfer Rates through Molecular Bridges in Quantum Dot Sensitized Oxides*

Photo-induced electron transfer processes from semiconductor quantum dots molecularly bridged to a mesoporous oxide phase are quantitatively surveyed using optical pump-THz probe spectroscopy. We control electron transfer rates in donor-bridge-acceptor systems by tuning the electronic coupling strength through the use of n-methylene (SH-$[CH_2]_n$-COOH) and n-phenylene (SH-$[C_6H_4]_n$-COOH) molecular bridges. Our results show that electron transfer occurs as a non resonant quantum tunneling process with characteristic decay rates of $\beta_n = 0.94 \pm 0.08$ and $\beta_n = 1.25$ per methylene and phenylene group respectively; in quantitative agreement with reported conductance measurements through single molecules and self-assembled monolayers. For a given QD donor-oxide acceptor separation distance, the aromatic n-phenylene based bridges allow faster electron transfer processes when compared with n-methylene based ones. Implications of these results for QD sensitized solar cell design are discussed.

3.1 Introduction

While metal oxides constitute robust and relatively cheap semiconductor materials that are finding increasing applications in optoelectronics, their band gaps are typically prohibitively wide for the generation of electron-hole pairs through the absorption of visible light. Several approaches have been developed to circumvent this drawback. Specifically, the sensitization of mesoporous oxides by semiconductor quantum dot (QD) nanocrystals represents a promising route for the development of low cost solutions for energy production (i.e. in QD sensitized solar cells[1-3]) and storage (i.e. in photocatalyst for water splitting[4, 5]). In a common approach for the sensitization of mesoporous oxide films with QDs, bi-functional molecular linkers are employed, for which each end of the molecule selectively anchors to the donor and acceptor, respectively[6-9]. This configuration has been termed a

** Adapted with permission from (Nano Letters, 2013, 13 (11), pp 5311–5315). Copyright (2013) American Chemical Society.*

donor-bridge-acceptor system[10], where the bridge imposes a barrier potential (φ) that has to be overcome in order for electron transfer (ET) to occur (see figure 3.1). The barrier potential height is a direct measure of the donor-acceptor electronic coupling strength, and the ET rate is expected to decrease exponentially with both barrier height and bridge length[10]. Despite the apparent relevance for molecularly engineered novel and more efficient quantum dot-sensitized systems, little quantitative information exists regarding the role of the molecular bridge on the ET process. Existing studies have shown that the nature of the molecular bridge affects the ET processes[7-9] but are largely of a qualitative nature. This lack in our knowledge has been attributed to the challenge of quantifying ultrafast electron transfer processes in a non-contact fashion in these *a priori* highly heterogeneous systems[10, 11].

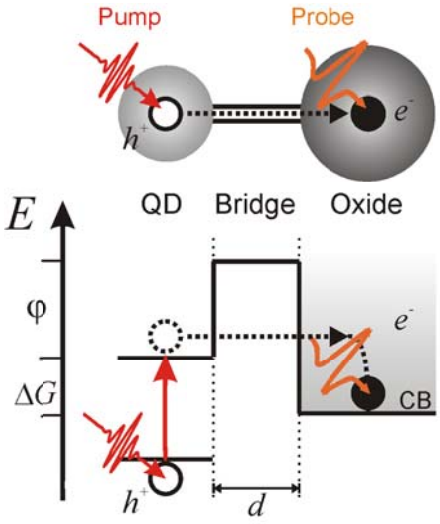

Figure 3.1 Principle of operation for time resolved THz photoconductivity measurements and sketch of the energetics of the QD-bridge-oxide system; After selective absorption of a femtosecond optical pump pulse (red) by the QD, electron transfer through the molecular bridge to the oxide can occur (dashed arrow). Free electrons (e^-) populating the oxide conduction band (CB) can be selectively probed through their photoconductive response by a freely propagating THz pulse (orange). The excess energy ΔG of electrons in the QD excited state relative to the oxide conduction band (i.e. the driving force for electron transfer) triggers the electron transfer through a barrier potential of height φ and width d defined by the lowest unoccupied molecular orbital (LUMO) level of the molecular bridge.

3.2 Methods and Materials

In previous work, we have demonstrated the unique potential of optical pump THz probe (OPTP) measurements for interrogating ET processes on QD sensitized oxide films[12, 13]. The strength of the technique relies on its ability to measure the complex (real and imaginary) photoconductivity of the sample after optical excitation with sub-picosecond time resolution[14]. As long as charge carriers are confined within the QDs, the pump-induced real photoconductivity is zero; as soon as charges are transferred to the oxide, the carriers are free to move and the real conductivity becomes finite. A

gradual increase in the real conductivity with time after photo-excitation therefore directly and unambiguously reflects the ET processes taking place from the QD to the oxide. However, we have reported previously[12, 13] that there is an additional, instantaneous contribution to the real conductivity upon photo-excitation due to free carriers populating QD aggregates. Here, we show how deliberate photo-oxidation of the sample allows us to separate out this parasitic signal to obtain pure ET kinetics.

As an example of the methodology, we show in figure 3.2 the characteristic photo-oxidation OPTP dynamics for a sample consisting of ~3nm diameter CdSe QDs sensitizing a mesoporous SnO_2 film by 4-mercaptobutyric acid (HS-$[CH_2]_3$-COOH). A detailed description of the sample preparation is given in chapter 2 sample preparation part. The solid black trace in figure 3.2 is the time resolved real conductivity signal for a sample preserved from photo-oxidation (prepared and measured under nitrogen environment). The real conductivity response of the sample is characterized by an instantaneous rise of the conductivity at time zero (attributed to photoconductivity within QD aggregates[12, 13]) followed by a fast decay (due to trapping or recombination within those QD aggregates) and a picosecond timescale rise of the conductivity. Note that only the slow rise of the real conductivity signal (indicating an increasing population of free carriers in the oxide) is related to the ET process of interest.

Photo-oxidation of the sample is achieved by exposing the sample to air under identical optical excitation conditions (in this case 12 hours with 400 nm pulses at 1 kHz at a fluence of 40 $\mu J/cm^2$, dotted black trace in figure 3.2). Photo-oxidation of QDs causes quenching of QD luminescence[15, 16], as a result of the generation of electron traps in the QD surface. The generation of these traps also can prevent ET from QDs to the oxide phase[13, 17], which is apparent in our measurements from the disappearance of the time-dependent ingrowth of the photoconductivity upon photo-oxidation (figure 3.2, dotted line). The instantaneous signal due to aggregated QDs remains, being a bulk signal that is less sensitive to the state of QDs at the surface of these aggregates. Hence, by comparing photoconductivity dynamics in the pristine sample with that in a photo-oxidized sample, for which ET is strongly suppressed, we can resolve unambiguously the ET component of interest. The green trace in figure 3.2 is obtained by subtracting OPTP traces with different degree of oxidation (solid and dotted black traces in figure 3.2). The resulting dynamics can be well described by a single exponential function allowing for straightforward quantification of ET from the QD to the oxide. In Appendix 3.5.1 attached to this chapter (see figure 3.6), we show that our methodology give very good sample to sample reproducibility.

Two important observations must be made here: (i) The inferred kinetics are independent of the degree of photo-oxidation for the two comparative measurements; (ii) while the parasitic signal can vary strongly between different samples, or even different spots on the same sample, our photo-oxidation protocol gives reproducible ET kinetics from sets of samples made with the same recipe. It is

remarkable to note that *monophasic* kinetics describe our measurements extremely well. This result implies that, following Marcus theory[18], most of our QD sensitizers experience similar energetics (ΔG) and donor-acceptor electronic coupling strengths ($|H_{DA}|^2$), challenging the a priori intuition of ET heterogeneity for mesoporous systems. A detailed analysis of the degree of ET heterogeneity for different mesoporous oxides is in progress and will be reported elsewhere.

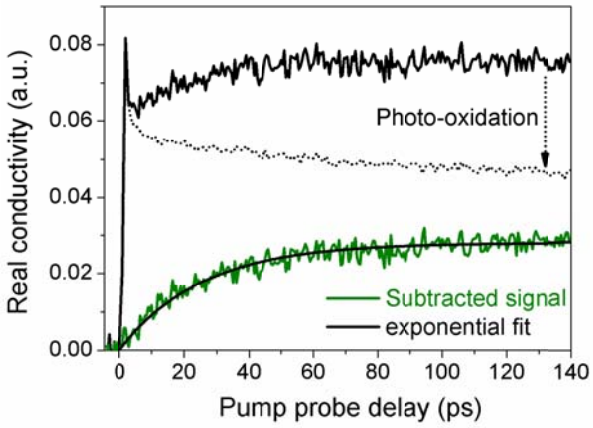

Figure 3.2 Characteristic evolution of the pump induced photoconductivity dynamics monitored by OPTP on CdSe QDs sensitizing SnO_2 connected by a HS-$[CH_2]_3$-COOH bridge, for the *un-oxidized* sample (top black trace) and after 12 hours exposure to air and 400 nm radiation (photo-oxidation process, black dotted trace). The green trace at the bottom is the difference between the two traces experiencing different degree of photo-oxidation and provides the kinetics of the real ET process. The black solid line is the corresponding single exponential fit.

3.3 Results and Discussions

In order to study how the nature and length of the molecular bridge between QD donor and oxide acceptor affects ET rates, we investigate bridges based on n-methylene (HS-$[CH_2]_n$-COOH, n = 1,3,5,7) and n-phenylene (HS-$[C_6H_4]_n$-COOH; n = 1,2) backbones. The bridges form the connection between ~3nm diameter CdSe QDs and SnO_2 nanoparticles, corresponding to a fixed driving force for ET of $\Delta G \sim 1.1$eV[18, 19]. Figure 3.3 a and b depict the obtained ET kinetics for the two types of analyzed molecules; in both cases a slow-down of the ET rate with increasing bridge length is apparent. Also here, the ET kinetics can be described very well by single exponential functions (black solid lines in figure 3.3 (a) and (b)). Table 1 summarizes the extracted ET rates for all molecular bridges considered in this study, and the lengths of the corresponding gas-phase molecules as obtained through density-functional theory (DFT) calculations. The kinetics of each sample was monitored within sufficiently large time windows to allow resolving the signal plateau (indicating that the ET process is complete). Only for the two largest n-methylene based bridges our experimental time window (0-1100 ps, limited by the length of the optical delay line) was insufficient to clearly resolve the plateau in the OPTP traces (see figure 3.3a), increasing the uncertainty in the inferred value for the ET rate (table 1).

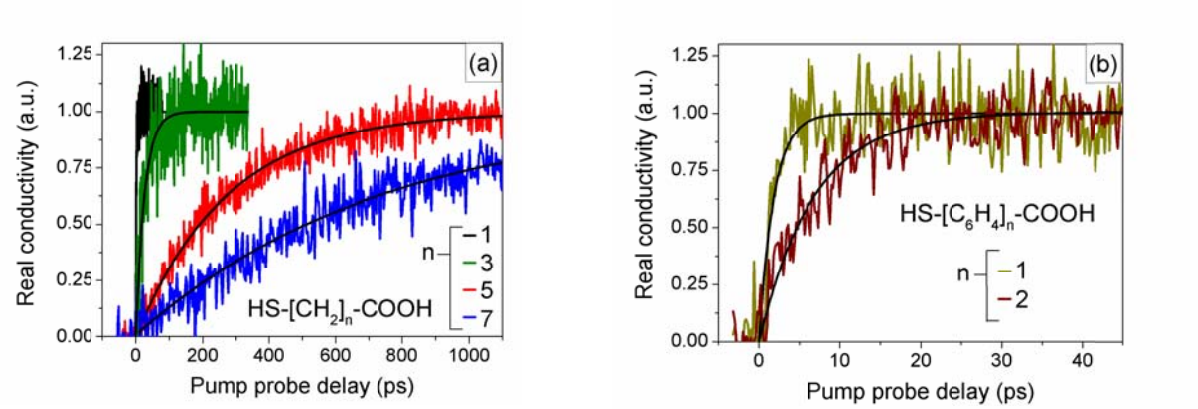

Figure 3.3 ET kinetics between ~3nm CdSe QDs and SnO_2 through (a) n-methylene based bridges (HS–$[CH_2]_n$-COOH, with n=1,3,5,7) and (b) n-phenylene based bridges (HS–$[C_6H_4]_n$-COOH, with n=1,2). Black lines depict single exponential fits.

Bridge HS-$[X]_n$-COOH	**Molecular length (Å)**	**ET time τ_{ET} (ps)**	**Rate constant k_{ET} (s^{-1})**
$[CH_2]_1$	4.0	3 ± 1	$3.33 \cdot 10^{11}$
$[CH_2]_3$	6.5	25 ± 2	$4.00 \cdot 10^{10}$
$[CH_2]_5$	9.0	225 ± 5	$4.44 \cdot 10^{9}$
$[CH_2]_7$	11.5	758 ± 10	$1.32 \cdot 10^{9}$
$[C_6H_4]_1$	6.7	2 ± 1	$5.00 \cdot 10^{11}$
$[C_6H_4]_2$	11.0	7 ± 2	$1.42 \cdot 10^{11}$

Table 1 QD/oxide ET times and rates extracted from fitting procedures for all molecular bridges considered in this study and lengths of the corresponding gas-phase molecules obtained through DFT calculations.

Figure 3.4 shows the evolution of ET rates as a function of nominal length for bridges based on n-methylene (HS-$[CH_2]_n$- COOH, n = 1,3,5,7) and n-phenylene (HS-$[C_6H_4]_n$-COOH; n = 1,2) backbones. In the case of n-methylene based molecules, the ET rate decays exponentially with bridge length. Indeed, as shown in figure 3.4 (black solid line), the data is well described as a non-resonant coherent tunneling process (where the electron never resides on the bridge; the so called superexchange mechanism[10, 20]) which predicts $k_{ET}(d) = k_{ET}(0) \cdot exp[-\beta \cdot d]$, where d is the distance between donor and acceptor states, $k_{ET}(0)$ the ET rate at $d = 0$ and β is the characteristic tunnelling decay rate for a given barrier potential (see figure 3.1). While the size of the n-phenylene data set leaves room for the possibility of ET being dominated by other mechanisms (e.g. electron hopping[10]), we assume here that the charge transfer through the n-phenylene based bridges is also mediated by

non-resonant coherent tunnelling (red solid line in figure 3.4), in agreement with reported conductance measurements[21, 22]. We obtain for the n-phenylene bridges a tunnelling decay rate of β_n= 0.29 Å^{-1} (or equivalently β_n = 1.25 per phenylene group) while for the n-methylene bridges β_n = 0.75 ± 0.06 Å^{-1} (or β_n = 0.94 ± 0.08 per methylene group). Within the superexchange model, the tunnelling decay rate takes the form β=-(2/a)·ln(H_{ob}/ΔE_{bb}); where H_{ob} is the internal coupling energy between bridge units, a is the bridge-unit length, and ΔE_{bb} is the energy of the mediating tunnelling state above the donor ground state. Accordingly, small barrier heights and/or strong bridge unit coupling lead to small β coefficients and large conductance in the donor-bridge-acceptor system. As shown in figure 3.5, our theoretical calculations illustrate the origin of the large difference in inferred β's: the n-methylene bridges are characterized by highest occupied (HOMO) and lowest unoccupied molecular orbitals (LUMO) strongly localized to either end of the bridge, with a large HOMO-LUMO gap and LUMO level very close to the ionization threshold. The higher-lying virtual orbitals located on the central moiety are similarly weakly coupled. In contrast to the n-methylene bridge, the frontier orbitals in the n-phenylene molecule delocalize across the entire molecule, with both HOMO and LUMO showing significant weight at both ends, and a significantly lower lying LUMO level. This qualitative difference holds true for all linkers employed in this study independent of their length.

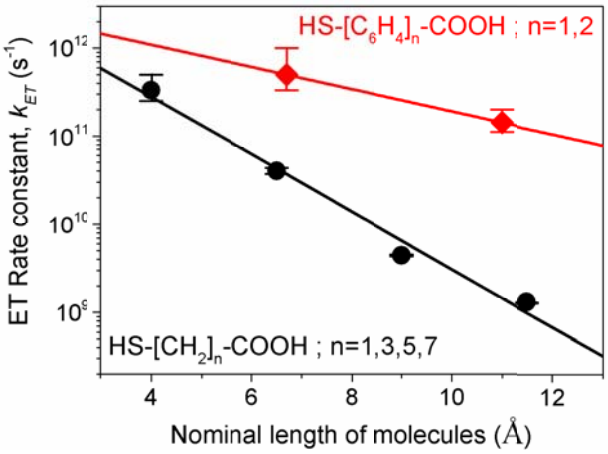

Figure 3.4 Estimated ET rate constants vs molecular bridge length for n-methylene based bridges (HS–$[CH_2]_n$-COOH, with n=1,3,5,7; black dots) and n-phenylene based bridges (HS–$[C_6H_4]_n$-COOH, with n=1,2; red squares). Solid lines are best fits to $k_{ET}(d) = k_{ET}(0)\cdot exp[-\beta\cdot d]$ as discussed in the text.

Finally, it is worth noting that our obtained β figures agree quantitatively with values reported from conductance measurements through single molecules[21, 23] and self-assembled monolayers[22, 24]. This agreement strongly supports our results (and methodology) and indicates that conductance and ET rates are indeed closely correlated as theoretically predicted by Nitzan[25]. In conductance measurements the current is measured while varying the DC bias, resulting in J-V curves. The equivalent of varying bias for ET measurements is changing QD size[6, 13, 18], which controls the ET driving force ΔG (see figure 3.1). Note that β values have been shown to be practically independent of

DC bias in molecular conductance measurements[23], consistent with the notion that in the expression for ET rates $k_{ET}(d) = k_{ET}(0) \cdot exp[-\beta \cdot d]$, ΔG co-determines the prefactor $k_{ET}(0)$.

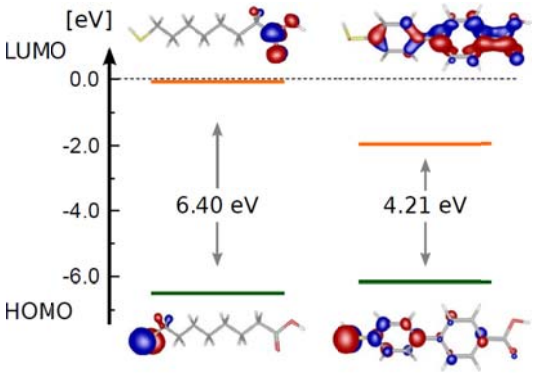

Figure 3.5 Energetic and spatial distribution of the frontier orbitals of HS–$[CH_2]_7$-COOH (left) and HS–$[C_6H_4]_2$-COOH (right) molecules, calculated using DFT.

3.4 Summary

In this work we have contributed to clarifying how ET processes are influenced and can be tuned by molecular bridges of different nature and length anchoring QDs to oxide nanoparticles on sensitized systems. For the studied samples, we find that the molecular bridges sandwiched between QD donor and oxide acceptor act as simple resistors to current flow. Similar results have been reported for studies of the tunneling decay rate through an inorganic barrier layer (the shell of a core-shell QD)[26, 27]. Our findings have implications for the design of QD sensitized solar cells. In these architectures small donor-acceptor energetics (driving forces ΔG, see figure 3.1) are desired to enhance potential photoconversion efficiencies[28]. However, small driving forces necessarily imply slow ET rates[13, 18] and then competing relaxation processes within the QDs can quench the output photocurrent in devices. The employment of more conductive molecular bridges (e.g. phenylene vs methylene ones) can counterbalance kinetically that effect and hence improved solar cell efficiencies are in principle within reach. In a complete sensitized solar cell based on a molecular bridge imposing the barrier for current flow between donor and acceptor, we expect that the presence of a hole conducting phase (e.g. electrolyte solution) will likely affect ET rates but not the ET (tunnelling) mechanism.

Integrating the concepts of molecular electronics into QDSSCs could further help us choosing functional bridges allowing fast unidirectional ET from donor to acceptor. For example, the employment of molecular bridges showing rectifying behavior between donor and acceptor could potentially prevent back electron recombination from the oxide to the electrolyte or/and from the oxide to the QDs. These recombination pathways are indeed critical for the solar cell performance[3], and their suppression will result in higher photocurrents and hence efficiencies. Finally, in this work we prove

that for given system energetics (ΔG in figure 3.1) ET rates in QD sensitized systems can be tuned over several orders of magnitude by appropriate system design.

3.5 Appendix

3.5.1 Photo oxidation protocol – sample to sample reproducibility

As discussed in the paper, by deliberate photo-oxidation of the samples we claim to be able to differentiate between the pure ET component on our OPTP traces and contributing parasitic signals (e.g. recombination processes in QD aggregates). To check the validity of our approach and rule out changes in the obtained kinetics dependent on the monitored sample's preparation history, we applied the photo-oxidation protocol on sets of samples made under the same recipe. An example is shown in figure 3.6; while the OPTP kinetics resolved before photo-oxidation can be clearly different from sample to sample (e.g. compare figure 3.6 (A) plot's solid red and blue traces), this is only due to the fact that parasitic signals can vary strongly among them, or even among different spots on the same sample. In figure 3.6 (B), by following our photo-oxidation protocol (in this case 12 hours with 400nm pulses at 1 kHz at a fluence of 40 μJ/cm2) we were able to resolve nearly identical ET kinetics from sets of samples made with the same recipe (in this case, CdSe QDs sensitizing SnO_2 connected by a HS-$[CH_2]_3$-COOH molecule). In this respect, fittings to single exponential functions gave us also comparable ET rates (25.3 ±1ps) within our experimental noise.

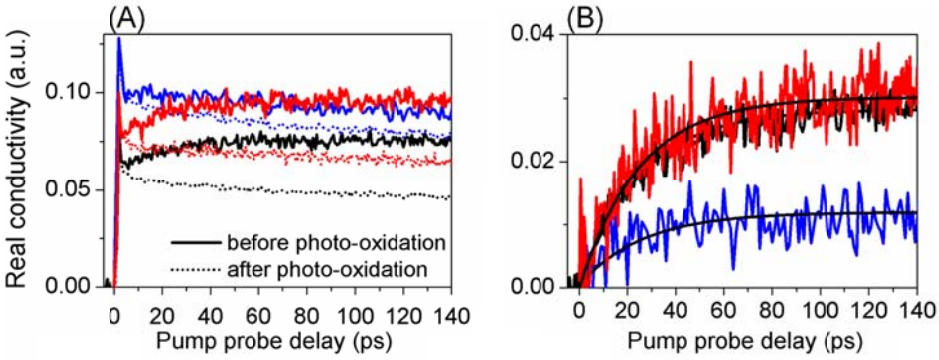

Figure 3.6 (A) Characteristic response of the pump induced photoconductivity dynamics for 3 samples consisting of CdSe QDs sensitizing SnO_2 connected by a HS-$[CH_2]_3$-COOH bridges before (solid lines) and after (dotted lines) 12h of photo-oxidation. (B) Subtracted kinetics and fittings to single exponential functions. As stated in the text, the obtained ET rates are identical within experimental error.

References

1. Kamat, P. V. *The Journal of Physical Chemistry C* **2008,** *112*, (48), 18737-18753.

2. Rühle, S.; Shalom, M.; Zaban, A. *ChemPhysChem* **2010,** *11*, (11), 2290-2304.

3. Mora-Seró, I.; Bisquert, J. *The Journal of Physical Chemistry Letters* **2010,** *1*, (20), 3046-3052.

4. Li, Y.; Zhang, J. Z. *Laser & Photonics Reviews* **2010,** *4*, (4), 517-528.

5. Chen, H. M.; Chen, C. K.; Chang, Y.-C.; Tsai, C.-W.; Liu, R.-S.; Hu, S.-F.; Chang, W.-S.; Chen, K.-H. *Angewandte Chemie* **2010,** *122*, (34), 6102-6105.

6. Robel, I.; Subramanian, V.; Kuno, M.; Kamat, P. V. *Journal of the American Chemical Society* **2006,** *128*, (7), 2385-2393.

7. Dibbell, R. S.; Watson, D. F. *The Journal of Physical Chemistry C* **2009,** *113*, (8), 3139-3149.

8. Dibbell, R. S.; Youker, D. G.; Watson, D. F. *The Journal of Physical Chemistry C* **2009,** *113*, (43), 18643-18651.

9. Hyun, B.-R.; Bartnik, A. C.; Sun, L.; Hanrath, T.; Wise, F. W. *Nano Letters* **2011,** *11*, (5), 2126-2132.

10. Adams, D. M.; Brus, L.; Chidsey, C. E. D.; Creager, S.; Creutz, C.; Kagan, C. R.; Kamat, P. V.; Lieberman, M.; Lindsay, S.; Marcus, R. A.; Metzger, R. M.; Michel-Beyerle, M. E.; Miller, J. R.; Newton, M. D.; Rolison, D. R.; Sankey, O.; Schanze, K. S.; Yardley, J.; Zhu, X. *The Journal of Physical Chemistry B* **2003,** *107*, (28), 6668-6697.

11. Watson, D. F. *The Journal of Physical Chemistry Letters* **2010,** *1*, (15), 2299-2309.

12. Pijpers, J. J. H.; Koole, R.; Evers, W. H.; Houtepen, A. J.; Boehme, S.; de Mello Donegá, C.; Vanmaekelbergh, D.; Bonn, M. *The Journal of Physical Chemistry C* **2010,** *114*, (44), 18866-18873.

13. Cánovas, E.; Moll, P.; Jensen, S. A.; Gao, Y.; Houtepen, A. J.; Siebbeles, L. D. A.; Kinge, S.; Bonn, M. *Nano Letters* **2011,** *11*, (12), 5234-5239.

14. Ulbricht, R.; Hendry, E.; Shan, J.; Heinz, T. F.; Bonn, M. *Reviews of Modern Physics* **2011,** *83*, (2), 543-586.

15. Sykora, M.; Koposov, A. Y.; McGuire, J. A.; Schulze, R. K.; Tretiak, O.; Pietryga, J. M.; Klimov, V. I. *ACS Nano* **2010,** *4*, (4), 2021-2034.

16. van Sark, W. G. J. H. M.; Frederix, P. L. T. M.; Van den Heuvel, D. J.; Gerritsen, H. C.; Bol, A. A.; van Lingen, J. N. J.; de Mello Donegá, C.; Meijerink, A. *The Journal of Physical Chemistry B* **2001,** *105*, (35), 8281-8284.

17. Hines, D. A.; Becker, M. A.; Kamat, P. V. *The Journal of Physical Chemistry C* **2012,** *116*, (24), 13452-13457.

18. Tvrdy, K.; Frantsuzov, P. A.; Kamat, P. V. *Proceedings of the National Academy of Sciences* **2011,** *108*, (1), 29-34.

19. Jasieniak, J.; Califano, M.; Watkins, S. E. *ACS Nano* **2011,** *5*, (7), 5888-5902.

20. McConnell, H. M. *Journal of Chemical Physics* **1961,** *35*, 8.

21. Venkataraman, L.; Klare, J. E.; Nuckolls, C.; Hybertsen, M. S.; Steigerwald, M. L. *Nature* **2006,** *442*, (7105), 904-907.

22. Wold, D. J.; Haag, R.; Rampi, M. A.; Frisbie, C. D. *The Journal of Physical Chemistry B* **2002,** *106*, (11), 2813-2816.

23. Xu, B.; Tao, N. J. *Science* **2003,** *301*, (5637), 1221-1223.

24. Hylke, B. A.; Bert de, B. *Journal of Physics: Condensed Matter* **2008,** *20*, (1), 013001.

25. Nitzan, A.; Ratner, M. A. *Science* **2003,** *300*, (5624), 1384-1389.

26. Zhu, H.; Song, N.; Lian, T. *Journal of the American Chemical Society* **2010,** *132*, (42), 15038-15045.

27. Dworak, L.; Matylitsky, V. V.; Breus, V. V.; Braun, M.; Basché, T.; Wachtveitl, J. *The Journal of Physical Chemistry C* **2011,** *115*, (10), 3949-3955.

28. Giebink, N. C.; Wiederrecht, G. P.; Wasielewski, M. R.; Forrest, S. R. *Physical Review B* **2011,** *83*, (19), 195326.

Chapter 4

Interplay between Structure, Stoichiometry and Electron Transfer Dynamics in SILAR-based Quantum Dot-Sensitized Oxides

We quantify the rate and efficiency of picosecond electron transfer (ET) from PbS nanocrystals, grown by successive ionic layer adsorption and reaction (SILAR), into a mesoporous SnO_2 support. Successive SILAR deposition steps allow for stoichiometry- and size-variation of the QDs, characterized using transmission electron microscopy. Whereas for sulfur-rich (p-type) QD surfaces substantial electron trapping at the QD surface occurs, for lead-rich (n-type) QD surfaces, the QD trapping channel is suppressed and the ET efficiency is boosted. The ET efficiency increase achieved by lead-rich QD surfaces is found to be QD-size dependent, increasing linearly with QD surface area. ET rates, on the other hand, are found to be independent of both QD size and surface stoichiometry, suggesting that the donor-acceptor energetics (constituting the driving force for ET) are fixed, due to Fermi level pinning at the QD/oxide interface. Implications of our results for QD-sensitized solar cell design are discussed.

4.1 Introduction

The sensitization of wide bandgap oxides by quantum dots (QDs) represents a promising route for the development of low-cost solar energy conversion devices (e.g. photovoltaics[1-6] and photocatalysis[7]). The QD synthesis can be performed either *ex situ*, *i.e.* colloidal dots are prepared and then directly adsorbed on or molecularly linked to the oxide,[2] or *in situ,* with nanocrystals directly nucleated and grown onto the oxide matrix,[6, 8, 9] for example through chemical bath deposition (CBD)[10, 11] or successive ionic layer adsorption and reaction (SILAR).[6, 8, 12, 13] The *ex-situ* approach provides a path for obtaining highly monodisperse QDs, but commonly suffers from the formation of QD aggregates

* *Adapted with permission from (Nano Letters.*, 2014, 14 (10), pp 5780–5786*). Copyright (2014) American Chemical Society.*

and/or limited QD surface coverage (constrained by oxide pore size). Electronically, the QD capping shell and/or the molecular bridges linking the QDs to the oxide can act as an insulating barrier to electron transfer; for aromatic and aliphatic molecular bridges, charge transfer has been shown to proceed via coherent tunneling, slowing down with increasing bridge length.[14] On the other hand, *in-situ* QD sensitization potentially enables hetero-epitaxial growth which allows morphologically well-defined QD donors,[15-18] and can offer larger QD surface coverage in mesoporous oxide architectures compared to the *ex-situ* approaches. Moreover, the intimate QD/oxide contact is expected to provide the strongest achievable electronic coupling for a given donor/acceptor system. This particular property could enable ultrafast and efficient QD-to-oxide ET processes at little to no energy cost, allowing to reach the ultimate theoretical ~30% Shockley-Queisser limit for photon-to-electron energy conversion in sensitized systems.[19]

Previous reports on *in-situ* nucleated QDs have, however, suggested wide QD size distributions and a lack of control over the nanocrystal morphology.[17] This has been primarily concluded from the featureless QD absorbance, which can also be an intrinsic manifestation of the strong donor-acceptor electronic wavefunction overlap.[20, 21] Among the existing *in-situ* methodologies, the SILAR method allows low-temperature-solution-processed epitaxial thin film growth[22, 23] and SILAR-based QD-sensitized solar cells with efficiencies exceeding 5% have been reported.[5, 6] The strengths of the SILAR approach to grow QDs on metal oxides lie in the fact that (i) the size of the QD can be controlled, to some extent, by the number of deposition cycles;[24, 25] and (ii) the QD surface stoichiometry can be easily tuned[26], opening new possibilities for QD doping[27-30] and providing a path for atomically passivated dots[31, 32]. Additionally, highly monodisperse core/shell colloidal QDs can be obtained when this sensitization methodology is applied.[32] Despite the apparent potential of this approach, several important questions concerning SILAR-based QD-sensitized oxides remain open; clear correlations between chemical synthesis, QD structure and stoichiometry, donor-acceptor charge transfer dynamics and their impact on device performance are lacking.

Here, we investigate the interplay between QD structure, stoichiometry, and electron transfer rate and efficiency in SILAR-based PbS QD-sensitized tin oxides as a function of SILAR deposition steps. TEM analysis indicates that the size of PbS QDs is controlled through sequential epitaxial deposition steps, as is the stoichiometry. Optical pump-THz probe (OPTP) spectroscopy reveals electron transfer (ET) rates independent of QD size and surface chemistry, indicative of Fermi level pinning at the QD/oxide interface. In contrast to the ET rate, the ET efficiency from PbS QDs directly nucleated onto a mesoporous oxide is very sensitive to the QD surface composition, being substantially enhanced for lead-rich surfaces. Finally, we correlate our OPTP photoconductivity measurements with photocurrent generation in QD-sensitized solar cells (QDSSCs), highlighting the relevance of our observations for solar cell design.

4.2 Methods and Materials

We characterize ET processes on QD-sensitized oxides using OPTP spectroscopy[14, 33-36] with sub-picosecond time resolution. Owing to its low photon energy, terahertz radiation is insensitive to optical transitions in QDs[35]; however, because the THz probe is absorbed by mobile carriers populating the oxide conduction band, the photo-induced THz absorption is directly related to the photoconductivity of the sample. Hence, following optical excitation of the QD, the time-dependent pump-induced absorption of the THz probe in a QD-sensitized system can be directly correlated with ET from the QDs to the oxide.[14, 33, 34] Note that as discussed in chapter 2, not only the ET rate but also the efficiency of the ET process can be obtained from OPTP measurements, through the amplitude of the photo-induced THz absorption.

Sensitization of a mesoporous SnO_2 matrix with PbS QDs was achieved by alternatively dipping the oxide film (up to 6 times) into beakers containing a (i) MeOH-based $Pb(NO_3)_2$ solution – providing the Pb^{2+} cations, (ii) pure MeOH solvent to remove the excess of unbound cations, (iii) MeOH-based Na_2S solution – providing the S^{2-} anions, and (iv) pure MeOH solvent to remove the excess of unbound anions. Steps (i) through (iv) are termed as one SILAR cycle, and denoted here as Cn, $n \geq 1$. Analogously, we define here *half cycle* as the same routine terminated after step (ii) (a scheme of SILAR method is given in chapter 2, sample preparation section). Note that half-cycle samples (Cn.5, $n \geq 1$) are characterized by a Pb-rich surface while samples grown with a completed cycle (Cn, $n \geq 1$) are S-rich. To avoid QD photo-oxidation, sample preparation and measurements were realized under N_2 conditions.

4.3 Results and Discussions

4.3.1 TEM characterization: QD growth mechanism.

Before reporting how QD stoichiometry affects electron transfer rate and efficiency, we characterize the SILAR-grown nanocrystal morphologies. The characteristic red-shift of the absorption threshold of SILAR-based QD-sensitized oxides *vs.* the number of SILAR cycles[24, 25] is a manifestation of a size-dependent confinement effect (see figure 2.5 in chapter 2). In order to accurately correlate QD structure and ET dynamics we performed transmission electron microscopy (TEM) on our samples; representative images for PbS QDs on a SnO_2 mesoporous support for samples C1, C3 and C6 are shown in figure 4.1(A-C). The TEM images reveal that QDs are uniformly distributed on the oxide surfaces, and do not show preferential nucleation on particular SnO_2 facets (larger area and higher resolution images are provided in figure 4.6 in Appendix). From TEM image statistical analysis, a saturation of PbS QD base diameter (*2r*) is apparent for samples beyond 3 SILAR cycles (see figure

4.1(D)). The saturation in QD base diameter is followed by a significant change in QD height (as resolved by monitoring QD aspect ratios (*h/r*), as a function of the number of SILAR cycles, see figure 4.1(E)). A similar qualitative change in aspect ratios was reported before for SILAR-based CdSe QDs onto TiO_2 and ZnO surfaces.[12, 37] In parallel with the saturation of the QD base diameter (from C3 and onwards), we observe the emergence of QD aggregates (PbS bulky phases, see TEM images in figure 4.6 (D) and (F) in the Appendix 4.5.1). The emergence of polycrystalline PbS phases after the QDs saturate in base diameter is consistent with the appearance of an ultrafast component in the ET dynamics for samples beyond C4, due to direct photogeneration and recombination of free carriers within the bulky QD clusters. Similar behavior has previously been observed for samples sensitized with colloidal QDs.[14, 33, 34] Furthermore, the emergence of an ultrafast component on the OPTP dynamics is accompanied in our samples by a decrease in the ET efficiency (as apparent from the reduced THz response at long times – see figure 4.7 (A) in the Appendix 4.5.2), indicating that the PbS bulky patches are strong photon absorbers but are not substantially contributing to the overall photocurrent in the samples. This scenario agrees well with previous observations that QDSSCs typically exhibit an increase in photocurrent followed by a decrease, as a function of the number of SILAR cycles.[24, 25] The correlation between nanostructure and ET dynamics stresses the importance of preventing the transition from isolated QD growth to polycrystalline thin film growth in sensitized architectures. For an optimum device performance, high surface densities of isolated QDs without aggregate formation are required.

Heteroepitaxial QD/oxide growth by different solution-processing methods has recently been discussed in a review;[15] concerning the SILAR method, to the best of our knowledge, only one report resolved the epitaxial growth of crystalline PbS QDs nucleated onto anatase TiO_2 surfaces by TEM.[25] As shown in figure 4.1(F), for our samples we have also been able to resolve crystalline PbS QDs epitaxially grown onto rutile SnO_2 surfaces. Our deposition recipe results in [111] faceted PbS dots with near-unity aspect ratio. These observations, together with the characteristic change in QD aspect ratio as a function of deposited material, indicate that epitaxial growth (triggered by QD/oxide lattice mismatch) most likely governs the nucleation of nanocrystals in our SILAR based samples. Note that in hetero-epitaxial Volmer-Weber growth mode an increasing aspect ratio as a function of the amount of deposited material has been predicted theoretically[38] and resolved experimentally[39]. Based on this analogy, we propose a simple model for the growth kinetics as sketched in figure 4.1(G). Our semi-empirical model considers spherical cap-shaped QDs assuming that SILAR deposition steps change the height of the QDs linearly and that the QD growth is self-limiting when *h*/*r* aspect ratios approach unity (*half-sphere* shaped QDs). Taking only the empirically measured saturated QD diameter radius as input ($R = r \sim 2.9$ nm for C6), such a simple growth model is able to describe remarkably well the QD diameters (*2r*) and aspect ratios (*r/h*) obtained from our statistical treatment on TEM characterization (see dashed lines in figures 4.1 (D-E)).

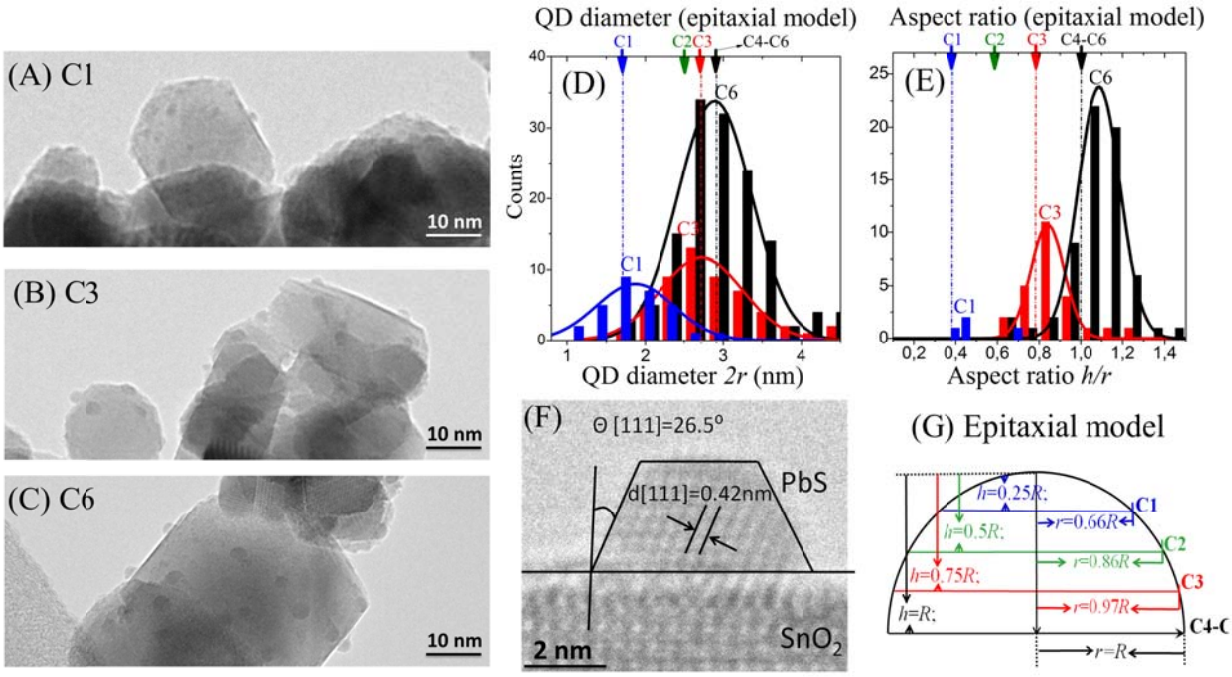

Figure 4.1 (A-C) characteristic TEM images for SnO_2 samples sensitized with 1, 3, and 6 SILAR cycles (C1, C3 and C6, respectively); (D) histograms of QD base diameters (*2r*) as a function of SILAR cycles (vertical bars) and results of the semi-empirical nucleation model (dashed vertical lines) shown in panel (G); (E) histograms of QD aspect ratios (vertical bars) and comparison with the semi-empirical nucleation model (dashed vertical lines) shown in panel (G). (F) [111] faceted epitaxial PbS QD resolved by TEM at the SnO_2 edge; (G) proposed nucleation mechanism ("epitaxial model") for *spherical cap-shaped* QDs sensitizing a mesoporous oxide by SILAR method (*h* and *r* denotes QD height and base radius, *R* refers to the saturated QD radius when *h/r* aspect ratio is unity).

4.3.2 Dependence of ET rates on QD size and stoichiometry.

Once the QD size dependence on the number of SILAR cycles has been resolved and modeled, we analyze the ET rates. Figure 4.2(A) shows the normalized pump-induced real part of the complex THz photoconductivity ($Re(\sigma)$) for samples C1, C2 and C3. The rise of the signal after photoexcitation is a direct manifestation of ET from the QD donor to the oxide acceptor, as the conductivity of electrons (and holes) in the QD is purely imaginary.[40] As shown in the plot, the observed ET dynamics in all cases are identical within the signal to noise ratio of our measurements, indicating that electron transfer rates from the sensitizer to the oxide are independent of the QD size. On the other hand, as shown in the inset of figure 4.2(A), the back-transfer, resulting in recombination of electrons and holes, does slow down with the number of SILAR cycles. A simple model using a single-stretched-exponential ingrowth and decay reveals rates of ET from QD to oxide and back electron transfer (BET) from oxide to QD (K_{ET} and K_{BET}, respectively) of $1/K_{ET}$(C1-3) =6.5 ±1.5 ps (with stretched coefficients of 0.68±0.05) and $1/K_{BET}$(C1) =2650±140 ps, $1/K_{BET}$(C2) =4620±160 ps, and $1/K_{BET}$(C3-C3.5) =8100±500 ps. Interestingly, as shown in figure 4.2(B), the ET dynamics are independent not

only of SILAR cycles (or sizes of QDs), but also of QD stoichiometry as illustrated by the OPTP traces for samples C3 and C3.5 (characterized by sulfur- and lead-rich QD surfaces, respectively). The fact that back ET rates are independent on QD stoichiometry suggests that the QD/oxide energetics and coupling strength are independent of QD surface doping. The invariance of ET dynamics with QD size and stoichiometry can be rationalized by Fermi level pinning[41, 42] at the PbS/SnO_2 interface, so that the energy difference between QD LUMO and oxide CB (given by ΔG and ΔG' in figure 4.3 (B)) is not modulated by QD size or surface doping (ΔG and $\Delta G'$ are equal and independent of nanocrystal dimensions). This is generally different from *ex situ* QD-sensitized oxides systems, where ET slows down with increasing QD size as a consequence of reduced ΔG (see figure 4.3(B)).[34, 43] Similarly, as theoretically predicted[44] and experimentally reported[27, 28, 45, 46], changes in the SILAR QD S/Pb ratio (QD stoichiometry) will affect the QD Fermi level, yet apparently do not affect ET rates. While the variation in both QD size and stoichiometry will affect QD energy levels, the energy difference between QD LUMO and oxide CB is not modulated by QD size or doping at the QD/air interface.

Back ET (BET) kinetics have been reported[47, 48] in dye sensitized systems to be determined by not only the energetics, but also by diffusion/hopping of charges within the oxide films, which can also be rate limiting. Even in the simple case that the overall recombination is determined by the interfacial BET, and assuming Marcus theory applies, BET rates will vary with driving force in a way depending on whether it occurs on the normal or inverted regions (which will depend on the system reorganization energy). Also BET can be a function of oxide/QD coupling strength which in our system is QD size dependent[21]. Although an accurate description of the BET process observed here is out of the scope of the present work, the observed decrease of K_{BET} with SILAR-cycle-number (see inset figure 4.2(A)) is consistent with an upward-shifting HOMO level (the HOMO level is not pinned). The experimentally resolved decrease of K_{BET} with SILAR-cycle-number (see inset figure 4.2(A)) is then a consequence of an increasingly smaller driving force for back-ET and increasingly smaller donor/acceptor coupling with increasing QD size.

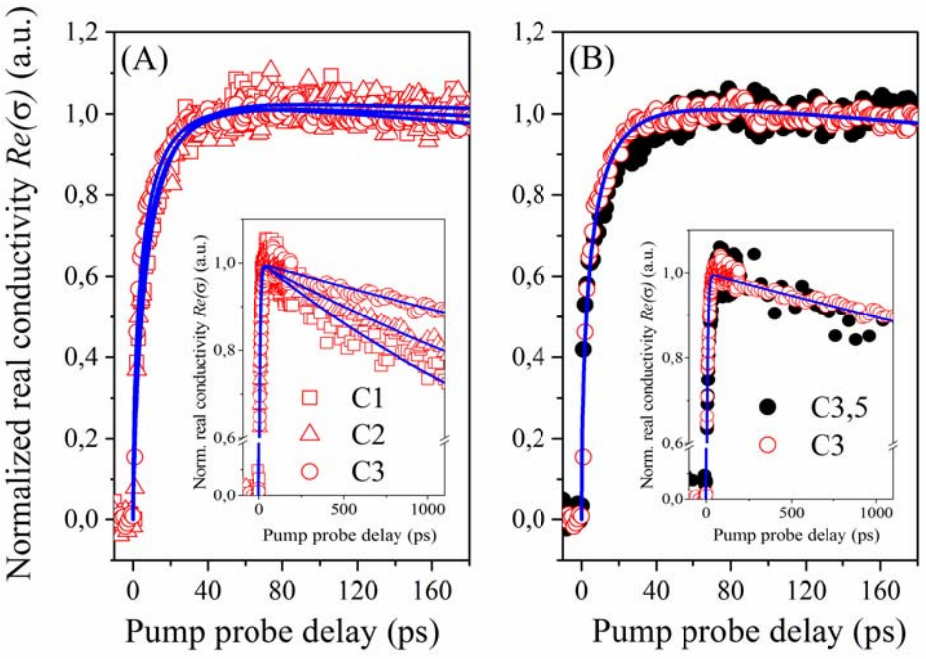

Figure 4.2 (A) Normalized OPTP response for PbS QDs sensitizing SnO_2 as a function of the number of SILAR cycles (C*n*, with *n* = 1-3); in the inset are shown the dynamics up to 1.1 ns; blue lines are best fits to the data as described in the text. (B) Normalized OPTP response for PbS QDs sensitizing SnO_2 by SILAR as a function of surface stoichiometry (by comparing samples with C3 and C3.5 SILAR cycles – Sulfur- and Lead-rich, respectively); the inset shows the dynamics up to 1.1 ns; blue lines are best fits to the data.

4.3.3 Dependence of ET efficiency on QD size and stoichiometry

Theoretically[44], nanocrystals with a perfect 1:1 stoichiometry ratio are expected to be intrinsic and therefore defect free. In practice, synthesized nanocrystals are typically non-stoichiometric[29, 49, 50] and characterized by the presence of surface states acting as donors or acceptors.[44] The passivation of those states for SILAR-based QDs requires a post-growth passivation treatment, commonly accomplished by introducing an organic or inorganic capping shell onto the QDs.[6, 25, 51] Alternatively, atomic passivation has been successfully exploited as a pathway for reversibly[31, 52, 53] tailoring the optoelectronic properties in colloidal QD *solids*, through doping[27-29, 45, 46] and passivation[31, 52, 53]. The effect of stoichiometry on QD-sensitized oxide systems has not been addressed to date. In figure 4.3 (A), we plot the ET dynamics for PbS QDs nucleated onto SnO_2 nanoparticles by C3 and C3.5 SILAR cycles (probed on the same sample spot for a given oxide substrate), corresponding to S- and Pb-rich QD surfaces, respectively. From the obtained plateau amplitude of the ET traces it is evident that QDs terminated by Pb surfaces allow more efficient ET from the QD to the oxide than those terminated by S (assuming that half cycle treatment by itself is not sufficient for the nucleation of new dots). This finding is consistent with the removal of PbS QD surface acceptors acting as traps by Pb capping, and is in perfect agreement with theory and experiments reporting the generation of Pb related surface

donors on QDs with S/Pb<1 ratios.[27, 28, 44] As summarized in figure 4.3(B) the observed enhancement of ET efficiency for lead-rich (or Sulfur-deficient) QD surfaces is a manifestation of a favorable kinetic competition between QD/oxide electron transfer (K_{ET}) and undesired trapping at the QD surface (K_{Tr}). Analogously, a sulfur-rich (lead-deficient) QD surface will be prone to trapping of photo-generated electrons in surface acceptor traps, lowering the ET efficiency.

The half cycle-cation passivation effect reported here for the PbS/SnO_2 system is a general phenomenon, as we observed identical qualitative effects on half-cycle terminated samples consisting on PbS/TiO_2, PbS/ZnO and PbSe/SnO_2 (see figure 4.8 in the Appendix 4.5.3).

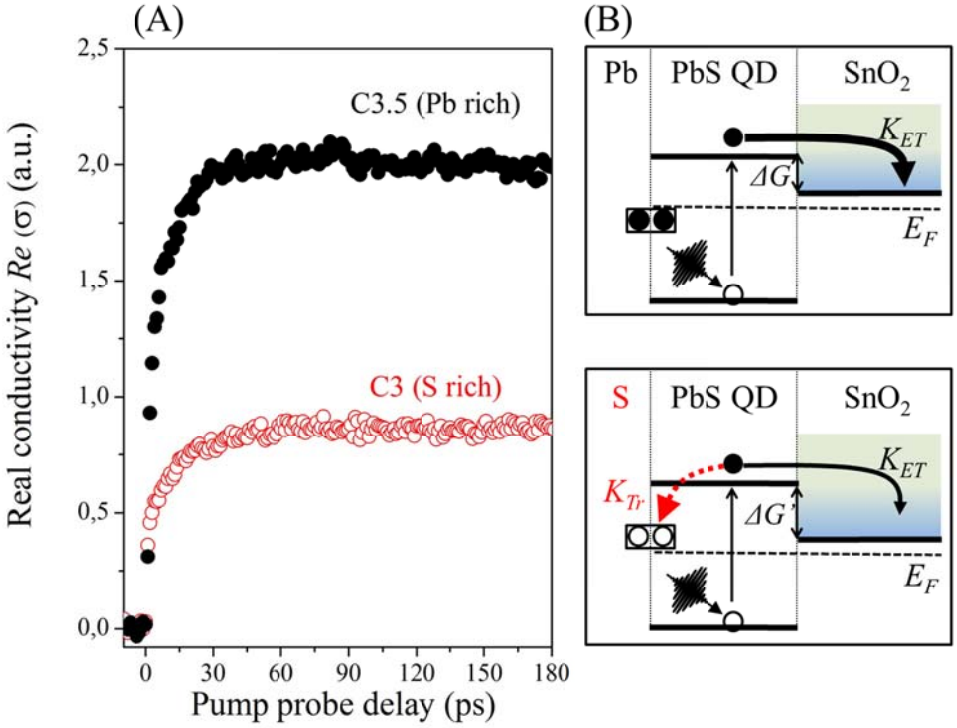

Figure 4.3 Stoichiometry effect on ET dynamics. (A) Characteristic optical pump-THz probe response for PbS QDs sensitizing SnO_2 by SILAR as a function of surface stoichiometry (comparing samples with C3 and C3.5 SILAR cycles). (B) Sketch illustrating system energetics as a function of PbS QD surface stoichiometry (ΔG represents donor-acceptor ET driving force); S-rich QD surfaces are populated with acceptors (p-type) allowing electron trapping (K_{Tr}) at the nanocrystal surface; Pb-rich surfaces are populated by donors (n-type), making electron trapping at the surface not feasible and hence maximizing the probability of ET to the oxide (K_{ET}).

In figure 4.4(A), we present the maximum of the observed pump-induced real photoconductivity ($Re(\sigma)$) at ~100 ps after the excitation pulse) as a function of the number of SILAR cycles for PbS nanocrystals sensitizing SnO_2. As discussed for C3 and C3.5 SnO_2/PbS samples (figure 4.3(A)), the passivation effect by an additional half cycle results in an ET efficiency enhancement in all cases

(from C1.5/C1 to C6.5/C6). For atomically Pb-passivated samples we resolve a monotonous increase in the monitored photoconductivity as a function of SILAR cycles within the range defined by C1.5 and C4.5. For samples treated beyond C4.5 SILAR cycles (C5.5 and C6.5 SILAR cycles), a decay in the overall measured photoconductivity is observed. The decay is consistent with the formation of QD aggregates beyond C4 cycles as discussed previously (bulky PbS phases acting as strong photon absorbers but poor donors). The observed improvement in the absolute amplitude of the photoconductivity between C1.5 and C4.5 SILAR cycles can be correlated with a QD size dependent effect, but can also result from an increasing population of QDs per unit area. In order to remove the potential effect of an increasing QD population we define here a passivation efficiency term defined as: $PE = \{Re(\sigma)_{Cn.5} - Re(\sigma)_{Cn}) / Re(\sigma)_{Cn}\}$,

with $n \geq 1$, where $Re(\sigma)_{Cn.5}$ and $Re(\sigma)_{Cn}$ stand for the plateau real conductivity of samples with C*n*.5 and C*n* SILAR cycles, respectively. In this respect, *PE* simply represents the Pb-passivation effect without considering changes in QD surface densities per unit area of the oxide. As derived in the Appendix 4.5.4, the passivation efficiency can be rewritten as $PE = \{K_{Tr} / K_{ET}\}$, in which K_{Tr} represents the rate of electron trapping at QD surfaces and K_{ET} is the rate of ET from donor to acceptor. As a consequence, the defined *PE* term physically represents the kinetic competition between undesired trapping at the QD surface (K_{Tr}) and QD/oxide electron transfer (K_{ET}), as illustrated in figure 4.3(B). As discussed above (see figure 4.2(A)), K_{ET} is a constant regardless of QD size (or, equivalently, regardless of the number of SILAR cycles, *Cn*). On the other hand, trapping rates are linearly dependent on defect density in bulk semiconductors.[54, 55] In this respect, for our system (where $K_{ET}(Cn) = constant$) we have that $PE \propto K_{Tr}(Cn) \propto N_{acceptors} \propto QD_{surface\ area}$. In figure 4.4(B) the dependence of *PE* vs $QD_{surface\ area}$ is plotted, the latter being estimated from our epitaxial model and TEM characterization, see figures 4.1(D, E and G). A linear correlation is resolved between C1 and C4 SILAR cycles, in agreement with the notion that the QD trapping rate is linearly correlated with QD area. Note that the saturation of PE at 300% versus QD surface area observed for samples beyond C4 is a manifestation of the saturation in the QD size as a function of deposition steps (in perfect agreement with TEM characterization).

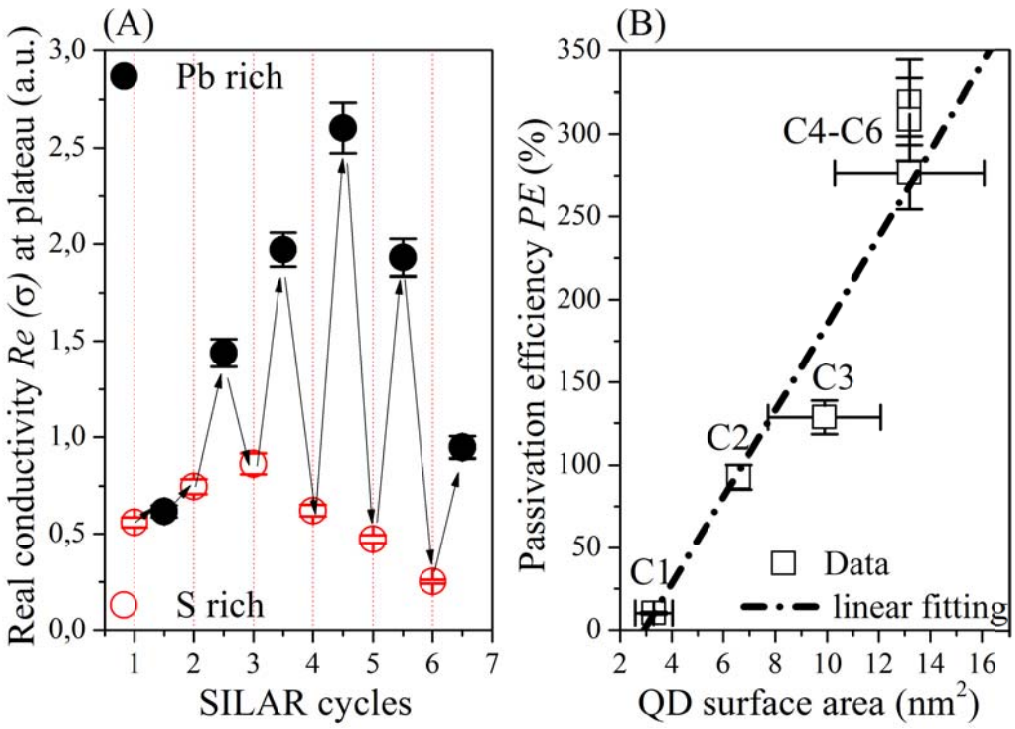

Figure 4.4 (A) Monitored real conductivity at the plateau (when ET has ended) as a function of SILAR deposition steps. Samples made of complete- and half- cycles are characterized by S- and Pb-rich QD surfaces. (B) Atomic passivation efficiency (*PE*) *vs* QD surface area (estimated from TEM statistics and the epitaxial growth model as discussed in the paper). The uncertainty in *PE* is obtained from 5-7 measurements on a given sample. The uncertainty in the QD surface area is inferred from the distribution in QD base diameter (FWHM) as a function of SILAR cycles from TEM analysis.

4.3.4 Implications of our results for QDSSC design

The maximum theoretical efficiency in excitonic solar cells is given by the Shockley-Queisser limit, provided that efficient ET processes from a *bandgap* optimized sensitizer to the selective contacts are made at no energy cost[19] (i.e. Ohmic contacts are established between the sensitizer HOMO-LUMO levels and the electron-hole electrodes respectively). In this contribution we show that stoichiometry control on SILAR-based QDs can be employed as a simple and efficient passivation scheme in order to remove recombination pathways in the QD sensitizers (an essential requirement for devices with high photocurrents). Provided that full passivation in the QDs is achieved by half SILAR cycle treatments (*e.g.* atomic passivation will not be compromised by surface packing as may be the case for molecules), the only electron relaxation pathway in the QDs will be radiative, making the kinetic competition with ET to the oxide favorable for the latter. On the other hand, we have resolved saturation in QD size during growth, followed by the appearance of polycrystalline phases as a function of SILAR cycles and suggested Fermi-level pinning at the QD/oxide interface. All these aspects represent constraints towards high efficiency devices. Saturation in QD size nucleation for a given system (most likely correlated with strain relaxation on lattice mismatched QD and oxide

phases) could prevent achieving optimum *bandgaps* matching the solar spectrum (~1.4 eV for maximum efficiency[19]). Once QD size saturation is reached after a certain number of cycles, the appearance of *bulky* polycrystalline phases should be prevented in devices (as these are strong photon absorbers and recombination centers, without substantially contributing to the photocurrent in the photovoltaic device). Note that preventing the formation of QD aggregates could dictate a minimum thickness to achieve full sunlight absorption for a given QD/oxide system (*e.g.* if QD oxide coverage depends on the number of deposited SILAR cycles). Finally, the suggested pinning at QD/oxide surfaces could prevent fine tuning of donor-acceptor energetics, and then trying to achieve Ohmic contacts between QD and oxide will be compromised (potentially reducing solar cell output voltage[19]).

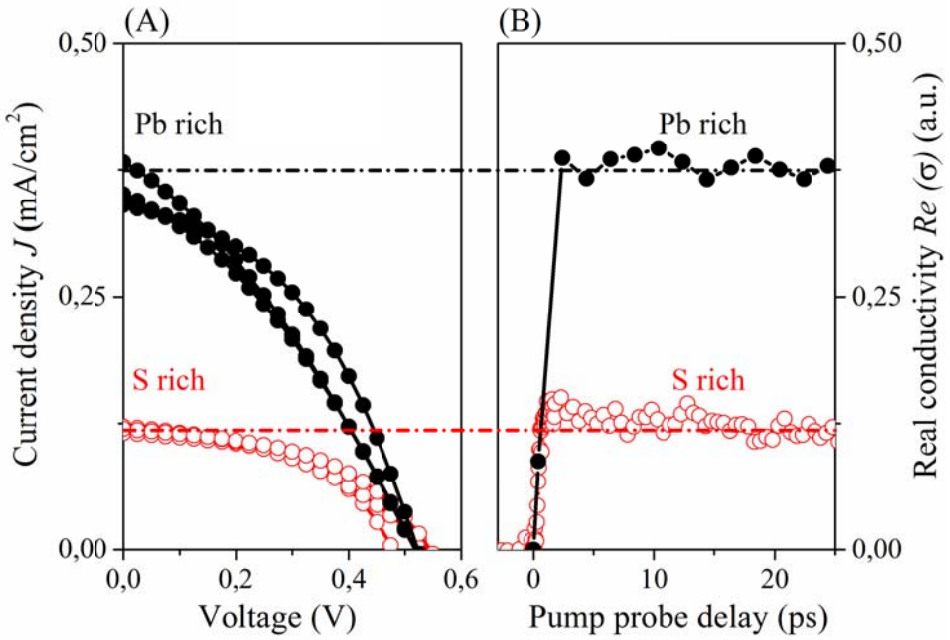

Figure 4.5 (A) Current-voltage characteristics of QDSSC devices (ITO/PbS@TiO_2/OMeTAD/Au) with QDs terminated with a lead- or sulfur- rich surface; (B) Characteristic optical pump-THz probe response for PbS QDs sensitizing TiO_2 by SILAR as a function of surface stoichiometry (comparing samples with C4 and C4.5 SILAR cycles).

In order to check whether metallic surfaces will constrain the voltage in devices and also whether the monitored passivation efficiency can be exploited in complete devices (*e.g.* if such an effect is unaltered by the presence of a hole conductor), we characterized 3 sets of QDSSCs based on 4 and 4.5 PbS QD SILAR cycles onto TiO_2 electrodes (C4 and C4.5 samples, respectively). The ITO/PbS@TiO_2 electrodes where sandwiched together with spiro-OMeTAD/Au contacts (further details are given in the SI) and solar cell current-voltage characteristics were recorded in a homemade solar simulator. As shown in figure 4.5(A), for all the devices tested we obtained a ~210% improvement in the photocurrent for the samples terminated with half a cycle (Pb-rich QD surfaces), revealing a

quantitative correlation between the observed *PE* improvement by OPTP measurements (see figure 4.5 (B)) and the monitored short circuit current (J_{SC}) in complete solar cell devices. Note that the kinetics (including recombination kinetics) may differ substantially under transient (THz) and steady state (device working) conditions (under illumination). In particular, under steady-state illumination, trap filling can alter transfer rates. On the other hand, we observe that the open circuit voltages (V_{OC}) for the two devices containing, respectively, QDs with Pb- or S-rich surfaces are indistinguishable within the range of values observed for the different samples. For our cells, the similar values for V_{OC}*'s* (within the sample-to-sample variation) indicates in simple terms, that the maximum quasi Fermi level splitting under illumination within the PbS QD absorber (which could be limited by the reported pinning) is preserved for cationic and anionic rich QD surfaces. Overall, the reported results indicate that atomic passivation can potentially be well-suited for QDSSCs.

4.4 Summary

In summary, we have correlated the structure and stoichiometry of QDs grown on SnO_2 films with the electron transfer rates and efficiency. Transmission electron microscopy reveals saturation in the QD base diameter, followed by an increase in nanocrystal height as a function of the number of SILAR cycles. This shape transition, together with the observation of the presence of hetero-epitaxial nucleated dots suggest that Volmer-Weber growth (mediated by lattice mismatch between QD and oxide materials), is the underlying growth mechanism for the analyzed SILAR-based QD sensitized system. While ET rates from the QD to the oxide are found to be insensitive to QD size and stoichiometry (attributed to Fermi level pining at the QD/oxide interface), the ET efficiency is found to be highly dependent on both aspects. In fact, half-cycle, n-type QD surfaces (cation-rich) exhibit a better passivation of the QD, which in turn favors photo-induced ET processes from the QD to the oxide acceptor. The cationic passivation effect is found to be QD-size dependent, being more prominent as QD area increases and correlating with density of QD surface acceptors. Finally, OPTP measurements are correlated with device photocurrents, showing that exploiting QD stoichiometry for nanocrystal passivation could be an efficient strategy for solar cell design.

4.5 Appendix

4.5.1 Transmission electron microscopy (TEM) study on PbS grown dynamics at SnO_2 surfaces

Transmission electron microscopy (TEM) images were obtained with a JEOL JEM-2010 microscope. Samples for TEM analysis were prepared by mechanically removing the QD-sensitized films from the substrate. The resulting powders were diluted in ethanol and drop casted onto carbon-coated copper grids. Figure 4.6 shows large area and high magnification TEM images for SILAR-based QDs sensitizing SnO_2 matrices for 1 to 6 cycles. Figure 4.6 (D) and (F) reveal the presence of QD aggregates (bulk polycrystalline phases). These aggregates are identified by noticing [111] facets separated by 0.42 nm, characteristic for PbS (see figure 4.6 (D)).

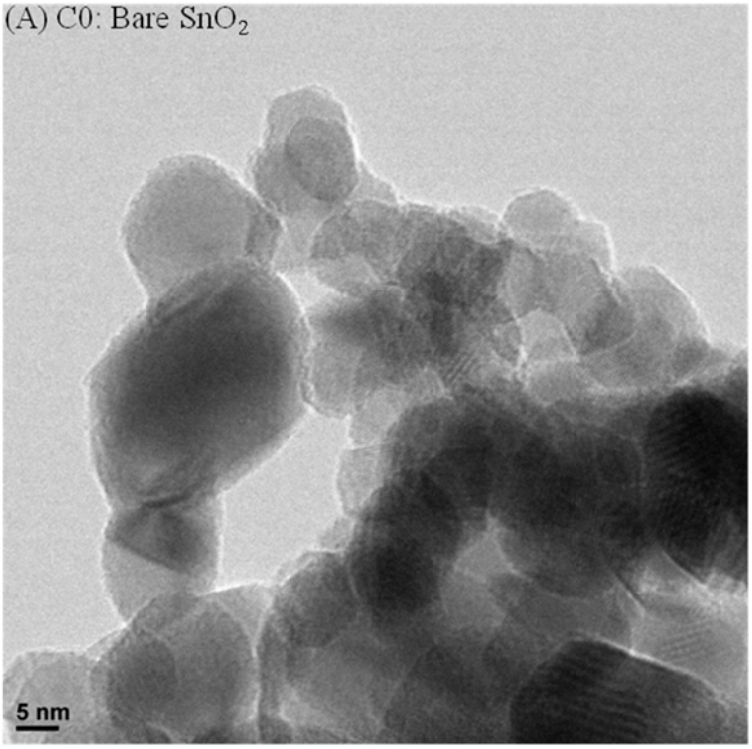

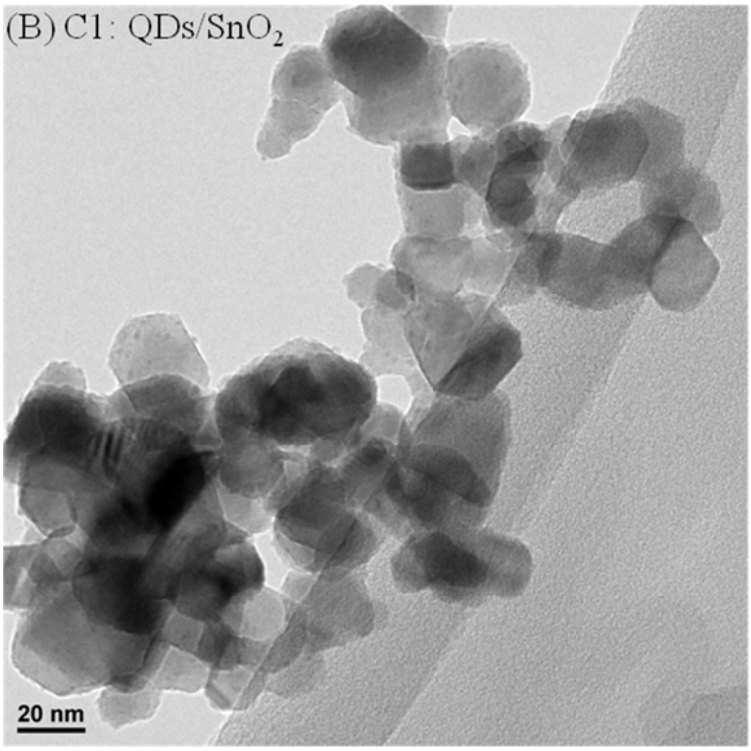
(B) C1: QDs/SnO2
20 nm

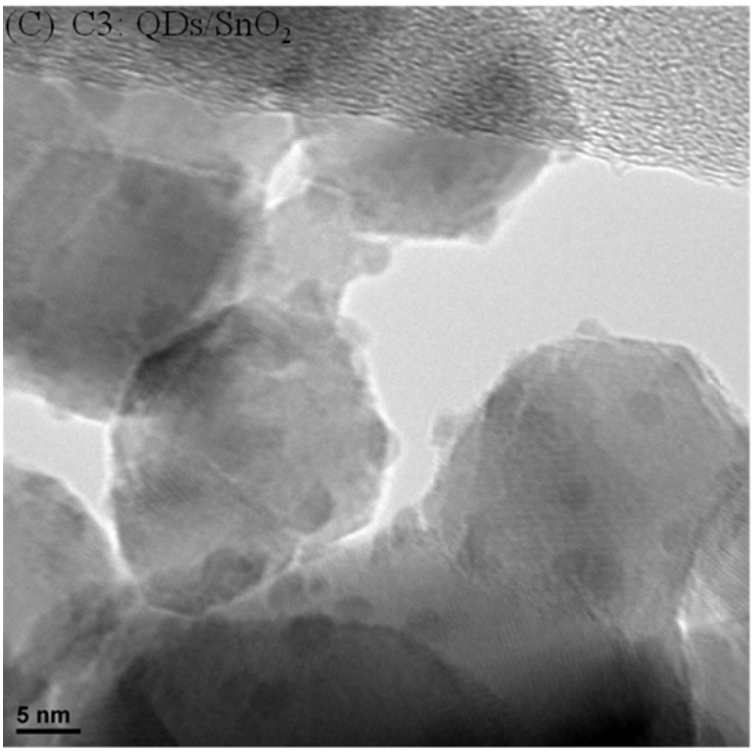
(C) C3: QDs/SnO2
5 nm

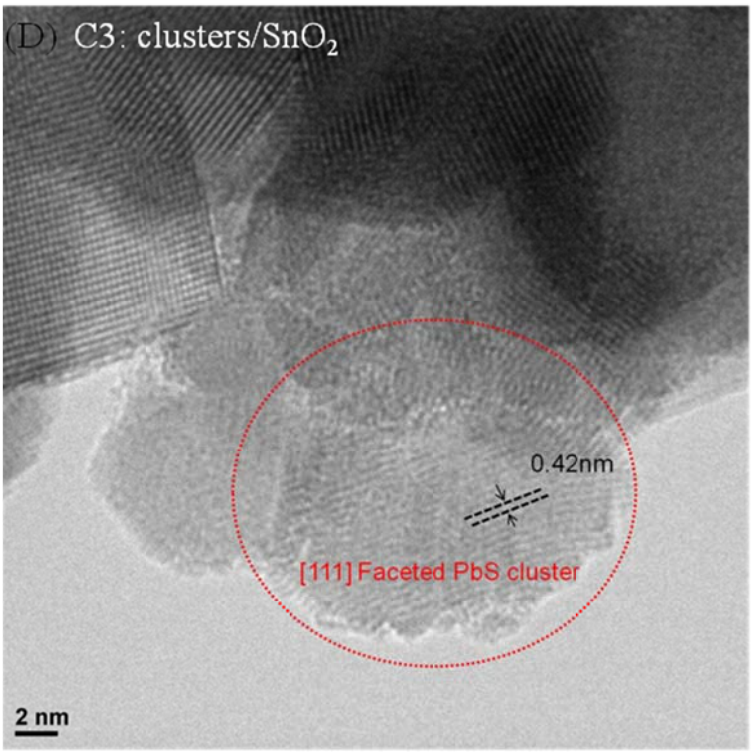
(D) C3: clusters/SnO2
0.42nm
[111] Faceted PbS cluster
2 nm

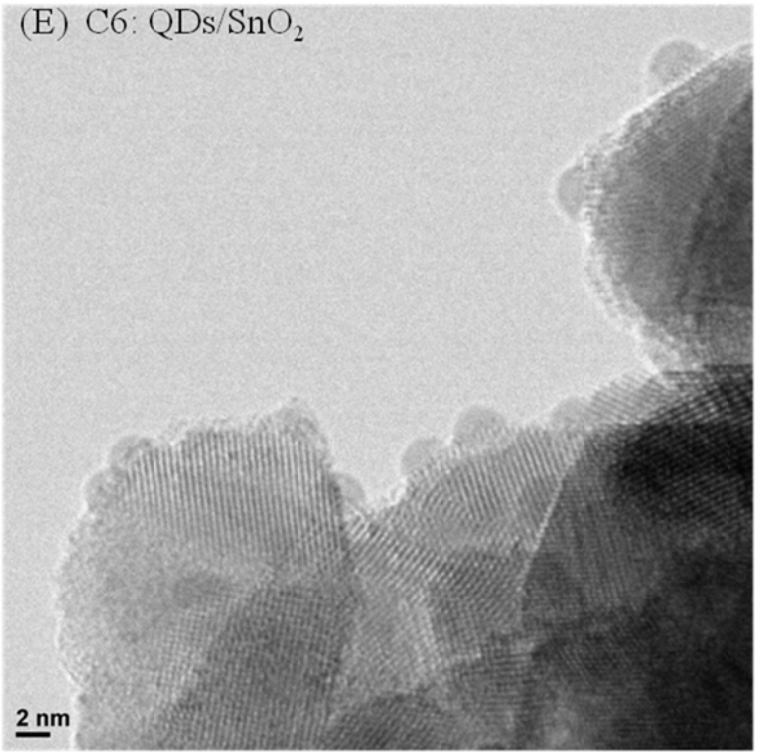
(E) C6: QDs/SnO2
2 nm

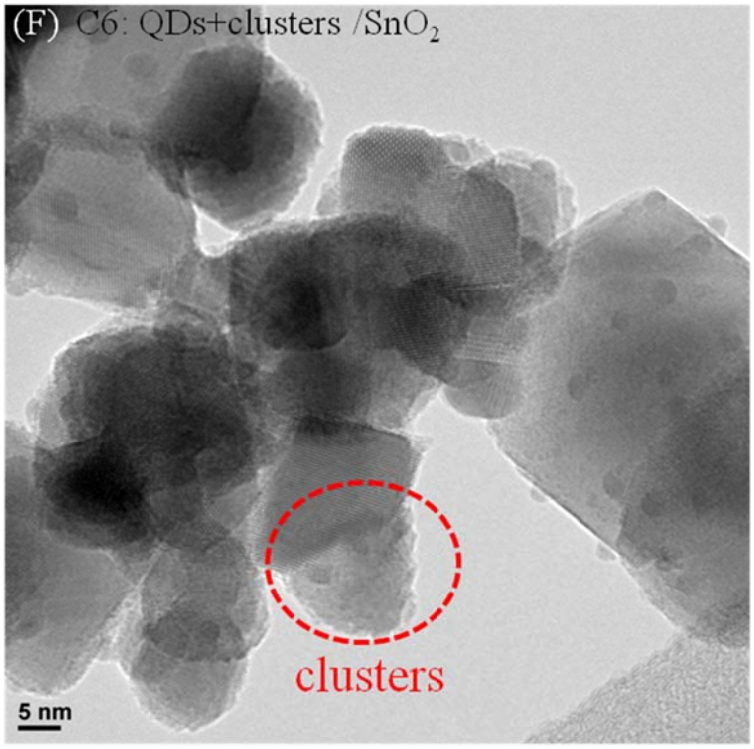

Figure 4.6 Nucleation and growth processes of SILAR-based PbS QDs on SnO_2 resolved by TEM as a function of deposited cycles Cn (n = 0, 1, 3 and 6). Figures (D) and (F) highlight the presence of PbS QD aggregates.

4.5.2 Dependence of OPTP traces as a function of SILAR cycles

Figure 4.7 (A) shows the OPTP traces for SnO_2 samples sensitized with PbS QDs with different number of SILAR cycles (1 to 6). The ET efficiency (correlated with the plateau value of the real conductivity in the plot) initially increases with the number of cycles and then drops after the third cycle. Figure 4.7 (B) shows the normalized ET dynamics. From C4 onward, when the ET efficiency drops, an ultrafast component appears in the dynamics within the first few ps-seconds after photo-excitation. This feature is consistent with the resolution of an overlapped signal due to carrier dynamics in QD cluster phases.[56-58]

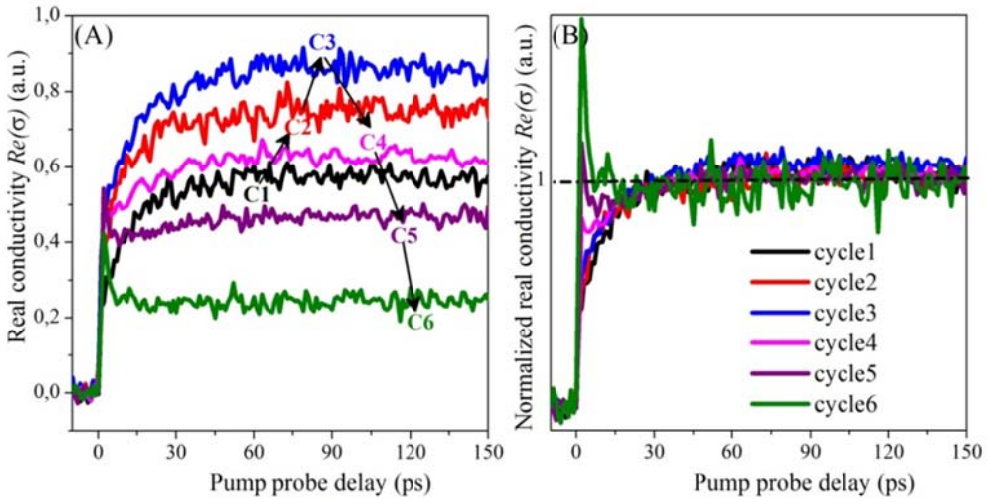

Figure 4.7 (A) Bare OPTP dynamics as a function of the number of SILAR cycles up to 150 ps. (B) Idem but normalizing the OPTP traces to the plateau signals.

4.5.3 Lead cation passivation effect for different combinations of QDs and oxides

In order to check whether the monitored lead cation passivation effect is general for other systems, the ET dynamics for (1) PbS QDs on ZnO and TiO_2 (different oxides), and (2) PbSe QDs on SnO_2 (different QDs), were measured. Qualitatively all Pb-ended samples (half cycle) showed a boost on photoconductivity, as shown in figure 4.8.

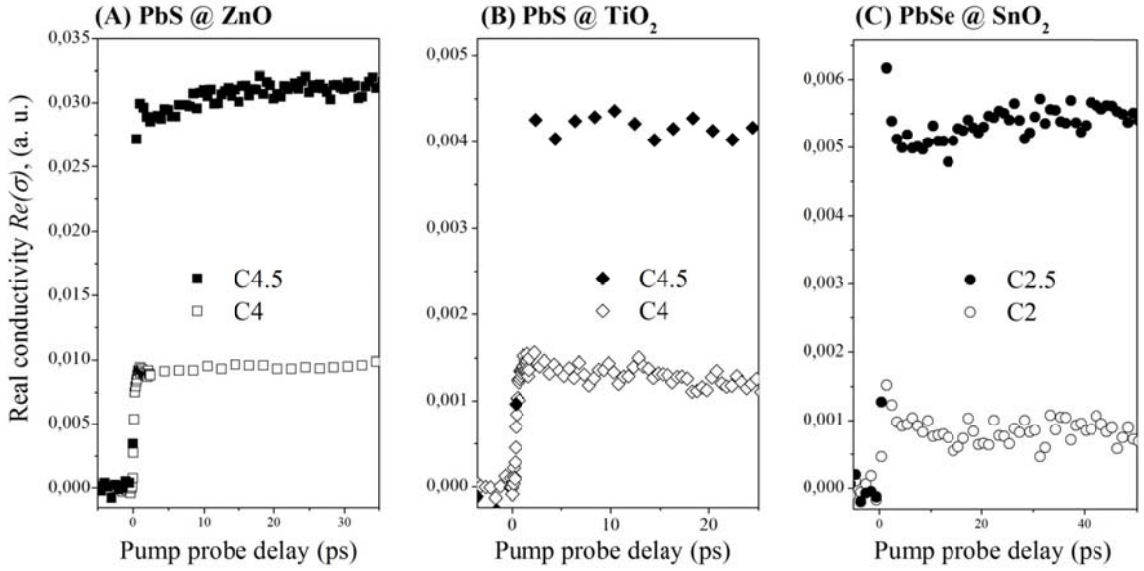

Figure 4.8 Cation passivation effect for different combinations of QDs and oxides; (A) PbS@ZnO; (B) PbS@TiO_2 and (C) PbSe at SnO_2.

4.5.4 Definition of passivation efficiency PE

In order to remove the potential effect of an increasing QD population with the number of deposition cycles, we define here a passivation efficiency term as: $PE = \{Re(\sigma)_{Cn.5} - Re(\sigma)_{Cn}) / Re(\sigma)_{Cn}\}$, with $n \geq 1$. In this respect, *PE* simply represents the absolute Pb passivation effect without considering changes in QD surface densities per unit area. Given that the time resolved photoconductivity can be written as $Re(\sigma) = \mu * N_{ET} * e$, where μ is the electron mobility in the oxide CB, N_{ET} is the number of electrons transferred to the oxide and *e* the elementary charge, we can rewrite *PE* as: $PE = \{N_{Tr}(Cn)/ N_{ET}(Cn)\}$, with $N_{Tr}(Cn) = N_{ET}(Cn.5) - N_{ET}(Cn)$, where $N_{Tr}(Cn)$ is the number of electrons being trapped in the QD surface before passivation with lead. As N_{Tr} and N_{ET} can be defined as $N_{Tr} = N_{tot} * (K_{Tr} / K_{Tr} + K_{ET})$ and $N_{ET} = N_{tot} * (K_{ET} / K_{Tr} + K_{ET})$ respectively (where N_{tot} is the total population of photogenerated excitons), then we can write *PE* further as: $PE = \{K_{Tr} / K_{ET}\}(Cn)$, with $n \geq 1$. Therefore, physically, the defined *PE* term is directly reflecting the kinetic competition between QD/oxide electron transfer (K_{ET}) and undesired trapping (K_{Tr}).

References

1. Wang, J.; Mora-Sero, I.; Pan, Z. X.; Zhao, K.; Zhang, H.; Feng, Y. Y.; Yang, G.; Zhong, X. H.; Bisquert, J. *J Am Chem Soc* **2013,** 135, (42), 15913-15922.

2. Pan, Z. X.; Mora-Sero, I.; Shen, Q.; Zhang, H.; Li, Y.; Zhao, K.; Wang, J.; Zhong, X. H.; Bisquert, J. *J Am Chem Soc* **2014,** 136, (25), 9203-9210.

3. Zhang, J. B.; Gao, J. B.; Church, C. P.; Miller, E. M.; Luther, J. M.; Klimov, V. I.; Beard, M. C. *Nano Lett* **2014,** 14, (10), 6010-6015.

4. Zhao, K.; Pan, Z.; Mora-Seró, I.; Cánovas, E.; Wang, H.; Song, Y.; Gong, X.; Wang, J.; Bonn, M.; Bisquert, J.; Zhong, X. *J Am Chem Soc* **2015**.

5. Lee, J. W.; Son, D. Y.; Ahn, T. K.; Shin, H. W.; Kim, I. Y.; Hwang, S. J.; Ko, M. J.; Sul, S.; Han, H.; Park, N. G. *Sci Rep-Uk* **2013,** 3.

6. Santra, P. K.; Kamat, P. V. *J Am Chem Soc* **2012,** 134, (5), 2508-2511.

7. Ahn, H. J.; Kim, M. J.; Kim, K.; Kwak, M. J.; Jang, J. H. *Small* **2014,** 10, (12), 2325-2330.

8. Lee, H.; Wang, M. K.; Chen, P.; Gamelin, D. R.; Zakeeruddin, S. M.; Gratzel, M.; Nazeeruddin, M. K. *Nano Lett* **2009,** 9, (12), 4221-4227.

9. Salant, A.; Shalom, M.; Hod, I.; Faust, A.; Zaban, A.; Banin, U. *Acs Nano* **2010,** 4, (10), 5962-5968.

10. Blackburn, J. L.; Selmarten, D. C.; Nozik, A. J. *J Phys Chem B* **2003,** 107, (51), 14154-14157.

11. Piris, J.; Ferguson, A. J.; Blackburn, J. L.; Norman, A. G.; Rumbles, G.; Selmarten, D. C.; Kopidakis, N. *J Phys Chem C* **2008,** 112, (20), 7742-7749.

12. Guijarro, N.; Lana-Villarreal, T.; Shen, Q.; Toyoda, T.; Gomez, R. *J Phys Chem C* **2010,** 114, (50), 21928-21937.

13. Santra, P. K.; Palmstrom, A. F.; Tanskanen, J. T.; Yang, N.; Bent, S. F. *J Phys Chem C* **2015,** 119, (6), 2996-3005.

14. Wang, H.; McNellis, E. R.; Kinge, S.; Bonn, M.; Canovas, E. *Nano Lett* **2013,** 13, (11), 5311-5315.

15. Selinsky, R. S.; Ding, Q.; Faber, M. S.; Wright, J. C.; Jin, S. *Chem Soc Rev* **2013,** 42, (7), 2963-2985.

16. Acharya, K. P.; Khon, E.; O'Conner, T.; Nemitz, I.; Klinkova, A.; Khnayzer, R. S.; Anzenbacher, P.; Zamkov, M. *Acs Nano* **2011,** 5, (6), 4953-4964.

17. Selinsky, R. S.; Shin, S.; Lukowski, M. A.; Jin, S. *J Phys Chem Lett* **2012,** 3, (12), 1649-1656.

18. Acharya, K. P.; Hewa-Kasakarage, N. N.; Alabi, T. R.; Nemitz, I.; Khon, E.; Ullrich, B.; Anzenbacher, P.; Zamkov, M. *J Phys Chem C* **2010,** 114, (29), 12496-12504.

19. Giebink, N. C.; Wiederrecht, G. P.; Wasielewski, M. R.; Forrest, S. R. *Phys Rev B* **2011,** 83, (19).

20. Yang, Y.; Rodriguez-Cordoba, W.; Xiang, X.; Lian, T. Q. *Nano Lett* **2012,** 12, (1), 303-309.

21. Tisdale, W. A.; Zhu, X. Y. *P Natl Acad Sci USA* **2011,** 108, (3), 965-970.

22. Nicolau, Y. F. *Appl Surf Sc* **1985,** 22-3, (May), 1061-1074.

23. Park, S.; Clark, B. L.; Keszler, D. A.; Bender, J. P.; Wager, J. F.; Reynolds, T. A.; Herman, G. S. *Science* **2002,** 297, (5578), 65-65.

24. Barcelo, I.; Campina, J. M.; Lana-Villarreal, T.; Gomez, R. *Phys Chem Chem Phys* **2012,** 14, (16), 5801-5807.

25. Lee, H.; Leventis, H. C.; Moon, S. J.; Chen, P.; Ito, S.; Haque, S. A.; Torres, T.; Nuesch, F.; Geiger, T.; Zakeeruddin, S. M.; Gratzel, M.; Nazeeruddin, M. K. *Adv Funct Mater* **2009,** 19, (17), 2735-2742.

26. Lee, H. J.; Chen, P.; Moon, S. J.; Sauvage, F.; Sivula, K.; Bessho, T.; Gamelin, D. R.; Comte, P.; Zakeeruddin, S. M.; Il Seok, S.; Gratzel, M.; Nazeeruddin, M. K. *Langmuir* **2009,** 25, (13), 7602-7608.

27. Oh, S. J.; Berry, N. E.; Choi, J. H.; Gaulding, E. A.; Lin, H. F.; Paik, T.; Diroll, B. T.; Muramoto, S.; Murray, C. B.; Kagan, C. R. *Nano Lett* **2014,** 14, (3), 1559-1566.

28. Kim, D. K.; Fafarman, A. T.; Diroll, B. T.; Chan, S. H.; Gordon, T. R.; Murray, C. B.; Kagan, C. R. *Acs Nano* **2013,** 7, (10), 8760-8770.

29. Luther, J. M.; Pietryga, J. M. *Acs Nano* **2013,** 7, (3), 1845-1849.

30. Engel, J. H.; Alivisatos, A. P. *Chem Mater* **2014,** 26, (1), 153-162.

31. Thon, S. M.; Ip, A. H.; Voznyy, O.; Levina, L.; Kemp, K. W.; Carey, G. H.; Masala, S.; Sargent, E. H. *Acs Nano* **2013,** 7, (9), 7680-7688.

32. Li, J. J.; Wang, Y. A.; Guo, W. Z.; Keay, J. C.; Mishima, T. D.; Johnson, M. B.; Peng, X. G. *J Am Chem Soc* **2003,** 125, (41), 12567-12575.

33. Pijpers, J. J. H.; Koole, R.; Evers, W. H.; Houtepen, A. J.; Boehme, S.; Donega, C. D.; Vanmaekelbergh, D.; Bonn, M. *J Phys Chem C* **2010,** 114, (44), 18866-18873.

34. Canovas, E.; Moll, P.; Jensen, S. A.; Gao, Y. A.; Houtepen, A. J.; Siebbeles, L. D. A.; Kinge, S.; Bonn, M. *Nano Lett* **2011,** 11, (12), 5234-5239.

35. Ulbricht, R.; Hendry, E.; Shan, J.; Heinz, T. F.; Bonn, M. *Rev Mod Phys* **2011,** 83, (2), 543-586.

36. Zidek, K.; Zheng, K. B.; Ponseca, C. S.; Messing, M. E.; Wallenberg, L. R.; Chabera, P.; Abdellah, M.; Sundstrom, V.; Pullerits, T. *J Am Chem Soc* **2012,** 134, (29), 12110-12117.

37. Barcelo, I.; Lana-Villarreal, T.; Gomez, R. *J Photoch Photobio A* **2011,** 220, (1), 47-53.

38. Muller, P.; Kern, R. *J Cryst Growth* **1998,** 193, (1-2), 257-270.

39. Ferreira, S. O.; Neves, B. R. A.; Magalhaes-Paniago, R.; Malachias, A.; Rappl, P. H. O.; Ueta, A. Y.; Abramof, E.; Andrade, M. S. *J Cryst Growth* **2001,** 231, (1-2), 121-128.

40. Wang, F.; Shan, J.; Islam, M. A.; Herman, I. P.; Bonn, M.; Heinz, T. F. *Nat Mater* **2006,** 5, (11), 861-864.

41. Markus, T. Z.; Itzhakov, S.; Akotzer, Y. I.; Cahen, D.; Hodes, G.; Oron, D.; Naaman, R. *J Phys Chem C* **2011,** 115, (27), 13236-13241.

42. Walther, C.; Blum, R. P.; Niehus, H.; Masselink, W. T.; Thamm, A. *Phys Rev B* **1999,** 60, (20), R13962-R13965.

43. Kongkanand, A.; Tvrdy, K.; Takechi, K.; Kuno, M.; Kamat, P. V. *J Am Chem Soc* **2008,** 130, (12), 4007-4015.

44. Kim, D.; Kim, D. H.; Lee, J. H.; Grossman, J. C. *Phys Rev Lett* **2013,** 110, (19).

45. Oh, S. J.; Berry, N. E.; Choi, J. H.; Gaulding, E. A.; Paik, T.; Hong, S. H.; Murray, C. B.; Kagan, C. R. *Acs Nano* **2013,** 7, (3), 2413-2421.

46. Oh, S. J.; Uswachoke, C.; Zhao, T.; Choi, J.-H.; Diroll, B. T.; Murray, C. B.; Kagan, C. R. *Acs Nano* **2015**.

47. Weng, Y. X.; Wang, Y. Q.; Asbury, J. B.; Ghosh, H. N.; Lian, T. Q. *J Phys Chem B* **2000,** 104, (1), 93-104.

48. Green, A. N. M.; Palomares, E.; Haque, S. A.; Kroon, J. M.; Durrant, J. R. *J Phys Chem B* **2005,** 109, (25), 12525-12533.

49. Moreels, I.; Lambert, K.; De Muynck, D.; Vanhaecke, F.; Poelman, D.; Martins, J. C.; Allan, G.; Hens, Z. *Chem Mater* **2007,** 19, (25), 6101-6106.

50. Petkov, V.; Moreels, I.; Hens, Z.; Ren, Y. *Phys Rev B* **2010,** 81, (24).

51. de la Fuente, M. S.; Sanchez, R. S.; Gonzalez-Pedro, V.; Boix, P. P.; Mhaisalkar, S. G.; Rincon, M. E.; Bisquert, J.; Mora-Sero, I. *J Phys Chem Lett* **2013,** 4, (9), 1519-1525.

52. Tang, J.; Kemp, K. W.; Hoogland, S.; Jeong, K. S.; Liu, H.; Levina, L.; Furukawa, M.; Wang, X. H.; Debnath, R.; Cha, D. K.; Chou, K. W.; Fischer, A.; Amassian, A.; Asbury, J. B.; Sargent, E. H. *Nat Mater* **2011,** 10, (10), 765-771.

53. Voznyy, O.; Zhitomirsky, D.; Stadler, P.; Ning, Z. J.; Hoogland, S.; Sargent, E. H. *Acs Nano* **2012,** 6, (9), 8448-8455.

54. Doany, F. E.; Grischkowsky, D.; Chi, C. C. *Appl Phys Lett* **1987,** 50, (8), 460-462.

55. Lambsdorff, M.; Kuhl, J.; Rosenzweig, J.; Axmann, A.; Schneider, J. *Appl Phys Lett* **1991,** 58, (17), 1881-1883.

56. Cánovas, E.; Moll, P.; Jensen, S. A.; Gao, Y.; Houtepen, A. J.; Siebbeles, L. D. A.; Kinge, S.; Bonn, M. *Nano Letters* **2011,** 11, (12), 5234-5239.

57. Pijpers, J. J. H.; Koole, R.; Evers, W. H.; Houtepen, A. J.; Boehme, S.; de Mello Donegá, C.; Vanmaekelbergh, D.; Bonn, M. *The Journal of Physical Chemistry C* **2010,** 114, (44), 18866-18873.

58. Wang, H.; McNellis, E. R.; Kinge, S.; Bonn, M.; Cánovas, E. *Nano Letters* **2013**.

Chapter 5

Fermi Level Pinning at QD Sensitized Oxide Interfaces Precludes Tuning of Donor-Acceptor Energetics by QD Dipolar Molecular Capping

Reducing the driving excess energy for exciton dissociation (∆G) at quantum dot (QD)/oxide interfaces could pave the way towards improved photoconversion efficiencies in solar cells and fuels architectures. Recent works demonstrated that QD workfunction (and hence ∆G at electrodes) can be tuned by capping the semiconductor nanocrystals with molecular dipoles. However, the workfunction tunability in PbS QD-superlattices was reported to be ~20-fold larger when compared with those reported on CdS and CdSe QD sensitized schemes; the origin for the large mismatch in tunability for these systems remains unclear (e.g. whether dipole/QD interfacial chemistry or sample morphology determine ∆G tuning). Here, we demonstrate that interfacial electron transfer (ET) rates, correlating directly with ∆G, are invariant to the QD dipolar capping in PbS/SnO_2 interfaces. This result rules out the scenario where a specific dipole/QD surface chemistry dictates ∆G tunability, and can be attributed to Fermi level pinning at the QD/oxide interface. Furthermore, we demonstrate that ET dynamics at interfaces, and then ∆G, can be tuned by QD dipolar molecular capping when inserting an insulating layer in between QD donor and oxide acceptor. Our results reveal that tuning of donor-acceptor energetics in sensitized systems requires electronic decoupling between the QD and the oxide phases.

5.1 Introduction

Achieving efficient surface passivation schemes in quantum dot (QD) nanocrystals is essential for their implementation in novel optoelectronic devices.[1-5] The passivation of QD surfaces, which is commonly achieved by capping the semiconducting nanocrystals with molecular agents[3, 6, 7], inorganic shells[1, 8, 9], or atoms[4, 10, 11], suppresses non-radiative relaxation paths for photo-excited charge carriers. The effectiveness of a passivation treatment is determined by the nature of the physico-chemical interaction of QD surface and capping agents (*e.g.* type of bond, packing density, lattice matching *etc.*). Additionally, the synergy between QDs and their capping agents offers a plethora of opportunities for tuning and controlling nanocrystal stability[12] and QD optoelectronic properties[13, 14] such as bandgap[13-15], doping[16] and workfunction[17-19]. Core QD workfunction tuning could be enabled by exploiting molecular dipoles as a QD passivation shell. This approach is an appealing route for

sensitized geometries, as a single QD capping treatment can provide a reliable passivation scheme for the QDs, boosting the short circuit photocurrents in devices,[3, 19, 20] and allow fine tuning of donor-acceptor interfacial energetics,[17-19, 21] potentially enhancing open circuit voltage in solar cells[22]. In fact, exploiting QD dipolar molecular capping treatments have provided a path towards more efficient QD based solar cells in bulk heterojunction[21] and sensitized cell architectures[17, 23].

The workfunction tunability of semiconductor surfaces by dipolar molecular treatments[24-26] can be qualitatively classified according to the organic-inorganic composite interfacial coupling strength (e.g. weak or strong, physisorption or chemisorption).[25, 27, 28] For weakly coupled interfaces, the modulation of surface energetics by molecular dipoles can be modeled by the Helmholtz equation:[25, 28]

$$\Delta V = \frac{N * \mu * cos\theta}{\varepsilon * \varepsilon_0}, \qquad \text{Equation 5.1,}$$

where ΔV represents the potential drop across the molecular film, N the number of absorbed molecules/area at the surface, μ the molecular dipole moment, and θ the molecular binding angle with respect to the surface normal; ε and ε_0 denote the permittivity of the molecule and vacuum, respectively. Equation 5 illustrates that in the weak coupling regime the workfunction of semiconductor surface increases in proportion to the dipole moment of the capping molecules. This proportionality seems to be a general phenomenon among many bulk[29-31] and polycrystalline[32] semiconductors, yet the quantitative strength of the interaction, i.e. the proportionality constant, $\Delta V/\mu$, seems to be highly dependent on the nature of the interfaces.[29] Similarly, for semiconducting QDs, although linear $\Delta V/\mu$ responses have been reported for QD-superlattices and QD/oxide surfaces; the workfunction tunability was found to be ~20-fold larger in PbS QD-superlattices when compared with those reported on in-situ nucleated CdS/TiO_2 and CdSe/TiO_2 QD/oxide interfaces (~400 meV/Debye vs ~20 meV/Debye respectively)[17, 18, 23]. The weaker workfunction tunability in QD sensitized oxides needs to be rationalized; e.g. *does material interfacial chemistry determine the* $\Delta V/\mu$ *value in sensitized systems (e.g. PbS vs CdS)?;* if this is the case, PbS QDs sensitizing a mesoporous oxide will display the ~400 meV/Debye found in colloidal superlattices. Note that the $\Delta V/\mu$ ratio will determine the degree of tunability for the exciton dissociation driving energy, ΔG, in a given system; where ΔG is defined as the energy difference between the QD LUMO and oxide CB workfunctions. In turn the ΔG value, which can be considered simply as a thermal loss at the electrodes, will ultimately determine the maximum efficiency for a sensitized solar cell[22]. Understanding these aspects is crucial for further development of QD sensitized solar cells.

In order to interrogate whether the specific dipole/QD surface chemistry sets the $\Delta V/\mu$ ratio, and hence the degree of donor-acceptor ΔG tunability on sensitized QD/oxide systems, we analyze here the interplay between QD dipolar molecular capping and interfacial electron transfer (ET) dynamics in a system where PbS QDs were directly nucleated onto a mesoporous SnO_2 matrix. We demonstrate that the interfacial ET rates (directly correlated with donor-acceptor ΔG) are invariant to the molecular

dipolar moment sign and strength at PbS/SnO_2 interfaces. These results rule out the scenario where a specific dipole/QD surface chemistry dictates the $\Delta V/\mu$ ratio, and can be rationalized by Fermi level pinning at the QD/oxide interface precluding the modulation of donor-acceptor energetics for any dipolar capping treatments. Furthermore, we demonstrate that by placing an inorganic insulating oxide layer between QD and oxide, pinning effects are removed and the tunability of donor-acceptor energetics is enabled. This illustrate that the tunability of interfacial donor-acceptor energetics in QD sensitized oxides by molecular dipoles requires decoupling of the QD and the oxide. Our results set design rule principles for optimized sensitized solar cells where thermal losses at the electrodes are engineered and reduced.

5.2 Methods and Materials

Bare PbS QDs were nucleated in-situ onto mesoporous SnO_2 electrodes by using the successive ionic layer adsorption and reaction (SILAR) approach in a glove box under N_2 atmosphere. The capping-free-grown QDs after 2 SILAR cycles are defined by a bandgap of ~0.9 ±0.1 eV[11]. QD molecular treatments with different dipolar moments were achieved by immersing QD/oxide electrodes for 2 hours in 0.1 M MeOH solutions for each given molecule and the details are given in chapter 2, sample preparation section.

5.3 Results and Discussions

The effective bonding of molecules to the QDs was verified for all samples as discussed in the Appendix. Figure 5.1 summarizes the set of molecules analyzed in this work, with dipole moments ranging from -3.2 to +4.76 Debye. All molecules contain a thiol group that serves as a selective anchoring site to the PbS QDs.[2, 3, 33] Interfacial carrier dynamics on a given sample spot before (QD/oxide) and after applying the molecular treatment (dipole/QD/oxide) were evaluated by optical pump-THz probe (OPTP) spectroscopy. This technique provides time-resolved photoconductivity with a sub-ps resolution and has been proven to be a powerful tool for investigating ET processes in QD sensitized systems.[1, 11, 34-36] Following optical excitation of the QDs (800nm, ~50 fs FWHM), the time-dependent pump-induced absorption of the THz probe directly reveal ET processes from the QD donor to the oxide acceptor.[11, 34] All OPTP measurements were performed under vacuum conditions (< 1.4×10^{-4} mbar) to avoid photo-oxidation of the QDs. Up to 5 different sample spots were measured for each sample, the variation of signal amplitudes is within 3-8% indicating the good homogeneity of the films and reproducibility of the measurements.

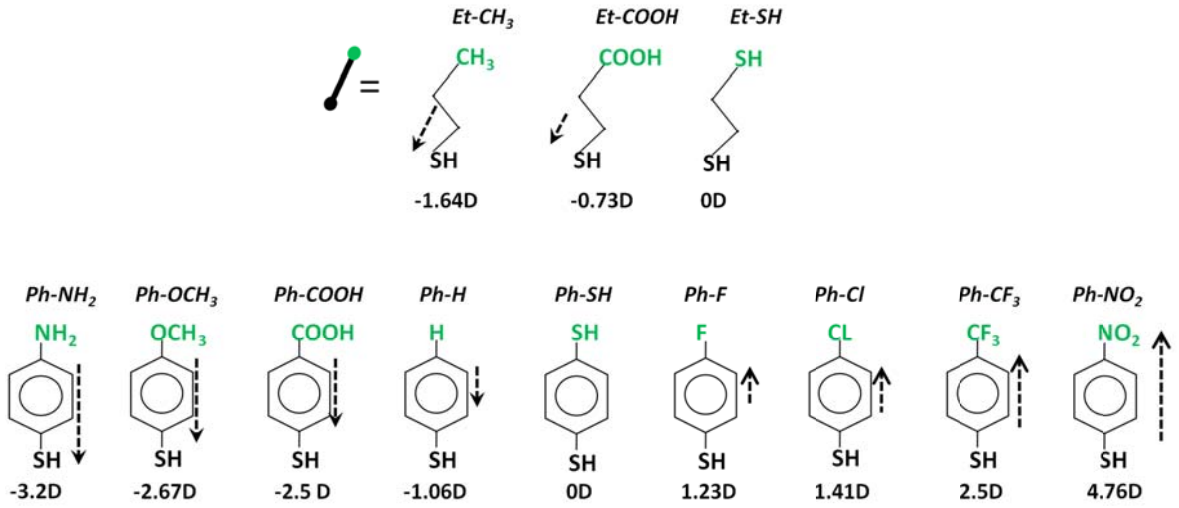

Figure 5.1 Set of molecules analyzed in this work. Et- and Ph- refers to ethylene (SH-CH_2-CH_2-) and phenylene (SH-C_6H_4-) based samples. The arrows indicate the direction of molecular dipoles moment in the gas phase, which were estimated by first principles calculations.

5.3.1 Estimates of dipole moments, capping density and bonding tilt angle by first principle calculations

As is seen in equation 5.1, the relative change in ΔV (correlated with a change in workfunction)[25, 29] is directly proportional to the molecular dipole moment, μ; the number of attached molecules per unit area, N; and the angle of the molecule towards the semiconductor surface normal, θ. In order to weight the impact of these variables on the monitored interfacial dipole/QD/oxide ET rates by OPTP (see below) we performed first-principles calculations.

We prepared the system composed of the isolated molecules, bare PbS (111) and (100) surfaces, and the molecules attached on these surfaces with varying the number of the molecules per unit area. The (111) and (100) surface are the most representative crystal facets for our PbS/SnO_2 samples[11]. In this calculation, we used four molecules of Ph-OCH_3, Ph-COOH, Ph-H, and Ph-NO_2 as representative cases. After optimizing these structures we computed the binding energies of the four molecules onto PbS(111) and (100) surfaces, and obtained angles formed by the molecules towards the surface normal (calculation details are provided in the Appendix 5.5.2). Figure 5.2(A) displays the variation of the binding energy when the number of attached molecules increases from n to $n+m$ ($\Delta E_{n\rightarrow n+m}$). A negative (positive) $\Delta E_{n\rightarrow n+m}$ indicates that the molecule absorbed on the substrate is energetically stable (unstable) when an additional molecule is adsorbed on the system characterized by n molecules attached on the surface. The variations of the binding energies estimates are plotted in figure 5.2(A). As is clear from this figure, we find that up to 8 molecules can be adsorbed onto a 14.5 Å × 16.8 Å PbS(111) slab surface area. When more than eight molecules are attached on the surface, the binding energy becomes positive, indicating that more than eight molecules are unlikely to be attached to the

14.5 Å × 16.8 Å PbS(111) surface. For the PbS(100) surface, the simulated binding energy is positive independent of the molecular dipole moment, indicating none the molecules bind onto the PbS(100) surface under these conditions. Sequentially, we surveyed the orientations of the molecules with respect to the semiconductor surface, θ, by computing the angle formed by the C-S bond to the PbS surface normal. Calculated angles are summarized in Fig. 2(B), while two snapshots for the optimized Ph-NO_2 and Ph-OCH_3 molecules onto the PbS(111) surface are depicted in Fig. 2(C) and (D), respectively. As is shown in Fig. 2(B), θ is very identical for these molecules, indicating that the tilt angle is insensitive to the molecular dipole moment in our calculations. Based on these first-principles calculations we can conclude that packing, binding energy and tilt angle are insensitive to the specific dipole moments of the molecules. These results allow us then to interrogate meaningfully the impact of dipolar moment vs donor-acceptor ET rates for the PbS/SnO_2 system.

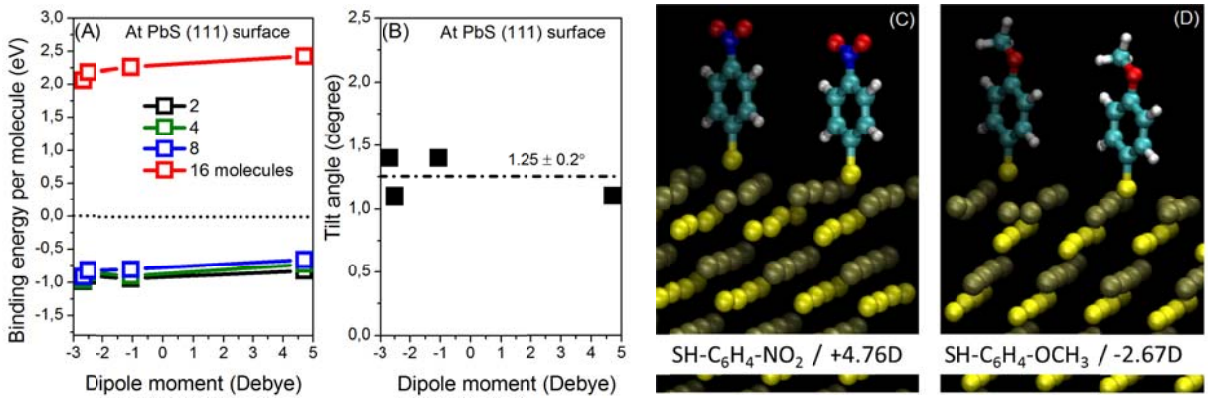

Figure 5.2 (A) Binding energy per molecule for Ph-OCH_3, Ph-COOH, Ph-H, and Ph-NO_2 deposited onto PbS(111) surfaces as a function of molecular packing density (2, 4, 8 and 16 molecules binding onto a 14.5 Å × 16.8 Å PbS(111) slab surface area); (B) molecular tilt angle towards PbS(111) surface normal as a function of gas phase dipolar moment (invariant vs packing density); (C-D) Optimized structure of Ph-NO_2 and Ph-OCH_3 molecules attached to PbS(111) surface illustrating similar morphology.

5.3.2 The impact of QD dipolar molecular capping on QD/oxide ET rate

A direct correlation between bigger QD/oxide donor-acceptor driving force (ΔG) and faster ET rates has been reported before by us[34] and others[34, 37]. Consequently, the variations in donor-acceptor energetics induced by QD dipolar molecular capping can be detected as the changes in the ET rate from the QD to the oxide in OPTP measurements. Here, interfacial carrier dynamics were measured in a single sample spot before and after functionalizing the QDs with dipolar molecular ligands. In figure 5.3(A-C) we show normalized OPTP ET dynamics before and after QD molecular dipolar treatments for molecules displaying dipole moments -2.5, 0 and +2.5 Debye; in figure 5.3(D) we summarize the variation induced by molecular QD capping in ET dynamics for all analyzed samples. As evident from these figures, QD capping by different molecular treatments do not affect ET dynamics as a function of dipole moment; neither as a function of molecular backbone nature, e.g. distinct polarizability of

phenyl vs ethyl based molecules. The results shown in figure 5.3 allow us to conclude that QD molecular dipolar capping is not affecting the donor-acceptor coupling neither the energetics (ΔG) in the analyzed PbS/SnO_2 systems. Note that changes in ET driving energy $\Delta G \leq 40$ meV have been clearly resolved as changes in ET rates from OPTP measurements[34]; this suggest that changes in ΔG induced by molecular capping as low as $\Delta G/\mu \leq 5$ meV are characteristic for our samples.

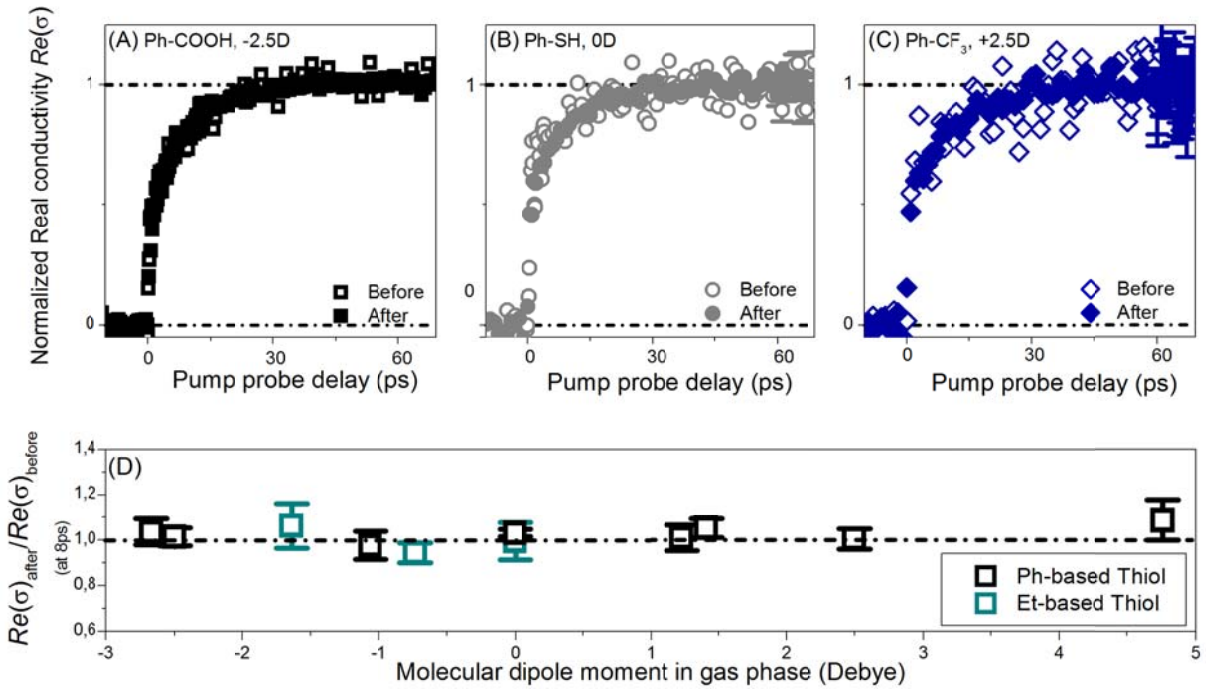

Figure 5.3 Comparison of normalized OPTP early dynamics before and after molecular dipolar capping of the QDs by (A) Ph-COOH, (B) Ph-SH, and (C) Ph-NO_2 molecules. (D) The real conductivity ratio for OPTP dynamics before and after molecular dipolar capping (8 ps after photoexcitation). The errors represent deviations inferred among 5 different sample's spots.

Previous work on chemically equivalent (PbS QDs), but morphologically different samples (QD solids) revealed changes in work functions as large as ~400 meV/Debye.[18] On the other hand, for chemically different yet morphologically similar samples consisting on cadmium based QDs nucleated in-situ onto TiO_2, a ~20 mV/Debye solar cell photovoltage onset variation was reported.[17] These results clearly indicate that interfacial dipole/QD specific chemistry alone (e.g. PbS or CdS) is not sufficient to co-determine the impact of QD dipolar capping on QD/oxide energetics, an indication of the important role of the oxide electrode towards the degree of QD workfunction tunability. Our results can be rationalized by Fermi level pining at the PbS/SnO_2 QD/oxide interface (e.g. fixing donor-acceptor ΔG); this rational is fully consistent with our previous report for this specific system where we found QD size independent QD to oxide ET rates[11]. In addition, strong pinning effects have been unambiguously resolved for CdSe QDs molecularly bridged to TiO_2 electrodes.[38] Therefore, the modest inferred tunability of photovoltage onset (~20 mV/Debye) for in-situ nucleated CdSe QDs onto TiO_2 electrodes[17] seems to have a similar origin that the one reported here. In this respect, our results

do rationalize the observations made in previous reports regarding the distinct contrast of workfunction tunability degree by capping QDs with molecular dipoles in colloidal QD superlattices (~400 meV/Debye[18]) and in QD dots sensitizing a mesoporous oxide matrix (~20 mV/Debye[17]); Fermi level pinning at QD/oxide interfaces can preclude ΔG tuning.

5.3.3 The impact of QD dipolar molecular capping on QD/oxide back ET (BET) rate

A recent work found a bandgap narrowing in PbS QDs[15] treated with three dipolar molecular capping analyzed here (Ph-CF_3, Ph-NH_2, Ph-H); this effect was found to be determined primarily by the nature of the molecular head group (e.g. thiol) rather than the specific dipole moment of QD capping molecules. Considering system energetics ΔG, a dipole independent bandgap narrowing in the QDs for our samples should be manifested as a dipole independent slowdown in back electron transfer (BET) rates.[11] Although we resolve experimentally that the molecularly induced changes in BET rate are invariant vs the specific dipole moment employed for capping the QDs, see figure 5.4(A-E). Contrary to expectations, we find a speed up of BET rates. This should be indicative of a widening in QD bandgap onset induced by molecular capping for our samples; indeed absorption measurements for samples before and after molecular treatment confirmed a ~40 meV QD bandgap increase induced by molecular capping, but independent of dipolar moment (see figure 5.8 in Appendix 5.5.3). The observation of a QD bandgap widening after molecular capping in our samples could be connected with strain release from the lattice-matched epitaxially grown PbS nanocrystal onto the SnO_2 matrix.[11, 39, 40] Note that the inferred bandgap for our bare PbS nanocrystals (~0.9 ± 0.1 eV) is much narrower than that expected for a nanocrystal of similar volume[41, 42]; a bandgap narrowing is a common phenomenon observed in epitaxially grown QDs owing to the lattice mismatch between dot and substrate[11,43]. In line with this discussion, a similar blue energy shift induced by capping has been reported for CdSe QDs directly nucleated onto a TiO_2 oxide matrix[22]. Further work would be required to elucidate the details of this molecular induced strain release effect.

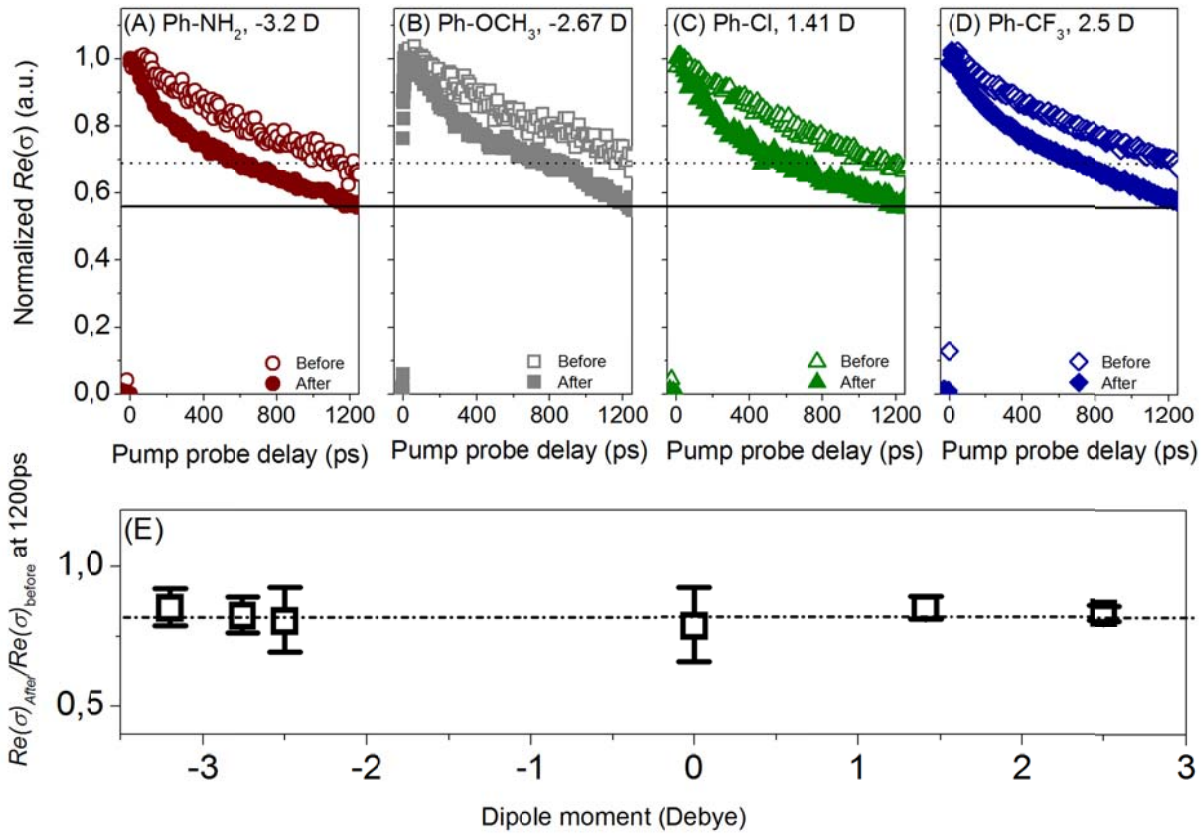

Figure 5.4 (A-D) Comparison of the normalized OPTP dynamics before and after QD molecular capping in 1200ps time window. (E) The ratio of OPTP responses at 1200ps pump-probe delay before and after QD molecular capping.

5.3.4 Decoupling QD/oxide interface by an insulating layer allows tuning of donor-acceptor energetics by QD dipolar molecular capping

Pining of donor-acceptor energetics represents a general interfacial phenomena which has been found on chemically and morphologically distinct interfaces (e.g. QD/oxide systems[38, 44-46], bulk semiconductor/semiconductor or semiconductor/liquid interfaces[47], metal/organic polymer interfaces[48, 49] *etc.*). While the pinning effects preclude the formation of Ohmic contacts at interfaces, they can be generally bypassed by inserting an insulating layer between donor and acceptor.[50, 51] In order to demonstrate that a similar treatment could allow fine tuning of donor-acceptor energetics in QD sensitized oxides we prepared a sample consisting of 2 SILAR cycles PbS QDs directly nucleated onto shell/core SiO_2/SnO_2 mesoporous electrode (details for sample preparation are given in chapter 2). Following the same approach described previously, we characterized the impact of a QD dipolar molecular capping on ET and BET dynamics by OPTP. As shown in figure 5.5, interfacial electron dynamics become tunable after QD molecular treatment in this case. Specifically, a sample following molecular -2.5 Debye Ph-COOH treatment show a speed up and slow down for ET and BET rates respectively. As sketched in figure 5(B), these results are consistent with an increase (reduction) in donor-acceptor Free Gibbs energy from ΔG_{ET} to ΔG_{ET}* (and ΔG_{BET} to ΔG_{BET}*) respectively. Within

this scenario, and taking as a reference the *linear* correlation between ET rates and donor-acceptor energetics inferred by us in QD size dependent PbSe/3MPA/SnO_2 systems[35] (3MPA refers here to 3-mercaptopropionic acid), we can estimate a change in donor acceptor energetics of ~80 meV/Debye for the PbS/SiO_2/SnO_2 system. This value represents 4-fold improvement vs previous reports for in-situ nucleated QD sensitized systems.[17, 23]

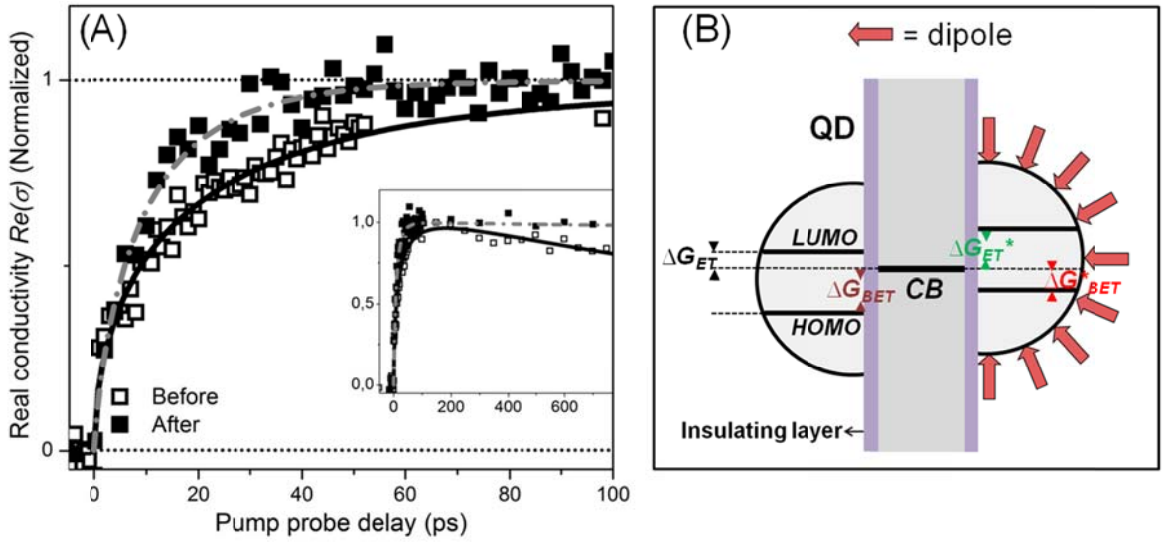

Figure 5.5 (A) Comparison OPTP dynamics in QD/SiO_2/SnO_2 systems before (open dots) and after (solid dots) capping PbS QDs with SH-C_6H_4-COOH (-2.5 Debye) molecular dipoles. (B) Sketch illustrating the effect of the molecular QD treatment on system energetics in QD/SiO_2/SnO_2 systems, ΔG_{ET}, ΔG_{BET}, ΔG_{ET}* and ΔG_{BET}* represent donor-acceptor Free Gibbs energy for ET and BET respectively.

5.4 Summary

Tuning interfacial donor-acceptor energetics in nanostructured systems can pave the way towards highly efficient optoelectronic applications. Regarding QD-sensitized oxides, relevant systems for solar energy conversion architectures, we demonstrate here that Fermi level pinning at QD sensitized oxide interfaces preclude tuning of donor-acceptor energetics by QD dipolar molecular capping. By placing an insulating layer between donor and acceptor, tuning of donor-acceptor energetics in QD sensitized oxides by QD dipolar molecular capping is enabled. The feasibility and potential of establishing Ohmic contacts between QD levels and electrode contacts must be reevaluated on QD sensitized solar cells exploiting our approach – as it has the potential of boosting open circuit voltages, and efficiencies, in complete devices.

5.5 Appendix

5.5.1 The impact of QD dipolar molecular capping on QD/oxide ET efficiency

In chapter 4, we have demonstrated that the boost in QD/oxide ET efficiency induced by a specific QD passivation treatment can be quantified by OPTP measurements. In order to interrogate experimentally the effectiveness (e.g. bonding and packing density) of our molecular treatments on QD/oxide electrodes grown by SILAR we follow here the same approach; where the boost in ET efficiency (passivation efficiency, PE) can be defined as[11]:

$$PE = (Re(\sigma)_{after} - Re(\sigma)_{before}) / Re(\sigma)_{after}), \quad \text{Equation. 5.2,}$$

here $Re(\sigma)_{before}$ and $Re(\sigma)_{after}$ refer to the OPTP plateau amplitude (when ET is ended) before and after a specific passivation treatment. Figure 5.6 (A) shows an example of the boost in OPTP signal monitored in a single QD/oxide sample's spot before and after being passivated by Ph-COOH molecules. As evident from the plot the overall real conductivity amplitude is approximately doubled by this specific molecular capping treatment (following EQ 2, this represents a PE~100% - please note here that this value is size dependent[11] and do not necessarily refer to unity passivation quantum yield induced by the thiol[52, 53]). This observation serves as a verification of an effective molecular capping of QDs when exploiting thiol-based linkers as passivation agents[2, 3]. Notably, the PE value estimated here quantitatively matches our previous findings - inferred for this exact system - when applying atomic passivation through QD surface stoichiometry tuning from p- to n-type[11] (see figure 5.6 (B), Pb passivation). Note that as illustrated in figure 5.1, the employed molecular dipole is expected to have an electron donating character towards the oxide surface near the SH group, which can be consistent with a dipole/QD n-type-like interface. In figure 5.6 (B) we summarize the PE efficiency for all the molecules analyzed in this work. The molecules defined by negative dipoles exhibit, within the noise of our estimates, the comparable improvement in PE independently of dipole moment strength. On the other hand, we find no difference between the PE efficiency resolved by molecules with phenyl *vs.* ethyl based backbones (grey and black squared in figure 5.6 (B)) which could indicate that steric effects potentially affecting packing density are not promoted by the molecules defined by un-

saturated backbones. As evident from figure 5.6 (B), the molecules defined by negative dipoles exhibit a ~2-fold improvement in PE when compared with molecules defined by positive dipoles; this observation, following equation 5.2, could simply indicate that QD surface related trap acceptors partially *survive* the passivation treatment when capped with positive dipoles (e.g. lead oxide species[38]). We are interrogating at present this effect, the outcome will not change the conclusions derived in this work (following equation 5.1, different packing density will only change the inferred slope of $\Delta V(\mu)$ for positive and negative dipole regions), then these results are out of the scope of the present letter and will be reported elsewhere.

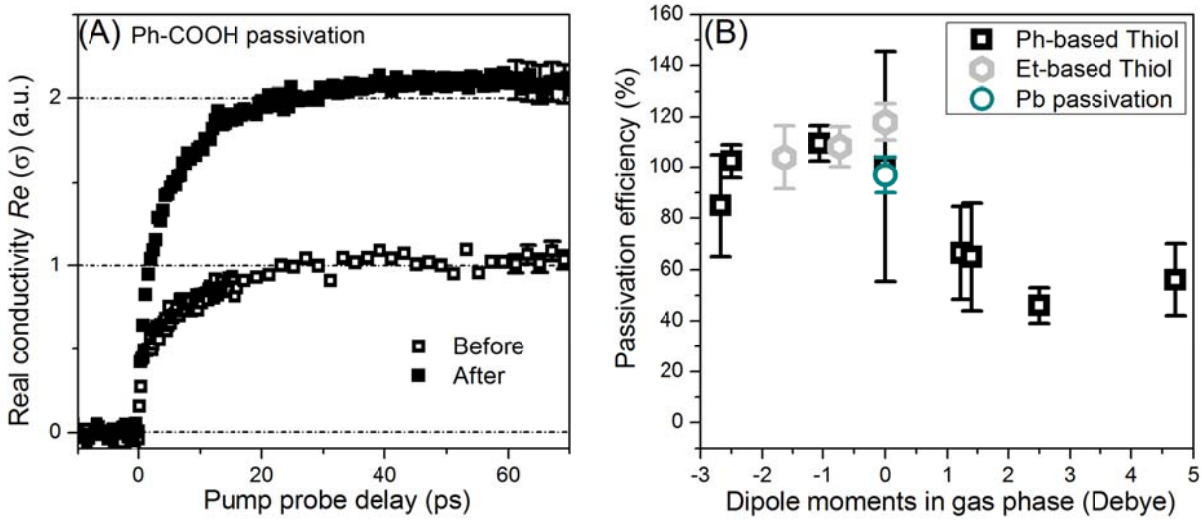

Figure 5.6 Passivation efficiency (as defined in the text) of molecules onto PbS QDs with different dipole moments. (A) An example illustrating the change in OPTP amplitude before and after Ph-COOH PbS QD passivation; (2) Passivation efficiency vs the gas phase dipole moments within the range of analyzed molecules. The passivation effect with Pb atom is shown for comparison.

5.5.2 First Principle Calculations

To examine the biding energy and packing conformations of the molecules attached on the PbS surface as well as the molecular dipole moment for the isolated molecules, we performed the first-principles calculations.

The dipole moments of the isolated molecules listed in figure 1 (B) in the main text were calculated with the GAMESS package[54]. We used the cc-pVTZ basis set and the B3LYP functionals for the optimization of the molecular structure as well as for computing the dipole moments.

For exploring the binding energy of the molecules on the PbS surface and packing conformations, we calculated the total energy of the system for molecules attached on the PbS surface ($E_{mol+PbS}$), the energy of the bare PbS surface (E_{PbS}), and the energy of the isolated molecules (E_{mol}) with the SIESTA code package.[55] We prepared the PbS (100) and (111) surfaces within the slab model. The PbS slab model was composed of three PbS layers, where the structure of the topmost 1 layer along the *z*-direction were optimized, while the atom positions for the rest of the two layers were fixed. Note that the topmost layer in this study means that the layer where the molecules were attached. The size of the cell was 11.872 Å × 11.872 Å × 35 Å for the (100) surface and 14.540 Å × 16.792 Å × 35 Å for the (111) surface with periodic boundary conditions. The *x*- and *y*-directions of the cell size was set to the experimentally measured lattice constant. We used the Troullier-Martins norm-conserving pseudopotential[56] with the Kleinman-Bylander nonlocal projector[57] for describing the core electrons. We used the PBE functions and DZP basis set. The *k*-points were sampled by 5 × 5 × 1. Note that the same calculation conditions were used for all the systems of molecules absorbed on the PbS surface, isolated molecules, and bare PbS surface. For the cases of the molecules absorbed on the PbS surface, the H atoms next to S atoms of the thiol molecules were dissociated from the molecules and were placed on the PbS surface where the molecules were not attached. The binding energy of a molecule when *m* molecules are added onto the PbS surface where *n* molecules are attached ($\Delta E_{n\rightarrow n+m}$) can be computed from

$$\Delta E_{n\rightarrow n+m} = \frac{E_{n+m,PbS} - E_{n,PbS}}{m} - E_{mol}, \quad \text{Equation 5.3,}$$

where $E_{n,PbS}$ is the conformation energy of the system of *n* molecules attached on the PbS surface, E_{mol} is the energy of a single isolated molecule, and E_{PbS} is the energy of the bare PbS surface. The molecular geometries of the Ph-NO_2 molecules absorbed on the PbS (111) surface as well as PbS (100) surface are displayed in Fig. S3. The calculated bonding is plotted in Fig. 2(A) in the main text. The angles of the molecules absorbed on the PbS surface and surface normal were calculated by using the optimized structure for two molecules absorbed on the PbS (111) surface. The data are given in Fig. 2(B) in the main text.

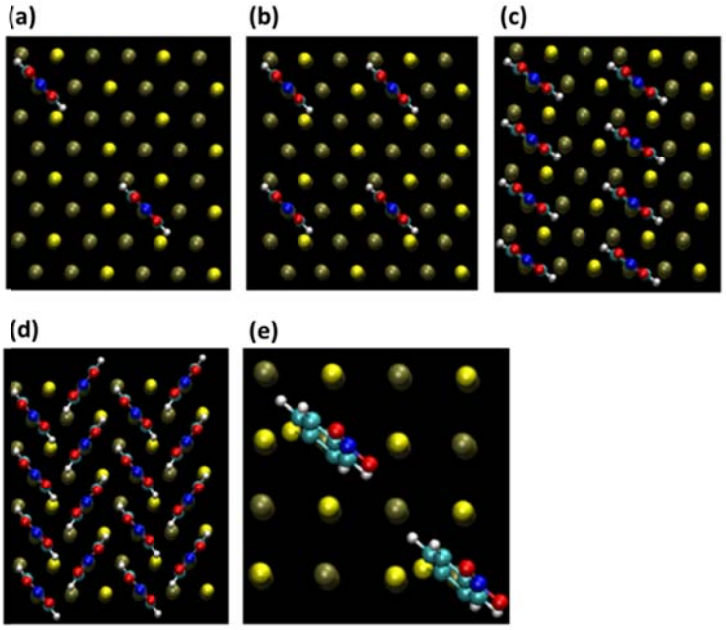

Figure 5.7 The top views of the optimized molecular structures. (a) Two, (b) four, (c) eight, and (d) sixteen Ph-NO_2 molecules are bonded to the PbS(111) surface, while (e) two molecules are adsorbed on the PbS(100) surface. H, C, N, O, S, and Pb atoms are denoted in white, sky blue, red, blue, yellow, and brown colors, respectively.

5.5.3 Absorption comparison with/without molecular passivation

In figure 5.8, we show the absorption spectra of QDs before and after adding of 2 dipolar molecules (Ph-COOH with -2.5 D and Ph-NO_2 with -4.76 D). A blue shift ~40 meV of PbS QD bandgap has been observed induced by molecular capping (for both cases).

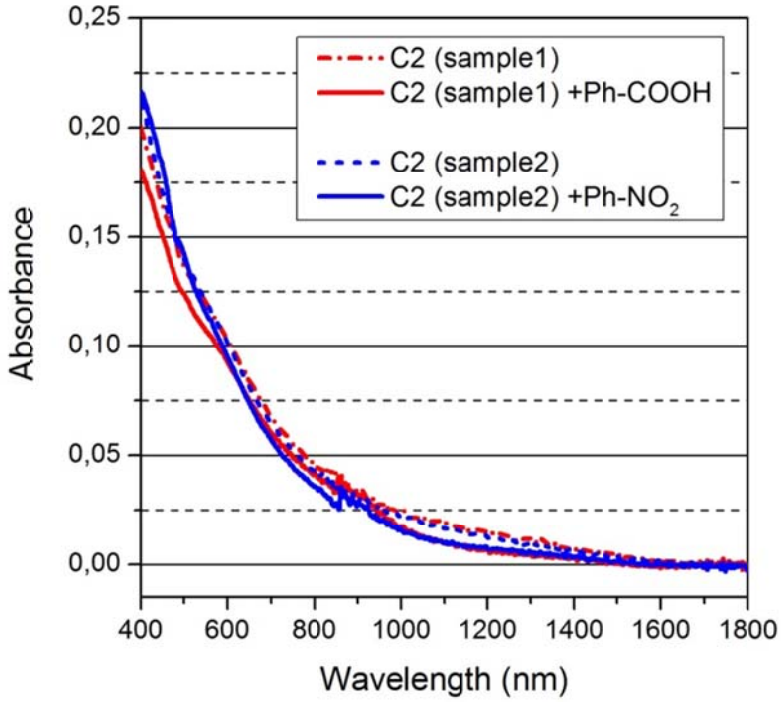

Figure 5.8 QD absorption change before and after molecular passivation (Ph-COOH and Ph-NO_2) for C2 PbS on SnO_2.

Reference

1. Zhao, K.; Pan, Z.; Mora-Seró, I.; Cánovas, E.; Wang, H.; Song, Y.; Gong, X.; Wang, J.; Bonn, M.; Bisquert, J.; Zhong, X. *J Am Chem Soc* **2015**.
2. Barkhouse, D. A. R.; Pattantyus-Abraham, A. G.; Levina, L.; Sargent, E. H. *Acs Nano* **2008,** 2, (11), 2356-2362.
3. de la Fuente, M. S.; Sanchez, R. S.; Gonzalez-Pedro, V.; Boix, P. P.; Mhaisalkar, S. G.; Rincon, M. E.; Bisquert, J.; Mora-Sero, I. *J Phys Chem Lett* **2013,** 4, (9), 1519-1525.
4. Tang, J.; Kemp, K. W.; Hoogland, S.; Jeong, K. S.; Liu, H.; Levina, L.; Furukawa, M.; Wang, X. H.; Debnath, R.; Cha, D. K.; Chou, K. W.; Fischer, A.; Amassian, A.; Asbury, J. B.; Sargent, E. H. *Nat Mater* **2011,** 10, (10), 765-771.
5. Zhang, J. B.; Gao, J. B.; Church, C. P.; Miller, E. M.; Luther, J. M.; Klimov, V. I.; Beard, M. C. *Nano Lett* **2014,** 14, (10), 6010-6015.
6. Wuister, S. F.; Donega, C. D.; Meijerink, A. *J Phys Chem B* **2004,** 108, (45), 17393-17397.
7. Anderson, N. C.; Hendricks, M. P.; Choi, J. J.; Owen, J. S. *J Am Chem Soc* **2013,** 135, (49), 18536-18548.
8. Kuno, M.; Lee, J. K.; Dabbousi, B. O.; Mikulec, F. V.; Bawendi, M. G. *J Chem Phys* **1997,** 106, (23), 9869-9882.
9. Hines, M. A.; Guyot-Sionnest, P. *J Phys Chem-Us* **1996,** 100, (2), 468-471.
10. Oh, S. J.; Berry, N. E.; Choi, J. H.; Gaulding, E. A.; Paik, T.; Hong, S. H.; Murray, C. B.; Kagan, C. R. *Acs Nano* **2013,** 7, (3), 2413-2421.
11. Wang, H.; Barcelo, I.; Lana-Vilarreal, T.; Gomez, R.; Bonn, M.; Canovas, E. *Nano Lett* **2014,** 14, (10), 5780-5786.
12. Woo, J. Y.; Ko, J. H.; Song, J. H.; Kim, K.; Choi, H.; Kim, Y. H.; Lee, D. C.; Jeong, S. *J Am Chem Soc* **2014,** 136, (25), 8883-8886.
13. Frederick, M. T.; Amin, V. A.; Swenson, N. K.; Ho, A. Y.; Weiss, E. A. *Nano Lett* **2013,** 13, (1), 287-292.
14. Frederick, M. T.; Amin, V. A.; Weiss, E. A. *J Phys Chem Lett* **2013,** 4, (4), 634-640.
15. Giansante, C.; Infante, I.; Fabiano, E.; Grisorio, R.; Suranna, G. P.; Gigli, G. *J Am Chem Soc* **2015,** 137, (5), 1875-1886.
16. Voznyy, O.; Zhitomirsky, D.; Stadler, P.; Ning, Z. J.; Hoogland, S.; Sargent, E. H. *Acs Nano* **2012,** 6, (9), 8448-8455.
17. Shalom, M.; Ruhle, S.; Hod, I.; Yahav, S.; Zaban, A. *J Am Chem Soc* **2009,** 131, (29), 9876-+.
18. Brown, P. R.; Kim, D.; Lunt, R. R.; Zhao, N.; Bawendi, M. G.; Grossman, J. C.; Bulovic, V. *Acs Nano* **2014,** 8, (6), 5863-5872.
19. Santra, P. K.; Palmstrom, A. F.; Tanskanen, J. T.; Yang, N.; Bent, S. F. *J Phys Chem C* **2015,** 119, (6), 2996-3005.

20. Wang, J.; Mora-Sero, I.; Pan, Z. X.; Zhao, K.; Zhang, H.; Feng, Y. Y.; Yang, G.; Zhong, X. H.; Bisquert, J. *J Am Chem Soc* **2013,** 135, (42), 15913-15922.

21. Chuang, C. H. M.; Brown, P. R.; Bulovic, V.; Bawendi, M. G. *Nat Mater* **2014,** 13, (8), 796-801.

22. Giebink, N. C.; Wiederrecht, G. P.; Wasielewski, M. R.; Forrest, S. R. *Phys Rev B* **2011,** 83, (19).

23. Barea, E. M.; Shalom, M.; Gimenez, S.; Hod, I.; Mora-Sero, I.; Zaban, A.; Bisquert, J. *J Am Chem Soc* **2010,** 132, (19), 6834-6839.

24. Vilan, A.; Shanzer, A.; Cahen, D. *Nature* **2000,** 404, (6774), 166-168.

25. Cahen, D.; Kahn, A. *Adv Mater* **2003,** 15, (4), 271-277.

26. Haick, H.; Cahen, D. *Accounts Chem Res* **2008,** 41, (3), 359-366.

27. Seker, F.; Meeker, K.; Kuech, T. F.; Ellis, A. B. *Chemical Reviews* **2000,** 100, (7), 2505-2536.

28. Selzer, Y.; Cahen, D. *Adv Mater* **2001,** 13, (7), 508-511.

29. Ashkenasy, G.; Cahen, D.; Cohen, R.; Shanzer, A.; Vilan, A. *Accounts Chem Res* **2002,** 35, (2), 121-128.

30. Bruening, M.; Moons, E.; Yaronmarcovich, D.; Cahen, D.; Libman, J.; Shanzer, A. *J Am Chem Soc* **1994,** 116, (7), 2972-2977.

31. Bruening, M.; Moons, E.; Cahen, D.; Shanzer, A. *J Phys Chem-Us* **1995,** 99, (20), 8368-8373.

32. Kruger, J.; Bach, U.; Gratzel, M. *Adv Mater* **2000,** 12, (6), 447-+.

33. Jeong, S.; Achermann, M.; Nanda, J.; Lvanov, S.; Klimov, V. I.; Hollingsworth, J. A. *J Am Chem Soc* **2005,** 127, (29), 10126-10127.

34. Canovas, E.; Moll, P.; Jensen, S. A.; Gao, Y. A.; Houtepen, A. J.; Siebbeles, L. D. A.; Kinge, S.; Bonn, M. *Nano Lett* **2011,** 11, (12), 5234-5239.

35. Pijpers, J. J. H.; Koole, R.; Evers, W. H.; Houtepen, A. J.; Boehme, S.; Donega, C. D.; Vanmaekelbergh, D.; Bonn, M. *J Phys Chem C* **2010,** 114, (44), 18866-18873.

36. Wang, H.; McNellis, E. R.; Kinge, S.; Bonn, M.; Canovas, E. *Nano Lett* **2013,** 13, (11), 5311-5315.

37. Robel, I.; Kuno, M.; Kamat, P. V. *J Am Chem Soc* **2007,** 129, (14), 4136-+.

38. Markus, T. Z.; Itzhakov, S.; Akotzer, Y. I.; Cahen, D.; Hodes, G.; Oron, D.; Naaman, R. *J Phys Chem C* **2011,** 115, (27), 13236-13241.

39. Trejo, O.; Roelofs, K. E.; Xu, S.; Logar, M.; Sarangi, R.; Nordlund, D.; Dadlani, A. L.; Kravec, R.; Dasgupta, N. P.; Bent, S. F.; Prinz, F. B. *Nano Lett* **2015**.

40. Bryant, G. W.; Zielinski, M.; Malkova, N.; Sims, J.; Jaskolski, W.; Aizpurua, J. *Phys Rev Lett* **2010,** 105, (6).

41. Wise, F. W. *Accounts Chem Res* **2000,** 33, (11), 773-780.

42. Moreels, I.; Lambert, K.; Smeets, D.; De Muynck, D.; Nollet, T.; Martins, J. C.; Vanhaecke, F.; Vantomme, A.; Delerue, C.; Allan, G.; Hens, Z. *Acs Nano* **2009,** 3, (10), 3023-3030.

43. Simmonds, P. J.; Yerino, C. D.; Sun, M.; Liang, B. L.; Huffaker, D. L.; Dorogan, V. G.; Mazur, Y.; Salamo, G.; Lee, M. L. *Acs Nano* **2013,** 7, (6), 5017-5023.

44. Walther, C.; Blum, R. P.; Niehus, H.; Masselink, W. T.; Thamm, A. *Phys Rev B* **1999,** 60, (20), R13962-R13965.

45. Xie, Z. T.; Markus, T. Z.; Gotesman, G.; Deutsch, Z.; Oron, D.; Naaman, R. *Acs Nano* **2011,** 5, (2), 863-869.

46. Carlson, B.; Leschkies, K.; Aydil, E. S.; Zhu, X. Y. *J Phys Chem C* **2008,** 112, (22), 8419-8423.

47. Bard, A. J.; Bocarsly, A. B.; Fan, F. R. F.; Walton, E. G.; Wrighton, M. S. *J Am Chem Soc* **1980,** 102, (11), 3671-3677.

48. Rusu, P. C.; Giovannetti, G.; Weijtens, C.; Coehoorn, R.; Brocks, G. *J Phys Chem C* **2009,** 113, (23), 9974-9977.

49. Braun, S.; Salaneck, W. R.; Fahlman, M. *Adv Mater* **2009,** 21, (14-15), 1450-1472.

50. Connelly, D.; Faulkner, C.; Clifton, P. A.; Grupp, D. E. *Appl Phys Lett* **2006,** 88, (1).

51. Sobolewski, M. A.; Helms, C. R. *Appl Phys Lett* **1989,** 54, (7), 638-640.

52. Ip, A. H.; Thon, S. M.; Hoogland, S.; Voznyy, O.; Zhitomirsky, D.; Debnath, R.; Levina, L.; Rollny, L. R.; Carey, G. H.; Fischer, A.; Kemp, K. W.; Kramer, I. J.; Ning, Z. J.; Labelle, A. J.; Chou, K. W.; Amassian, A.; Sargent, E. H. *Nat Nanotechnol* **2012,** 7, (9), 577-582.

53. Klem, E. J. D.; Shukla, H.; Hinds, S.; MacNeil, D. D.; Levina, L.; Sargent, E. H. *Appl Phys Lett* **2008,** 92, (21).

54. Schmidt, M. W.; Baldridge, K. K.; Boatz, J. A.; Elbert, S. T.; Gordon, M. S.; Jensen, J. H.; Koseki, S.; Matsunaga, N.; Nguyen, K. A.; Su, S. J.; Windus, T. L.; Dupuis, M.; Montgomery, J. A. *J Comput Chem* **1993,** 14, (11), 1347-1363.

55. Soler, J. M.; Artacho, E.; Gale, J. D.; Garcia, A.; Junquera, J.; Ordejon, P.; Sanchez-Portal, D. *J Phys-Condens Mat* **2002,** 14, (11), 2745-2779.

56. Troullier, N.; Martins, J. L. *Phys Rev B* **1991,** 43, (3), 1993-2006.

57. Kleinman, L.; Bylander, D. M. *Phys Rev Lett* **1982,** 48, (20), 1425-1428.

Chapter 6

Interplay between Multiexciton Generation and Collection Efficiency at Quantum Dot-Oxide Interfaces

Harvesting multiexcitons populating semiconductor quantum dots (QDs), generated by the absorption of a single high energy photon, has been proposed as a path towards higher efficiencies in photovoltaic devices. Although multiexciton generation (MEG) efficiency has been widely interrogated in colloidal QD solutions, less focus has been placed on the physics regarding multiexciton collection (MEC) at electrodes. In this work, using optical pump THz probe spectroscopy, we investigate interfacial biexciton transfer rates and efficiency from PbS quantum sensitizing a mesoporous SnO_2 film as a function of impinging photon flux and photon excess energy. First we interrogate MEC efficiency for photon energies below the MEG threshold ($hv/E_g<2$, where biexciton regime is reached by increasing photon flux); the interfacial MEC efficiency is dictated by the kinetic competition between QD-to-oxide electron transfer and QD Auger recombination rates. Accordingly, we demonstrate that by reducing Auger rate in the QDs, by partial localization of holes in a QD molecular capping shell, allowing us boosting MEC at the QD/oxide interface. For sample's excitation allowing MEG ($hv/E_g>2$) and in the 1 hv/QD excitation regime, we find that the interfacial MEG efficiency is essentially zero. This seemingly counterintuitive result is rationalized by efficient hot electron transfer (HET) at the QD/oxide interface kinetically competing with impact ionization within the QDs, and thus greatly reducing MEG efficiency.

6.1 Introduction

In a single junction photovoltaic device, the efficiency for solar energy conversion under 1 sun is thermodynamically limited to ~33%; the so called Shockley−Queisser (SQ) limit.[1] To a great extent, this upper limit is determined to the ultrafast thermalization of highly energetic charges photo-generated by photons well exceeding material's absorption onset.[1-4] In this respect, efficiencies beyond

the SQ limit can be in principle achieved in solar cell designs where thermal losses in the absorber are circumvented, e.g. hot carrier solar cells[5] or solar cells exploiting multiexciton generation[6] (MEG, also referred as carrier multiplication). MEG is a phenomenon in which absorption of one high energy photon with energy at least twice of the semiconductor's bandgap (hv/E_g>2) is capable to produce two or more excitons[7-10] by impact ionization[11, 12]. By detailed balance arguments the theoretical limit of photo-conversion efficiency by exploiting MEG at 1 sun is ~44%.[7, 13-15] As proven in complete devices[16], sensitization of oxide electrodes by QDs could represent an appealing route for efficient interfacial dissociation of multiple excitons generated by MEG. The intimate contact between QD and oxide can in principle allow ultrafast extraction of multiple charges before exciton-exciton annihilation takes place (e.g. via Auger recombination[17-19]). Although a vast amount of experimental reports have scrutinized MEG dynamics and process efficiency as a function of photon energy and fluence in semiconducting QDs[7, 9, 20-23], to our knowledge there is only one report interrogating interfacial biexciton dissociation dynamics and multiexciton collection (MEC) efficiency at QD/oxide interfaces; albeit under excitation conditions not allowing MEG (hv/E_g<2). Although biexciton dynamics in QDs induced by the absorption of 2 photons with energies hv/E_g<2 or by MEG for photon energies hv/E_g>2 are correlated[24], an absolute estimate of multiexciton collection (MEC) efficiency at the QD/oxide interface could in principle differ in both cases. This is due to the fact that MEG efficiency is determined by the kinetic competition between impact ionization and carrier cooling within the QDs; note that both kinetic processes are absent under hv/E_g<2 excitation conditions.

Here we interrogate for the first time biexciton dissociation dynamics (transfer rates and MEC efficiency) in a sensitized system for photon energies below (hv/E_g<2) and above (hv/E_g>2) the energy excitation threshold allowing MEG. When exciting QDs with photon energies below the MEG energy onset, where the biexciton regime can be only reached under high photon flux, we find that MEC efficiency at the QD/oxide interface is dictated, in agreement with the currently available report[17], by the kinetic competition between the donor-to-acceptor-biexciton-dissociation and Auger-recombination rates within QDs. On the other hand, contrary to expectations, when exciting QDs with photon energies allowing MEG (hv/E_g>2) and in the 1hv/QD excitation regime, we find that the MEC

efficiency is essentially null. This seemingly counterintuitive result is rationalized by efficient hot electron transfer (HET) at the QD/oxide interface. By modelling the kinetic competition at the QD/oxide surface, we resolve that MEG efficiency (both amplitude and energy onset) can be dramatically affected by simple considering an ultrafast depopulation channel, e.g. HET transfer towards the oxide, kinetically competing with impact ionization within the QDs.

6.2 Methods and Materials

In this work, we analyze interfacial biexciton carrier dynamics on PbS QDs directly nucleated onto SnO_2 mesoporous matrices via successive ionic layer adsorption and reaction (SILAR) method (as the same system discussed in chapters 4, and 5). The nucleation of PbS QDs by SILAR was made in a globe box under N_2 conditions following a 3.5 SILAR cycles recipe the QDs are defined by a bandgap onset of ~0.9±0.1 eV (estimated by absorption spectrum). This growth recipe provides a good passivation scheme for the QDs by surface stoichiometry tuning, as we have shown in chapter 4. Carrier dynamics were interrogated by optical pump THz probe (OPTP) spectroscopy and the detailed working principle are given in chapter 2. In this work the samples under study were optically photoexcited by 800 nm and 400 nm laser pulses as a function of photon flux density; importantly for both excitation conditions we found null OPTP real conductivity signal on bare SnO_2 electrodes (gap ~3.5 eV). In order to prevent sample photo-oxidation during OPTP characterisation, all measurements were conducted under vacuum (~$1.4*10^{-4}$ mbar); under these conditions the OPTP signal remained constant for measuring times exceeding 12 hours.

6.3 Results and Discussions

6.3.1 Interfacial biexciton dynamics for $h\nu/E_g<2$ pump excitation: QD to oxide ET rates

Figure 6.1(A) shows OPTP data normalized to the dynamics at 1.1.ns for PbS QDs sensitizing SnO_2 as a function of 800nm pump fluence (between ~$3.87*10^{14}$ and ~$1.11*10^{16}$ photons/cm^2; these estimates are corrected for reflection and transmission losses in the samples, see the discussion in the Appendix 6.5.1). The OPTP dynamics reveal a pump induced rise of real conductivity representing electron

transfer (ET) processes taking place from the QD to the oxide. The rise is followed by a *slow* long lived decay representing back ET processes (BET) from oxide CB towards the QDs and/or oxide surface states[25]. For fluences <2.5 *10^{15} photons/cm^2 we find invariant OPTP dynamics referring to the single exciton regime (X, 1*hv*/QD excitation). A single-stretched-exponential ingrowth which amplitude is modulated by an exponential decay fits the data well; back solid line in figure 6.1(A) provides τ_{ET}^{X}= 4.2±0.2 ps and τ_{BET}^{X}= 14.7±0.3 ns respectively with β=0.58±0.1. On the other hand, for excitation fluences >2.5 *10^{15} photons/cm^2, the OPTP dynamics become fluence dependent; under these conditions the OPTP dynamics are contributed by a mixture of ET processes taking place from QDs hosting single excitons and multiexcitons respectively.[26] In this respect, the multiexciton contribution to the OPTP dynamics can be disentangled by simply subtracting low and high fluence OPTP data as shown in figure 6.1(B). Notably, the amplitude regarding multiexciton dynamics scales linearly with fluence as shown in the inset of figure 6.1(B); in addition, normalized multiexciton dynamics are invariant vs photon density as shown in figure 6.1(C). These observations allow us to conclude that, under our experimental conditions, the disentangled multiexciton contribution to the OPTP dynamics shown in figure 6.1(B-C) represent primarily the biexciton regime (XX). Black dotted line in the figure 6.1(C) represent the best fit to the XX dynamics following the same fitting protocol employed before for the X regime where β=0.58±0.1 was kept constant. Figure 6.1(D) summarizes the obtained transfer rates defining ET and BET components for 3 different PbS/SnO_2 samples in the X and XX regime respectively (K_{ET}^{X}, K_{BET}^{X} , K_{ET}^{XX}, and K_{BET}^{XX}). As evident from figure 6.1(D), both the ET and the BET rates are fasten by ~1 and ~2 orders of magnitude respectively in XX regime when compared with the X regime. Faster ET and BET rates can be tentatively rationalized by assuming an enhancement in donor-acceptor interfacial energetics and/or donor-acceptor coupling strength in the XX regime when compared with the X regime; both effects have been shown by us and others to strongly speed up donor to acceptor rates in the X regime on QD sensitized systems.[27-30,25] This simple picture could be consistent with reports showing a QD energy onset blue shift ranging from tens to few hundreds meVs as consequence of negative bi-exciton QD binding energies (see the discussion in the Appendix 6.5.2); the strength of the blue shift being dependent on QD sample composition, size[31, 32], shape[32] and strain[33].

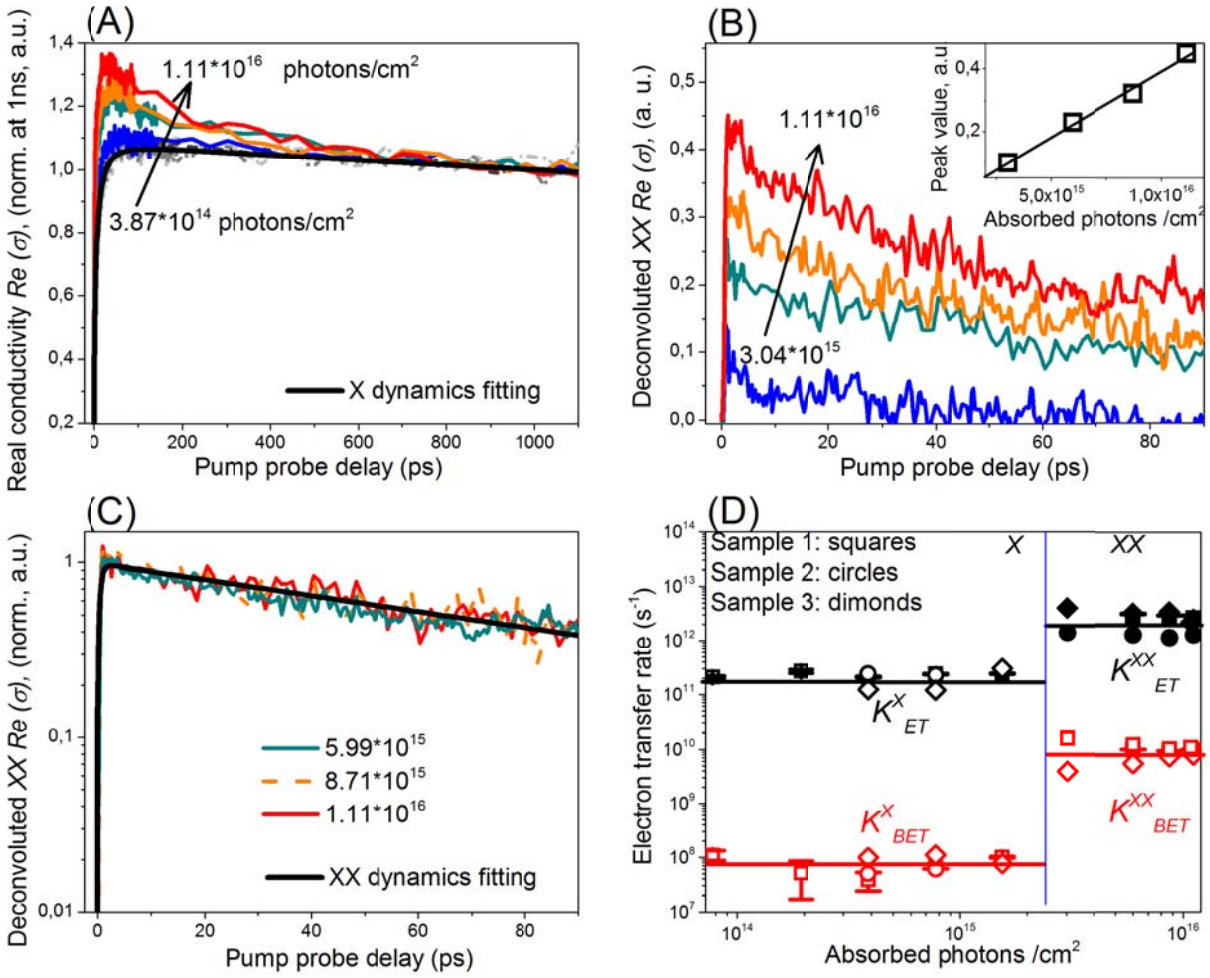

Figure 6.1 (A) OPTP electron transfer dynamics, normalized at ~1ns, as a function of 800nm pump excitation flux for PbS QDs sensitizing a SnO_2 mesoporous film; black line represent best fit following the model described in the text; (B) Disentangled biexciton (XX) OPTP dynamics. The inset shows a linear correlation between pump fluence and OPTP XX amplitude; (C) Normalized XX dynamics; black line represent best fit following the model described in the text. (D) Fluence dependent X and XX ET and BET rates for 3 different samples following same preparation and measurement protocols.

6.3.2 Interfacial biexciton dynamics for hv/E_g<2 pump excitation: QD to oxide ET efficiency

While the dynamics discussed before clearly reflect interfacial ET processes in the XX regime for *hv/E_g*<2 photon energies, more relevant for device performance is to quantify the multiexciton collection (MEC) efficiency at the QD/oxide electrode. This information can be quantified from our data as follows; for excitation densities <2.5*10^{15} photons/cm^2 we resolve a linear correlation between OPTP amplitude and photon flux (black dots in figure 6.2(A)). The obtained slope is assumed here as a reference accounting for *100%* X ET dissociation efficiency, meaning that each absorbed photon in a

QD generate 1*e* in the oxide CB (*1e/1hv;* see green line in figure 6.2(A)). We can extrapolate that slope for fluences >2.5*10^{15} photons/cm^2; this projection set the MEC upper limit efficiency at the oxide electrode in the XX regime (*2e/2hv;* see green line in figure 6.2(A)). In the XX regime, the weights of the maximum amplitudes for N_X and N_{XX} dynamics at a given fluence can be disentangled from OPTP data as discussed previously, resulting in linear dependences within the analyzed range of fluences (solid black and dotted blue lines in figure 6.2(A) for N_X and N_{XX} contributions respectively). Finally, the difference at any given photon flux between the N_{XX} contribution and the upper threshold XX efficiency (*2e/2hv*) slope accounts for Auger-related recombination losses taking place within the QDs hosting biexcitons (red area in figure 6.2(A)). In this respect, the MEC efficiency can be simply inferred by the ratio between the measured and upper limit XX contributions; or analogously by the ratio between MEC gain at the oxide electrode and Auger losses within the QDs by $\eta_{MEC}=\left(\frac{N_{XX}}{N_{XX}+N_{Aug}}\right)$.

From figure 6.2(A) we obtain a MEC efficiency of ~55 ±3% for the analyzed PbS/SnO_2 samples. This figure implies that, *on average*, QDs populated with biexcitons are only able to transfer to the oxide 1.10 ±0.06 electrons per 2 absorbed photons; or equivalently that 90 ±6% of the XX populating QDs recombine efficiently via Auger-related processes. From the latter estimates, we can infer a QD *averaged* Auger relaxation lifetime of τ_{Aug}~0.33 ps (assuming a kinetic model involving neutrally and positively charged biexcitons[17, 26], see the detailed discussion in Appendix 6.5.3). This rough estimate is consistent with the one that can be inferred from the reported linear correlation between biexciton Auger rates and nanocrystal volume (τ_{Aug}~1.5 ps).[7, 26, 34, 35]

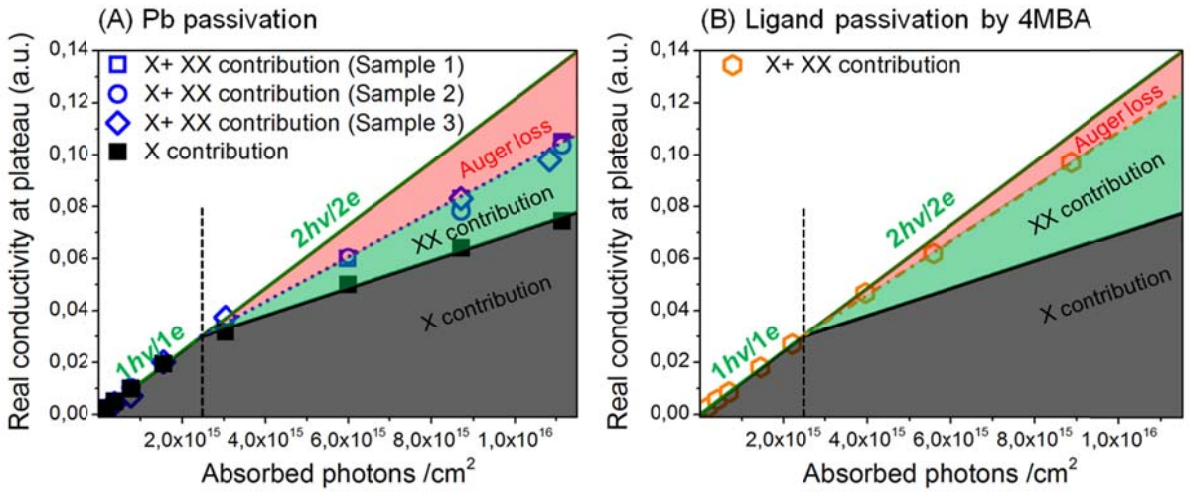

Figure 6.2 OPTP Real conductivity maximum amplitude contributions from single excitons and biexcitons populations at the oxide CB as a function of number of absorbed photons under 800nm excitation. Black dash line indicates the fluence threshold above which 2hv/QD excitation conditions are reached in the samples. Grey, green and red areas represent the contribution to OPTP signals arising from single excitons (X), biexcitons (XX) and Auger recombination losses within the QDs. Panel (A) and (B) representing PbS QD/SnO_2 sensitized samples where QDs are passivated by lead atoms or 4-mercaptobenzoic acid ligands (4-MBA) respectively.

In order to validate that a simple kinetic competition between interfacial XX transfer and Auger recombination rates within the dots determine MEC efficiency for $hv/E_g<2$ photon energies, we interrogated the impact of reduced QD Auger rate on MEC efficiency. It has been recognized in the literature that total or partial hole localization towards the QD capping shell, e.g. by exploiting core-shell type II band alignment, allows for enhancing Auger lifetimes in the QDs.[36-38] In this line, several reports demonstrated that QD hole wavefunction partially delocalizes towards the shell in thiol-based molecularly capped QDs[39-43]. Following those reports, we prepared new PbS/SnO_2 samples where passivation of the dots was achieved by 4-Mercaptobenzoic acid (4-MBA) ligands. Before analyzing MEC efficiency at the QD/oxide interface, we experimentally verified that the newer QD molecular capping treatment was not affecting ET and BET rates in the X regime, neither introducing new recombination paths competing with the previously addressed dynamics from Pb terminated dots (as discussed in figure 5.4 and figure 5.6 in chapter 5). These results allow us to establish quantitative correlations between MEC efficiencies inferred from Pb- and 4-MBA-passivated QD/SnO_2 samples. Figure 6.2(B) illustrate the weights of the maximum amplitudes for N_X and N_{XX} dynamics at a given fluence for samples passivated with 4-MBA. From this data, the inferred MEC efficiency for the 4-

MBA passivated QDs equals ~75 ±5%. This figure implies that on average 1.5 ±0.1 electrons are injected towards the oxide from QDs populated by biexcitons. The boost in interfacial MEC efficiency for 4-MBA capped QDs when compared with Pb capped QDs is consistent with the expected reduction in Auger recombination lifetime anticipated for the latter (with an estimate of τ_{Aug}(4-MBA)= 2 ps; see the detailed discussion in Appendix 6.5.3). Our results are fully consistent with the observations made by Zidek *et al.*[17], in which they have analyzed MEC efficiency in CdSe QDs sensitizing ZnO with photon energies hv/E_g<2 (biexcitons generated as a function of photon flux). In their work, they found a QD size dependent maximum MEC efficiency peaking at ~70% which was codetermined by the sequential kinetic competition between interfacial charge transfer processes and Auger dynamics in QDs.

6.3.3 Biexciton electron transfer dynamics for hv/E_g>2 photon energies

As discussed before, in order to MEG in sensitized architectures, it is mandatory to interrogate interfacial biexciton dissociation dynamics in the hv/E_g>2 regime. In order to evaluate any gain in MEC efficiency induced by MEG we analyzed OPTP interfacial dissociation dynamics for 4-MBA/QD/oxide samples as a function of 800nm and 400nm photon excitations in the 1*hv* per QD excitation regime (fluences <2.5 *10^{15}photons/cm^2). If MEG is efficient under 400nm pump excitation in our QDs (hv/E_g~3.4), a stepper slope for the OPTP real conductivity amplitude dependence with photon flux should be obtained when compared with 800nm excitation. Note here that MEG studies on isolated QDs of similar gap under similar excitation conditions revealed MEG efficiencies in the range 15-25%[35, 44, 45] (with hv/E_g ~3.1), well above our detection limit. Contrary to expectations, we find nearly identical slopes for both excitation energies, indicating that MEG efficiency in the QDs is null in our systems. A closer look to the OPTP dynamics under 800nm and 400nm allow us to rationalize this observation. In figure 6.3(B) we compare the obtained dynamics under 400nm and 800nm excitation in the 1*hv*/QD excitation regime. Although we experimentally resolve that the 400nm pump excitation fastens the ET rate, both the OPTP maximum amplitude as well as the inferred BET rates are barely affected when comparing both excitation conditions. These observations, together with the lack of MEG resolved in figure 6.3(A) can be explained by simply assuming that hot carrier extraction

is achieved in our system under 400nm excitation (hv/E_g~3.4). In simple terms, hot electron transfer induced by pump excess energy can be rationalized by an enhancement of donor-acceptor ET driving energy and coupling strength. Sub-100fs hot electron transfer lifetimes have been reported by us and other authors to be efficient from lead salt QDs towards TiO_2 electrodes[4, 46]; the resolved rise time of OPTP data for the samples analyzed here under 400nm excitation (<120 fs) is perfectly consistent with HET processes taking place at the strongly coupled PbS/SnO_2 interface. Analyzing HET is out of the scope of this paper; a detailed characterization of the nature of the process is underway and will be reported elsewhere. The most important outcome of the results shown in figure 6.3(A-B) is that ultrafast donor-acceptor ET (e.g. hot electron transfer, HET) can kinetically compete with QD impact ionization (II, triggering MEG); so ultrafast extraction of charges, a priori expected to compete only with Auger recombination in the dots, is found to be able to compete kinetically with MEG generation itself.

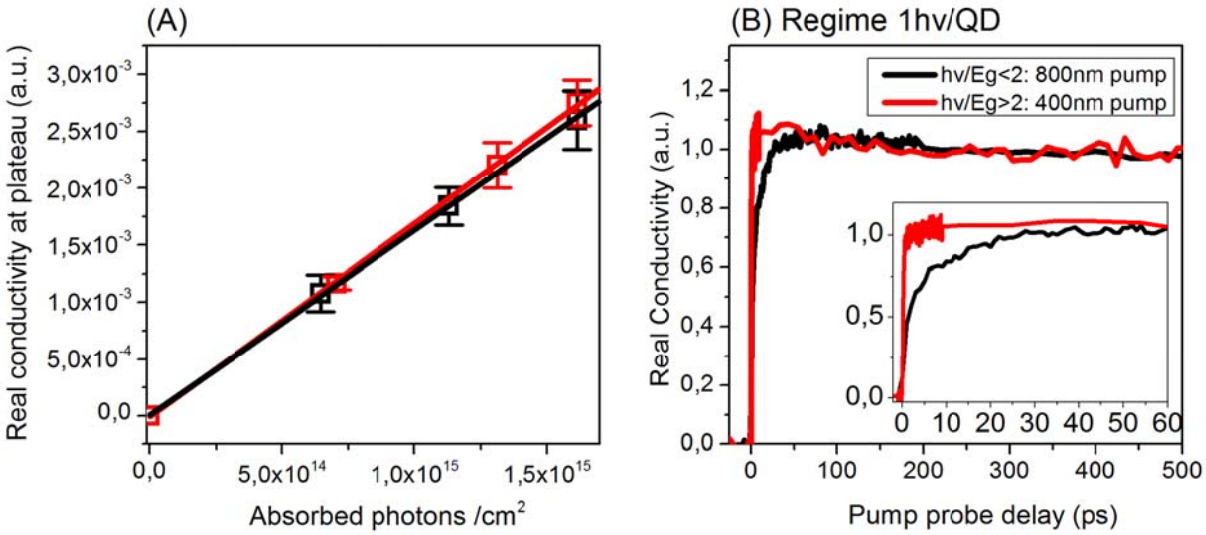

Figure 6.3 (A) Fluence dependence of the real conductivity maximum amplitude obtained for QD/SnO_2 samples excited under 800nm (black line) and 400nm (red line) pump conditions in the 1hv/QD excitation regime. (B) OPTP interfacial carrier dynamics in QD/SnO_2 samples for 800nm and 400 nm excitation (hv/Eg<2 and hv/Eg>2 respectively) in the 1hv/QD excitation regime.

In order to further verify that the results summarized in figure 6.3(A) refer uniquely to single exciton dynamics in the samples independently of hv/E_g photon energy, we performed OPTP measurements under 400nm excitation for fluences >2.5 *10^{15} photons/cm^2; then for fluences able to reach the XX regime by 2 photon absorption processes. As demonstrated in the previous section, interfacial MEC

efficiency induced by photon flux in the 2*hv*/QD regime is defined by the kinetic competition between donor-to-acceptor transfer rate and Auger-recombination rate within the QDs. In this respect, provided that photon excess energy does not change Auger recombination rate within the dots[11], HET should reveal a boost in MEC efficiency under 400nm excitation conditions. Indeed, as illustrated in figure 6.4(A), we resolve that MEC efficiency approaches unity under 400nm excitation in the 2*hv*/QD excitation regime even for samples passivated by surface stoichiometry tuning. In figure 6.4(B) we present the disentangled XX OPTP dynamics under 800nm and 400nm excitation; the overlap for XX dynamics under 400nm and 800nm excitation is fully consistent with pure bi-exciton dynamics for photon energies hv/E_g>2; supporting that MEG has a negligible contribution to MEC efficiency for the analyzed samples.

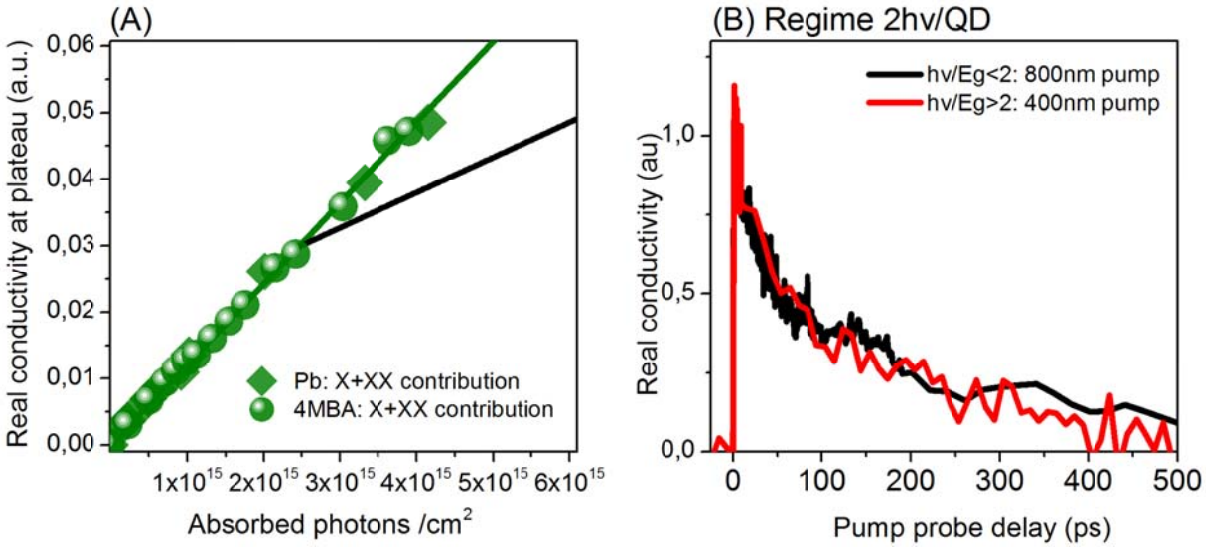

Figure 6.4 (A) Fluence dependence of the real conductivity maximum amplitude obtained for QD/SnO_2 samples excited under 400nm (green line); black dash line indicates the fluence threshold above which 2hv/QD excitation conditions are reached in the samples. (B) OPTP interfacial carrier dynamics in QD/SnO_2 samples for 800nm (black line, hv/Eg<2) and 400 nm (red line, hv/Eg>2) pump in the 2hv/QD excitation regime.

6.3.4 Modeling the kinetic competition between MEG and MEC

In order to generalize our findings, we model here the interplay between an ultrafast competing QD depopulation channel and impact ionization in ~3nm in diameter PbSe QDs; for this system MEG on isolated QDs and MEC towards a TiO_2 electrode have been reported. Theoretical works concluded that the origin of MEG relates with impact ionization, and that the upper limit efficiency of the process is

determined by the kinetic competition between hot carrier relaxation and impact ionization rates within the QDs[11, 12]. In figure 5(A) we plot the impact ionization rate (K_{II}; solid green line)[11, 47] and bulk-like intraband relaxation rate (K_{Rel}~0.83eV/ps; solid orange line)[48] as a function hv/E_g for ~3nm in diameter PbSe QDs. From these rates we can infer the upper limit for MEG efficiency as a function of photon excess energy by $\eta_{MEG}\% = \frac{K_{II}}{K_{Rel}+K_{II}}$, see black line in figure 5(B). In figure 5(A) and 5(B) we analyze the effect of adding an ultrafast process, e.g. HET, competing with impact ionization and relaxation rates on MEG efficiency ($\eta_{MEG}\% = \frac{K_{II}}{K_{Rel}+K_{II}+K_{HET}}$; dashed lines considering K_{HET}/K_{Rel} ratios from 0 to 100 in figure 5(B)). As evident from figure 5(B), increasing the K_{HET}/K_{Rel} ratio dramatically reduces MEG efficiency at a given energy and notably, even changes the energy onset where MEG efficiency becomes active. In figure 5(B), black dots represent the MEC efficiency inferred from photocurrent measurements in samples consisting on 3nm PbSe dots sensitizing a TiO_2 electrode.[16] From our modeling a HET rate of ~100fs fit the experimental data rather well; which agrees quite well with the ~50fs HET rate inferred by ultrafast spectroscopy[4, 46] for the same system. The modeling presented here fully supports our experimental observations in PbS/SnO_2 sensitized systems, and allow us to conclude that ultrafast collection of photogenerated electrons at the electrode can be detrimental for MEG efficiency.

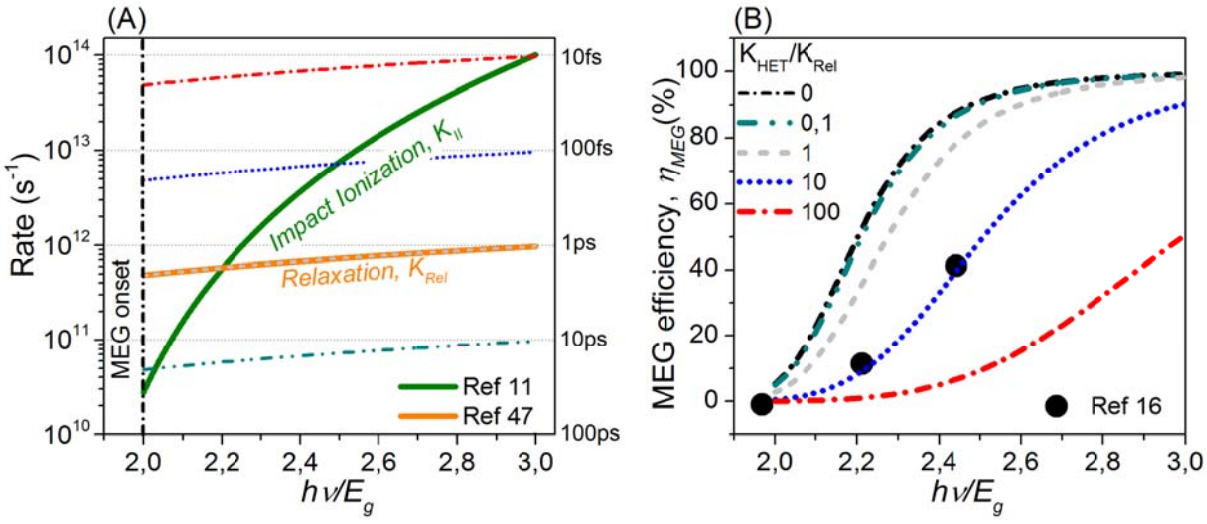

Figure 6.5 MEG generation efficiency with HET as a competing channel for 3nm PbSe QDs. (A) Impact ionization rate (K_{II}, green solid line) and electron thermalization rate (K_{Rel}, orange solid line) as a function of hv/E_g. Dashed lines represent QD-to-oxide hot electron transfer rates (K_{HET}) assuming K_{HET}/K_{Rel} ratios in the range 0-100; (B) MEG efficiency in the 2<hv/Eg<3 energy range for K_{HET}/K_{Rel} ratios in the range 0-100.

Interestingly, we believe that our simple modeling could explain the disparity on MEG efficiency estimates reported in literature for a single system by simply assuming the existence of an ultrafast trapping component competing with hot charge relaxation. Note that hot trapping in QDs has been indeed reported in lead salt dots by other authors[49, 50], and also that the speed of trapping at the QD surface is simply proportional to trap acceptor density (scaling linearly with QD surface area[25], see chapter 4). Further experimental efforts are needed to unravel whether the density of traps involved in hot charge trapping correlates with MEG efficiency as illustrated in figure 5. It is also worth mention, that the simple modeling depicted here –where K_{Rel} relates with PbSe LO multi-phonon bulk like relaxation – sets the upper threshold MEG efficiency for 3nm PbSe QDs as 76% for photon energies between 2 and 3 times the bandgap of the absorber. Aiming *square-like* MEG efficiency response in the $2<hv/E_g<3$ excitation photon range, towards maximum device photoconversion efficiency, will require exploiting QDs where bulk-like carrier thermalization rates are at least one order of magnitude slower than impact ionization rates.

6.4 Summary

To summarize, using optical pump THz probe spectroscopy we interrogate multiexciton collection (MEC) efficiency in QD sensitized system as a function of impinging photon flux, QD surface chemistry and photon excess energy. For photon energies $hv/E_g<2$, where the biexciton regime is accessible only by increasing photon flux impinging the samples, MEC efficiency is simply dictated by the kinetic competition between interfacial donor-to-acceptor ET and QD Auger-recombination rates. As a result, reducing Auger rate, e.g. by localization of holes in the outer QD shell, allows boosting the interfacial MEC efficiency in sensitized systems. For photon energies $hv/E_g>2$, where biexcitons can be readily accessible by the absorption of one high energy photon, we find that MEG efficiency is null in our system. This is correlated with ultrafast hot ET transfer processes competing efficiently against MEG generation in the QDs. Modelling allow us to conclude that that MEG efficiency estimates (both amplitude and energy onset) can be completely weighted by an ultrafast

depopulation channel (e.g. HET transfer towards the oxide) kinetically competing with impact ionization in the QDs.

6.5 Appendix

6.5.1 *Characterization of transmission and reflection losses*

The transmission and reflection losses have been characterized. The measurement geometry is shown as in the figure 6.6, in which the sample is placed inside a cryostat with the front and back window materials of quartz. The incident pump intensity $\boldsymbol{I_0}$, and transmission intensity $\boldsymbol{I_{tr}}$ are measured for each fluence used. For the reflection loss, the loss related to one reflection at the front and back windows are considered. According to the Fresnel's equations, and given the refractive index 1.5 for the quartz, one can estimate the loss $\boldsymbol{I_{ref}}$ (from the front window), and $\boldsymbol{I'_{ref}}$ (from the back window) as:

$$I_{ref}=I_0*(n_{window}-n_{air})^2/(n_{window}+n_{air})^2=I_0*(1.5-1)^2/(1.5+1)^2=0.04I_0; \quad \text{Equation 6.1}$$

$$I'_{ref}=(I_0-I_{ref}-I_{abs})*0.04=(0.96I_0-I_{abs})*0.04; \quad \text{Equation 6.2}$$

By considering the conservation of light flux in the system,

$$I_{abs}=I_0-I_{ref}-I'_{ref}-I_{tr}=I_0-0.04I_0-(0.96I_0-I_{abs})*0.04-I_{tr} \quad \text{Equation 6.3}$$

One can obtain:

$$I_{abs}=0.96I_0-1.04I_{tr}; \quad \text{Equation 6.4}$$

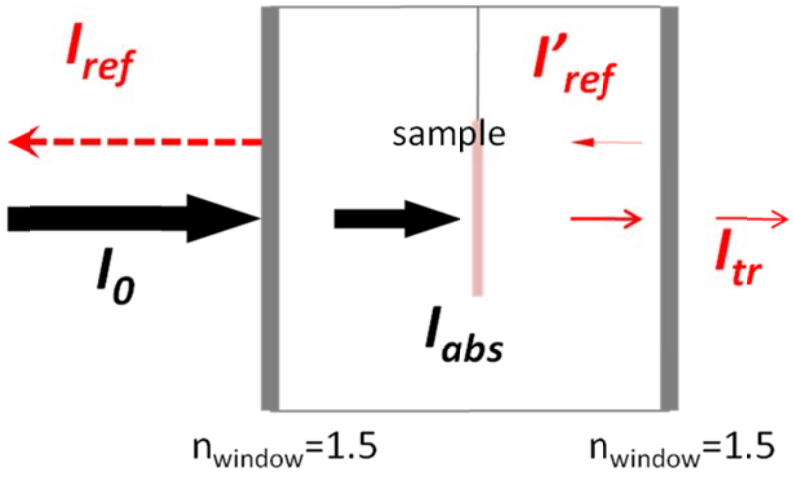

Figure 6.6 The measurement geometry for calculating the real absorption of the sample by monitoring the incoming and transmitted light intensity.

6.5.2 Discussion on XX binding energy in our system

The presence of biexcitons within a quantum dot can strongly perturb system energetics due to Coulombic interactions. The best way to describe such interaction is to introduce the biexciton binding energy δE^{XX}, which can be defined as $\delta E^{XX} = 2E^{X} - E^{XX}$; where E^{XX} and E^{X} are single and biexciton energies. In simple terms the strength and sign of the biexciton binding energy contain information about the nature of the columbic interaction within the QDs. When δE^{XX} is positive, the E^{XX} transitions move downward in energy as a consequence of exciton-exciton columbic attraction, which can be expected on systems with similar spatial distributions of electron and hole wavefunctions. On the other hand, if δE^{XX} is negative, E^{XX} transitions move upward in energy reflecting a strong columbic repulsion between the excitons, which can be promoted by distinct spatial localization within the nanocrystal of electron and hole wavefunctions, e.g. in type II core-shell dots.[33, 37, 51, 52] In order to quantitatively correlate the boost in rates resolved in figure 6.1 (D) with system energetics, one can in principle aim inferring biexciton binding energies by monitoring XX induced shifts in emission or absorption due to columbic interactions. For our sample geometry such attempt is not possible, as emission is suppressed due to the oxide electrode, absorbance is broaden and reduced due to the inhomogeneous distribution of QD sizes and strong coupling with the oxide acceptor. In this respect, a qualitative discussion describing the boost of ET in the XX regime is only doable here.

For the epitaxial grown strained PbS QDs analyze here[25], is likely that the distribution of electron and hole charge density in the bi-exciton regime is asymmetric (e.g. due to distinct nature of surface chemistry and strain at the bare PbS surface and contacted PbS/SnO_2 interface); in this respect some degree of charge localization is expected that should be linked to a broadening on QD emission onset (negative bi-exciton binding energy, δE^{XX}).

6.5.3 Estimation of Auger rate based on XX collection efficiency

In theory, the probability (*P*) of extracting 2 electrons out of an exciton states in QDs is determined by 2 consequential competitions: (1) between transferring the first electron and biexciton Auger recombination, and (2) between transferring the second electron and corresponding trion Auger recombination. That is:

$$P = P_1 * P_2 = \frac{K_{ET}^{XX}}{K_{ET}^{XX}+K_{Aug}^{XX}} * \frac{K_{ET}^{X}}{K_{ET}^{X}+K_{Aug}^{XX+}}$$, Equation 6.5,

in which, P_1 and P_2 are probability of transferring first electron and second electron out, K_{ET}^{XX}, K_{ET}^{X}, K_{Aug}^{XX} and $K_{Aug}^{XX^+}$ represent dissociation rate for first and second electron, and Auger rate in the XX and trion (XX^+) states respectively.

In equation 6.5, K_{ET}^{XX} and K_{ET}^{X} can be readily obtained by fitting ET dynamics in X and XX regime. *P* can be obtained by converting the biexciton ET^{XX} efficiency η^{XX} as:

$$P=2\,\eta^{XX}-1$$, Equation 6.6,

This relationship is based on the fact that in the biexciton states, at least one electron out of two can be extracted even if the Auger is dominant.[17] Now in equation 6.5, the only 2 unknown parameters are K_{Aug}^{XX} and $K_{Aug}^{XX^+}$. It is worth to noting that, it has been theoretically proposed[53] and experimentally demonstrated[54] that the XX Auger process can be considered as a superposition of two independent decay pathways consisting of positive- and negative-trion (X^-) channels, resulting in:

$$K_{Aug}^{XX} = (2 * K_{Aug}^{X+} + 2 * K_{Aug}^{X-})$$, Equation 6.7,

Where K_{Aug}^{X-} is the negative-trion Auger rate. By assuming a symmetric decay rate ($K_{Aug}^{X-} = K_{Aug}^{X+}$), one can get:

$$K_{Aug}^{X+} = K_{Aug}^{XX}/4 \text{ , Equation 6.8,}$$

Combined equation 6.5, 6.6, and 6.8, one can get:

$$P = \frac{K_{ET}^{XX}}{K_{ET}^{XX}+K_{Aug}^{XX}} * \frac{K_{ET}^{X}}{K_{ET}^{X}+K_{Aug}^{XX}/4} = 2\eta^{XX} - 1 \text{ , Equation 6.9,}$$

Based on equation 6.9, K_{Aug}^{XX} can be estimated with knowing the rest parameters.

References

1. Shockley, W.; Queisser, H. J. *J Appl Phys* **1961,** 32, (3), 510-&.
2. Linde, D. V. D.; Lambrich, R. *Phys Rev Lett* **1979,** 42, (16), 1090-1093.
3. Shank, C. V.; Fork, R. L.; Leheny, R. F.; Shah, J. *Phys Rev Lett* **1979,** 42, (2), 112-115.
4. Tisdale, W. A.; Williams, K. J.; Timp, B. A.; Norris, D. J.; Aydil, E. S.; Zhu, X. Y. *Science* **2010,** 328, (5985), 1543-1547.
5. Ross, R. T.; Nozik, A. J. *J Appl Phys* **1982,** 53, (5), 3813-3818.
6. Kolodinski, S.; Werner, J. H.; Wittchen, T.; Queisser, H. J. *Appl Phys Lett* **1993,** 63, (17), 2405-2407.
7. Schaller, R. D.; Klimov, V. I. *Phys Rev Lett* **2004,** 92, (18).
8. Klimov, V. I. *Annu Rev Phys Chem* **2007,** 58, 635-673.
9. Trinh, M. T.; Houtepen, A. J.; Schins, J. M.; Hanrath, T.; Piris, J.; Knulst, W.; Goossens, A. P. L. M.; Siebbeles, L. D. A. *Nano Lett* **2008,** 8, (6), 1713-1718.
10. Sandeep, C. S. S.; Ten Cate, S.; Schins, J. M.; Savenije, T. J.; Liu, Y.; Law, M.; Kinge, S.; Houtepen, A. J.; Siebbeles, L. D. A. *Nat Commun* **2013,** 4.
11. Franceschetti, A.; An, J. M.; Zunger, A. *Nano Lett* **2006,** 6, (10), 2191-2195.
12. Allan, G.; Delerue, C. *Phys Rev B* **2006,** 73, (20).
13. Werner, J. H.; Brendel, R.; Queisser, H. J. *Appl Phys Lett* **1995,** 67, (7), 1028-1030.
14. Hanna, M. C.; Nozik, A. J. *J Appl Phys* **2006,** 100, (7).
15. Klimov, V. I. *Appl Phys Lett* **2006,** 89, (12).
16. Sambur, J. B.; Novet, T.; Parkinson, B. A. *Science* **2010,** 330, (6000), 63-66.
17. Zidek, K.; Zheng, K. B.; Abdellah, M.; Lenngren, N.; Chabera, P.; Pullerits, T. *Nano Lett* **2012,** 12, (12), 6393-6399.

18. Yang, Y.; Lian, T. Q. *Coordination Chemistry Reviews* **2014,** 263, 229-238.

19. Huang, J.; Huang, Z. Q.; Yang, Y.; Zhu, H. M.; Lian, T. Q. *J Am Chem Soc* **2010,** 132, (13), 4858-4864.

20. Pijpers, J. J. H.; Hendry, E.; Milder, M. T. W.; Fanciulli, R.; Savolainen, J.; Herek, J. L.; Vanmaekelbergh, D.; Ruhman, S.; Mocatta, D.; Oron, D.; Aharoni, A.; Banin, U.; Bonn, M. *J Phys Chem C* **2008,** 112, (12), 4783-4784.

21. Nair, G.; Geyer, S. M.; Chang, L. Y.; Bawendi, M. G. *Phys Rev B* **2008,** 78, (12).

22. Nair, G.; Chang, L. Y.; Geyer, S. M.; Bawendi, M. G. *Nano Lett* **2011,** 11, (5), 2145-2151.

23. Nair, G.; Bawendi, M. G. *Phys Rev B* **2007,** 76, (8).

24. Schaller, R. D.; Klimov, V. I. *Phys Rev Lett* **2006,** 96, (9).

25. Wang, H.; Barcelo, I.; Lana-Vilarreal, T.; Gomez, R.; Bonn, M.; Canovas, E. *Nano Lett* **2014,** 14, (10), 5780-5786.

26. Zhu, H. M.; Yang, Y.; Lian, T. Q. *Accounts Chem Res* **2013,** 46, (6), 1270-1279.

27. Canovas, E.; Moll, P.; Jensen, S. A.; Gao, Y. A.; Houtepen, A. J.; Siebbeles, L. D. A.; Kinge, S.; Bonn, M. *Nano Lett* **2011,** 11, (12), 5234-5239.

28. Wang, H.; McNellis, E. R.; Kinge, S.; Bonn, M.; Canovas, E. *Nano Lett* **2013,** 13, (11), 5311-5315.

29. Robel, I.; Kuno, M.; Kamat, P. V. *J Am Chem Soc* **2007,** 129, (14), 4136-+.

30. Zidek, K.; Zheng, K. B.; Ponseca, C. S.; Messing, M. E.; Wallenberg, L. R.; Chabera, P.; Abdellah, M.; Sundstrom, V.; Pullerits, T. *J Am Chem Soc* **2012,** 134, (29), 12110-12117.

31. Lelong, P. H.; Heller, O.; Bastard, G. *Solid State Electron* **1998,** 42, (7-8), 1251-1256.

32. Schliwa, A.; Winkelnkemper, M.; Bimberg, D. *Phys Rev B* **2009,** 79, (7).

33. Ding, F.; Singh, R.; Plumhof, J. D.; Zander, T.; Krapek, V.; Chen, Y. H.; Benyoucef, M.; Zwiller, V.; Dorr, K.; Bester, G.; Rastelli, A.; Schmidt, O. G. *Phys Rev Lett* **2010,** 104, (6).

34. Robel, I.; Gresback, R.; Kortshagen, U.; Schaller, R. D.; Klimov, V. I. *Phys Rev Lett* **2009,** 102, (17), 177404.

35. Stewart, J. T.; Padilha, L. A.; Qazilbash, M. M.; Pietryga, J. M.; Midgett, A. G.; Luther, J. M.; Beard, M. C.; Nozik, A. J.; Klimov, V. I. *Nano Lett* **2012,** 12, (2), 622-628.

36. Cirloganu, C. M.; Padilha, L. A.; Lin, Q. L.; Makarov, N. S.; Velizhanin, K. A.; Luo, H. M.; Robel, I.; Pietryga, J. M.; Klimov, V. I. *Nat Commun* **2014,** 5.

37. Klimov, V. I.; Ivanov, S. A.; Nanda, J.; Achermann, M.; Bezel, I.; McGuire, J. A.; Piryatinski, A. *Nature* **2007,** 447, (7143), 441-446.

38. Nanda, J.; Ivanov, S. A.; Achermann, M.; Bezel, I.; Piryatinski, A.; Klimov, V. I. *J Phys Chem C* **2007,** 111, (42), 15382-15390.

39. Frederick, M. T.; Amin, V. A.; Swenson, N. K.; Ho, A. Y.; Weiss, E. A. *Nano Lett* **2013,** 13, (1), 287-292.

40. Wuister, S. F.; Donega, C. D.; Meijerink, A. *J Phys Chem B* **2004,** 108, (45), 17393-17397.

41. Aldana, J.; Wang, Y. A.; Peng, X. G. *J Am Chem Soc* **2001,** 123, (36), 8844-8850.

42. Knowles, K. E.; Frederick, M. T.; Tice, D. B.; Morris-Cohen, A. J.; Weiss, E. A. *J Phys Chem Lett* **2012,** 3, (1), 18-26.

43. Frederick, M. T.; Amin, V. A.; Weiss, E. A. *J Phys Chem Lett* **2013,** 4, (4), 634-640.

44. McGuire, J. A.; Sykora, M.; Joo, J.; Pietryga, J. M.; Klimov, V. I. *Nano Lett* **2010,** 10, (6), 2049-2057.

45. Ellingson, R. J.; Beard, M. C.; Johnson, J. C.; Yu, P. R.; Micic, O. I.; Nozik, A. J.; Shabaev, A.; Efros, A. L. *Nano Lett* **2005,** 5, (5), 865-871.

46. Tisdale, W. A.; Zhu, X. Y. *P Natl Acad Sci USA* **2011,** 108, (3), 965-970.

47. Luo, J. W.; Franceschetti, A.; Zunger, A. *Nano Lett* **2008,** 8, (10), 3174-3181.

48. Miaja-Avila, L.; Tritsch, J. R.; Wolcott, A.; Chan, W. L.; Nelson, C. A.; Zhu, X. Y. *Nano Lett* **2012,** 12, (3), 1588-1591.

49. Grela, M. A.; Brusa, M. A.; Colussi, A. J. *J Phys Chem B* **1999,** 103, (31), 6400-6402.

50. Kambhampati, P. *J Phys Chem C* **2011,** 115, (45), 22089-22109.

51. Piryatinski, A.; Ivanov, S. A.; Tretiak, S.; Klimov, V. I. *Nano Lett* **2007,** 7, (1), 108-115.

52. Avidan, A.; Oron, D. *Nano Lett* **2008,** 8, (8), 2384-2387.

53. Wang, L. W.; Califano, M.; Zunger, A.; Franceschetti, A. *Phys Rev Lett* **2003,** 91, (5).

54. Park, Y. S.; Bae, W. K.; Pietryga, J. M.; Klimov, V. I. *Acs Nano* **2014,** 8, (7), 7288-7296.

55. Vanmaekelbergh, D.; van Vugt, L. K.; Bakker, H. E.; Rabouw, F. T.; de Nijs, B.; van Dijk-Moes, R. J. A.; van Huis, M. A.; Baesjou, P. J.; van Blaaderen, A. *Acs Nano* **2015,** 9, (4), 3942-3950.

Chapter 7

Unity Hot Electron Transfer Quantum Yield in Quantum Dot Sensitized Mesoporous Oxides at Room Temperature

Charge thermalization processes represent one of the major efficiency losses in a solar converter. Thermal looses can in principle be circumvented if hot carrier extraction towards selective contacts is faster than intraband relaxation in the absorber (e.g. in the so called hot carrier solar cells). Previous works reported that extraction of hot electrons is feasible in QD sensitized systems, yet only at low temperature (e.g. when carrier cooling is inhibited). In chapter 6, hot electron transfer (HET) was demonstrated to be competitive with impact ionization and relaxation processes in PbS/SnO_2 samples at room temperature. Here we analyze the underling photophysics governing HET rate and efficiency in this system. We demonstrate that interfacial HET efficiency is simply determined by the kinetic competition between QD-to-oxide charge transfer and electron cooling within the QD. In this respect, HET can be tuned by increasing photon excess energy and by lowering sample's temperature. Sub-120 fs HET rates with unity quantum yield efficiency are observed for ≥1 eV excess energies of hot electrons at room temperature. Our results set the design principles for circumventing thermal losses in sensitized systems, which are promising candidates for low cost solar energy conversion schemes.

7.1 Introduction

In 1961 Shockley and Queisser established theoretically the limiting efficiency for single bandgap solar converters as ~33.5% under 1 sun illumination.[1] This upper limit is dictated ultimately by a trade-off between two competing major losses in the absorber, which are: (i) the inability to absorb photons with energy less than the absorber bandgap and (ii) the ultrafast cooling of hot carriers

generated by the absorption of photons with energies well exceeding bandgap energy[2, 3]. The latter loss mechanism accounts for a ~33% efficiency drop in optimized ~1 eV bandgap single absorber solar cells,[4] but could, in principle, be circumvented if hot carriers are extracted towards selective contacts faster than intraband relaxation in the absorber takes place (e.g. in hot carrier solar cells).[4, 5] In the quest for realizing "hot carrier solar cells"[4], much attention has been paid to prevent thermal losses in the absorbers. In bulk semiconductors, carrier cooling proceeds within picoseconds following primarily a sequential cascade of electron-phonon interactions (multiphonon relaxation).[3, 6, 7] Although initial reports suggested multiphonon relaxation processes to be inefficient in quantum dot nanocrystals near the band edges (the "phonon bottleneck effect")[8], further research demonstrated that the phonon-bottleneck effect can be bypassed by Auger-like electron-hole interactions.[9-11] Indeed decoupling of electron and hole wavefunctions in type II core-shell QDs has proven capable for making the phonon bottleneck effect active; as evident from hot electron lifetimes above nanosecond time scales.[12]

Previous reports dealt mainly with inhibiting relaxation processes near the QD bandedge, where discretization of energy levels makes the phonon-bottleneck an appealing aspect for preventing hot carrier cooling. However, for high excess energies, relaxation in QDs proceeds as in their bulk counterparts[13, 14], via multiphonon relaxation. These processes occur within ps timescales, so when aiming harvesting high energy hot carriers will require a different approach. For a system were ultrafast hot relaxation dynamics are fixed (e.g. determined by phonon-electron scattering), one could aim collecting hot carries by engineering ultrafast interfacial extraction rate towards the contacts. In this respect, strongly coupled quantum dot sensitized oxides systems in which the donor-acceptor coupling strength is enhanced by means of short conjugated bridges in between QD and oxide, as described in chapter 3, could represent a practical way for extracting hot carriers in ultrafast time scales.[15, 16] Indeed, two reports have demonstrated hot electron transfer in QD sensitized oxide systems by tuning interfacial chemistry to enhance the coupling strength between PbSe QDs and TiO_2 electrodes[17, 18], yet HET appears to be efficient only at very low temperatures (e.g. at 77 K). A recent work from us suggests that HET could indeed happen as well at room temperature for this system[19].

In all these works[17-19], HET was resolved from the $1P_e$ states of QDs to TiO_2. Still, little is known about the nature of HET for a given system as a function of photon excess energy for HET, and whether HET is possible from the bulk-like QD states at room T. Additionally, quantitative estimates of HET efficiency for a given system are lacking, and high efficiency of HET process is essential for realization of hot carrier solar cells.

In this chapter, we demonstrate by THz spectroscopy that HET efficiency with unity quantum yield can be achieved at room temperature in strongly coupled PbS QD/SnO_2 interfaces[21] (the same system that was discussed in chapters 4, 5, and 6). Furthermore, we illustrate that the quantum yield for HET efficiency is basically defined by the kinetic competition between interfacial HET rate and cooling rates within the QDs. Accordingly, increasing photon excess energy (e.g. increase the donor-acceptor coupling strength), and/or reducing carrier cooling rate by lowering system's temperature can increase the HET rate and process efficiency.

7.2 Methods and Materials

For monitoring sub-ps HET rate, we have used optical pump THz probe (OPTP) spectroscopy. PbS QDs used in this study are nucleated by following a 1 to 4 SILAR cycle recipe. The bandgap of QDs inferred from reflectance as described in chapter 4 are: 1.25±0.1 (C1), 1.0 ±0.1 (C2), 0.90±0.1 (C3) and 0.83 ±0.1eV (C4) respectively (where Cn denotes the number of SILAR cycles).

7.3 Results and Discussions

7.3.1 Efficient hot electron transfer (HET) at room temperature: the role of electron excess energy

If thermal losses in the QDs compete efficiently with interfacial ET processes in our samples, ET will take place from cold states, and one should resolve ET dynamics to be invariant on pump energy. In contrast, as shown in figure 7.1(A) (taking C3 as an example), we observed clearly distinct ET

dynamics under 800nm and 400nm excitations. For 400nm excitation the ET rate is speed up, demonstrating that electron injection from hot states is operative in the sample. For describing the ET dynamics, a simple biphasic ingrowth model with two injection channels as shown in figure 7.1(B) (assuming HET and cold electron transfer (CET)) is proposed, and the best fits are shown in figure 7.1(A). Based on this model, both HET rate and efficiency can be obtained readily from the fittings. Regarding to the HET efficiency, while for 800nm excitation the ET dynamics are clearly bi-phasic (with HET rate ~ 1ps and CET rate ~10 ps) with nearly equal weight between HET and CET; in the case of 400 nm pump, HET with <120 fs rate (limited by instrumental response) is the only active injection channel, implying unity HET quantum yields at room T. Note that the obtained HET rate and efficiency are consistent with the reported relaxation rates in lead salt QDs (near the bandgap threshold, $1P_e$-$1S_e$, 0.5 to >2 ps[9-11, 22] and well above it, where bulk-like PbS multi-phonon relaxation dynamics has been reported to be 0.83 eV/ps)[14]. For 400nm pump, the hot electron excess energy is >1 eV, and then HET rate is expected to compete with bulk relaxation. The unity quantum yield agrees well then with the obtained <120 fs rate and the 0.83 eV/ps cooling rate. For 800nm pump, the HET rate ~1 ps resolved in figure 7.1(A) will be consistent with a ~50% HET efficiency.

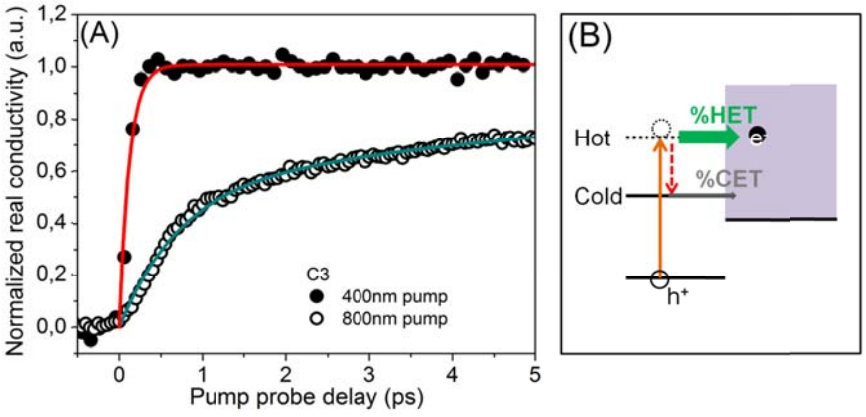

Figure 7.1 (A) Demonstration of hot electron transfer dynamics by comparing ET dynamics for 800nm pump and 400nm pump for 0.90±0.1eV QDs directly nucleated onto SnO2 films; (B) Schematic presentation of interfacial HET and cold electron transfer (CET); the red dashed arrow represent carrier cooling in the QD.

Following these results we analyzed the dependence of photon excess energy on HET rates and efficiency by changing QD size. A change in QD size will affect the excess energy for hot electrons photoinduced in the samples and then should affect HET rate and efficiency. Because of the similar

effective masses for electrons and holes in PbS [14, 23], t, and the excess energy of hot carriers are equally distributed between electrons and holes[14]; therefore the excess energy of hot electrons can be defined as: $E_{ex}=(h\nu-E_g)/2$. As the QD bandgaps are narrowing (for SILAR recipes, resulting in the reduced excess energy for a given pump energy. In principle, with increasing of E_{ex} of hot carriers, both cooling dynamics and coupling strength in the system can be modified. For hot carrier with large E_{ex}, carrier cooling follows bulk-like relaxation[13], because of much denser density of states in high lying states in contrast to discrete energy spectrum near the band edge. On the other hand, the coupling strength for electrons with high E_{ex} thus HET rate is expecting to be enhanced, owing to a large wavefunction linkage into oxide phase from higher excited states.[18] Indeed, as shown in figure 7.2(A) by increasing QD size and hence reducing QD bandgap the HET rate is increased in proportion with the photon excitation excess energy, reaching the time resolution of our set-up ~120-150 fs for photon excitations >1 eV above the LUMO QD level. Accordingly, the HET efficiency increases with E_{ex} and reaches a ~100% QY (with E_{ex} ~1 eV).

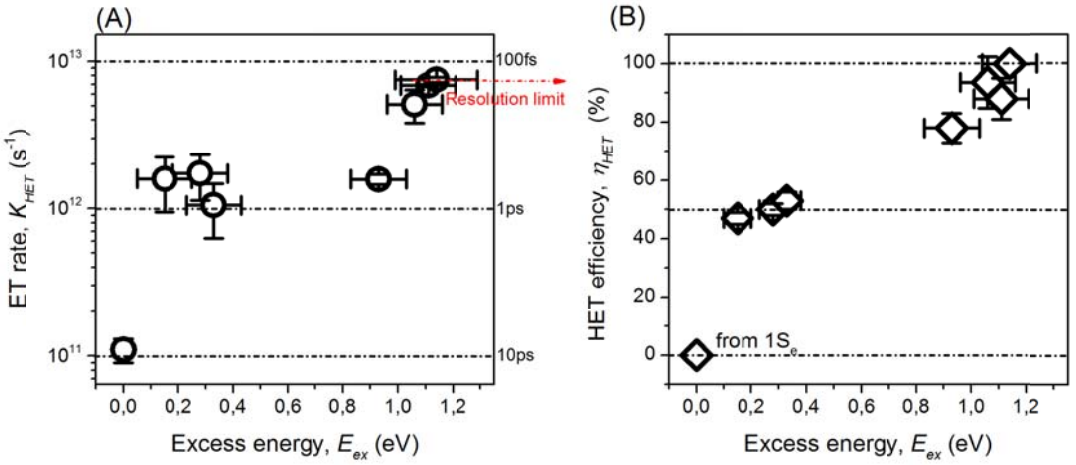

Figure 7.2 (A) Excess energy dependent HET rate extracted from the model described in the paper; (B) Excess energy dependent HET efficiency. The error is estimated from measurements based on 3-8 different samples.

7.3.2 Hot electron transfer: the effect of temperature (or the cooling rate)

By decreasing temperature (T), the cooling rate in QDs slows down as a consequence of less efficient electron-phonon interactions,[17, 18] while excess excitation energy is expected to be fixed (provided that QD bandgap is not affected by T for our QD sizes). [23, 24] Consequently, HET rate and efficiency is anticipated to increase as the temperature of the system is decreased. In line with our expectation, as

shown in figure 7.3 (A) the ultrafast rate and amplitude for HET dynamics is increased by lowering T. The results are summarized in figure 7.3(B) and (C); where the presented parameters were inferred by following the same fitting protocol as described before. As evident from the plots, a reduction of temperature (affecting electron cooling rate) boost HET efficiency in the systems.

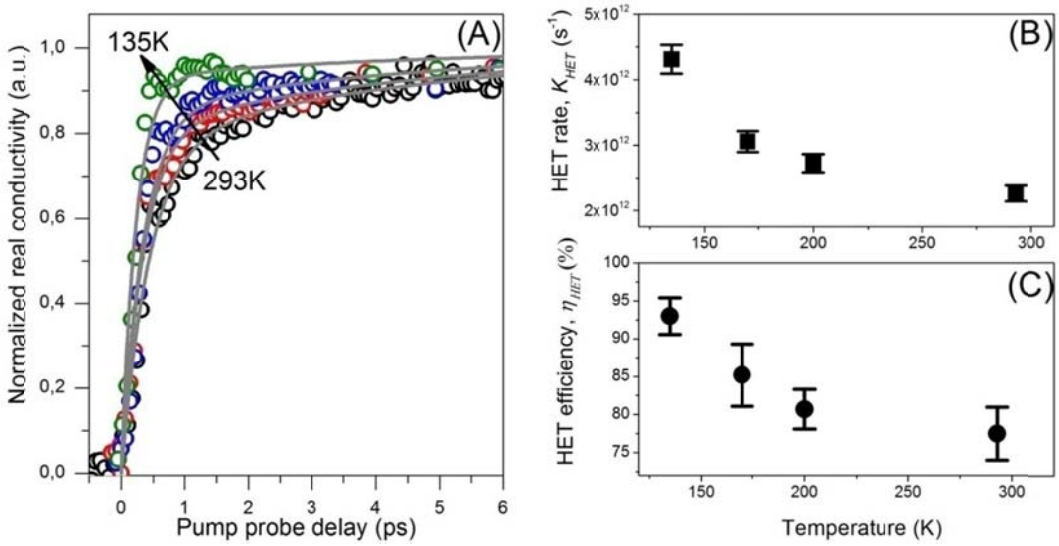

Figure 7.3 (A) Temperature (T) dependent HET dynamics (from room T to 135K). The grey lines are biphasic fittings described in the text; (B) extracted HET rate at different T, and (C) corresponding efficiency.

7.4 Summary

To summarize, we demonstrate that efficient hot electron extraction at room temperature can be achieved in SILAR grown bridgeless QD sensitized SnO_2 systems. By increasing the excess energy of hot electrons in QDs, coupling strength between hot states and oxide CB is enhanced leading to sub-120 fs HET with unity quantum yield for E_{ex} above 1eV in our samples. Additionally, lowering T can substantially reduce the thermalization rate, resulting in a favorable competition between interfacial donor to acceptor HET and cooling within the dots.

Reference

1. Shockley, W.; Queisser, H. J. *J Appl Phys* **1961,** 32, (3), 510-&.

2. Linde, D. V. D.; Lambrich, R. *Phys Rev Lett* **1979,** 42, (16), 1090-1093.

3. Shah, J.; Pinczuk, A.; Gossard, A. C.; Wiegmann, W. *Phys Rev Lett* **1985,** 54, (18), 2045-2048.

4. Ross, R. T.; Nozik, A. J. *J Appl Phys* **1982,** 53, (5), 3813-3818.

5. Wurfel, P. *Sol Energ Mat Sol C* **1997,** 46, (1), 43-52.

6. Rossi, F.; Kuhn, T. *Rev Mod Phys* **2002,** 74, (3), 895-950.

7. Othonos, A. *J Appl Phys* **1998,** 83, (4), 1789-1830.

8. Nozik, A. J. *Physica E* **2002,** 14, (1-2), 115-120.

9. Hendry, E.; Koeberg, M.; Wang, F.; Zhang, H.; Donega, C. D.; Vanmaekelbergh, D.; Bonn, M. *Phys Rev Lett* **2006,** 96, (5).

10. Klimov, V. I.; McBranch, D. W. *Phys Rev Lett* **1998,** 80, (18), 4028-4031.

11. Guyot-Sionnest, P.; Shim, M.; Matranga, C.; Hines, M. *Phys Rev B* **1999,** 60, (4), R2181-R2184.

12. Pandey, A.; Guyot-Sionnest, P. *Science* **2008,** 322, (5903), 929-932.

13. Cho, B.; Peters, W. K.; Hill, R. J.; Courtney, T. L.; Jonas, D. M. *Nano Lett* **2010,** 10, (7), 2498-2505.

14. Miaja-Avila, L.; Tritsch, J. R.; Wolcott, A.; Chan, W. L.; Nelson, C. A.; Zhu, X. Y. *Nano Lett* **2012,** 12, (3), 1588-1591.

15. Yang, Y.; Rodriguez-Cordoba, W.; Xiang, X.; Lian, T. Q. *Nano Lett* **2012,** 12, (1), 303-309.

16. Wang, H.; McNellis, E. R.; Kinge, S.; Bonn, M.; Canovas, E. *Nano Lett* **2013,** 13, (11), 5311-5315.

17. Tisdale, W. A.; Williams, K. J.; Timp, B. A.; Norris, D. J.; Aydil, E. S.; Zhu, X. Y. *Science* **2010,** 328, (5985), 1543-1547.

18. Tisdale, W. A.; Zhu, X. Y. *P Natl Acad Sci USA* **2011,** 108, (3), 965-970.

19. Cánovas, E.; Wang, H.; Karakus, M.; Bonn, M. *Chem Phys*.

20. Anderson, N. A.; Lian, T. Q. *Annu Rev Phys Chem* **2005,** 56, 491-519.

21. Wang, J.; Mora-Sero, I.; Pan, Z. X.; Zhao, K.; Zhang, H.; Feng, Y. Y.; Yang, G.; Zhong, X. H.; Bisquert, J. *J Am Chem Soc* **2013,** 135, (42), 15913-15922.

22. El-Ballouli, A. O.; Alarousu, E.; Usman, A.; Pan, J.; Bakr, O. M.; Mohammed, O. F. *Acs Photonics* **2014,** 1, (3), 285-292.

23. Wise, F. W. *Accounts Chem Res* **2000,** 33, (11), 773-780.

24. Dey, P.; Paul, J.; Bylsma, J.; Karaiskaj, D.; Luther, J. M.; Beard, M. C.; Romero, A. H. *Solid State Commun* **2013,** 165, 49-54.

Chapter 8

Summary and Conclusions

In spite of their potential, photovoltaics represent only a tiny fraction of current global energy sources nowadays. For turning this scenario around, it is necessary to achieve low cost-high efficiency solutions for the direct conversion of sunlight into electricity. For overcoming the high production costs of traditional solar cells based on silicon, new solar cell concepts and protocols employing e.g. cheap, abundant and solution-processable materials as light absorbers have been developed in the recent years.

Within this scenario, quantum dot-sensitized solar cells (QDSSCs) represent a promising low-cost photovoltaic technology that has demonstrated a sharp rise in efficiency performance in the past decade. Despite these efforts, the <10% efficiency of current QDSSCs designs is still too low to be competitive with established technologies. While the low cost is attractive, further research efforts need to focus on photoconversion efficiency improvement: a mandatory step for potential commercialization of QDSSCs in the future. To this end, the work included in this thesis was dedicated to understand and to potentially overcome the fundamental constraints limiting QDSSC device efficiencies, with a particular focus on analyzing carrier dynamics at the sensitized interfaces by THz spectroscopy. The operation of a QDSSC is complex: it relies on the kinetic competition between charge transfer and trapping processes across hybrid interfaces, as well as on transport and trapping dynamics taking place at the electrodes. In this thesis, we focused primarily on unveiling the nature and tuning of interfacial electron transfer (ET) processes from the quantum dot (QD) sensitizer towards the mesoporous oxide electrode. The results discussed and summarized in this thesis revealed new pathways in order to boost efficiencies of QDSSCs by targeting: (i) improvements in device's open circuit voltages (V_{OC}) by reducing thermal energy losses at QD/oxide interfaces, and (ii) improvements in short circuit currents (J_{SC}) by suppressing trapping processes in QD/oxide electrodes.

8.1 Reducing thermal energy losses at QD/oxide electrodes

When ET takes place from the lowest unoccupied molecular orbital (LUMO) of QDs towards the oxide conduction band (CB), an associated thermal loss at the interface needs to be considered for estimating the solar cell's maximum efficiency. The thermal energy loss at the electrode is linked to the need of paying a certain amount of energy (commonly referred to ET driving excess energy, ΔG)

for dissociating excitons at the interface. A fundamental question arises here: what is the minimum energy offset required to transfer electrons from the QD to the electrode? Aiming to reduce the value of donor-acceptor ΔG while keeping the interfacial ET rate still fast, we have interrogated the role of the donor-acceptor coupling strength and QD surface dipole moment on ET dynamics in chapters 3 and 5.

In chapter 3 we demonstrated that for a fixed value of ΔG, ET rates from QD donor to oxide acceptor can be fastened by systematically shortening the length of molecular linkers between them. These results are rationalized by assuming a simple model of a tunneling process taking place from QDs to oxide: the molecular linker acts simply as a resistor towards current flow between QDs and oxides, and the QD/oxide coupling strength exponentially decays with respect to donor-acceptor distance. Furthermore, we demonstrated that for a fixed donor-acceptor distance defined by the molecular bridge, unsaturated molecular bridges imposed a smaller tunneling barrier height than those based on saturated hydrocarbons (e.g. when comparing SH-$[C_6H_4]_n$-COOH and SH-$[CH_2]_n$-COOH bridges. Remarkably, we found that the decay factors of the tunneling processes obtained from the ET rates were in quantitative agreement with reported values from conductance measurements through single molecules and self-assembled monolayers. Achieving ultrafast ET processes by enhancing donor-bridge-acceptor coupling strength through interfacial chemistry engineering can release constrain related with aiming reduced ΔG losses in QDSSC designs.

In chapter 5 the impact of QD dipolar molecular capping as a mean to tune interfacial energetics (ΔG) was investigated. We found that, Fermi level pinning effects at the QD/oxide interface can completely preclude the tuning of the interfacial energetics by QD molecular capping. In this respect, we further demonstrated that tunability of ΔG is enabled after inserting an insulating layer in between QD/donor and oxide acceptor phases. These results offer new design principles for reducing thermal losses at QD/oxide interfaces, and open the path for improved photoconversion efficiencies on QD-sensitized systems beyond the thermal losses associated with ΔG.

Additionally, an ambitious strategy for boosting photoconversion efficiencies beyond the Shockley–Queisser limit relies on preventing thermal losses at the absorbers: e.g. those associated with cooling of hot carrier after the absorption of photons with energies above the bandgap. In this thesis we have analyzed two approaches for circumventing thermal losses within QDs: multiexciton generation and collection, and hot carrier extraction at oxide interfaces.

Multiexciton generation (MEG) is a process where a high energy photon ($hv>2E_g$) can produce at least two excitons. During the last decades, most of the research focused on MEG was devoted to investigate the underlying physics of the processes in isolated QD systems. For implementing MEG in real devices, multiexciton collection (MEC) at electrodes is critical but has not been extensively

studied yet. In chapter 6 we studied MEC rates and efficiencies in QD/oxide electrodes as a function of QD photon excess energy. Firstly we have interrogated MEC efficiency for photon energies below the MEG threshold (hv/E_g<2, where biexciton regime is reached by increasing photon flux); the interfacial MEC efficiency is found to determine by the kinetic competition between QD-to-oxide electron transfer and QD Auger recombination rates. For excitations allowing MEG (hv>$2E_g$) in QDs, the MEG efficiency in the 1*hv*/QD excitation regime was essentially zero, while collection efficiency of biexciton generated in the 2*hv*/QD regime can reach nearly 100%. This seemingly counterintuitive result was rationalized by efficient hot electron transfer (HET) at the QD/oxide interface kinetically competing with impact ionization (II): a key step for efficient MEG efficiency in the QDs. Our results provided new fundamental insights into exploiting MEG effects in nanostructured systems efficiently.

In chapter 7 we analyzed the photophysics of hot electron transfer (HET) processes taking place in QD/oxide electrodes. Although HET was demonstrated in chapter 6 to reduce the MEG efficiency, it could however be quite relevant for hot carrier solar cell designs. In this chapter we demonstrated that by enhancing the donor-acceptor coupling by increasing the photon pump excess energy, HET efficiency can reach unity quantum efficiency yield at room temperature. On the other hand, we demonstrated that samples displaying less efficient HET can reach unity quantum efficiency yield as well by reducing the sample temperature and thereby inhibiting thermal losses in the QDs. These results rationalize the underlying physics regarding HET at QD/oxide electrodes, offering new avenues to exploit efficient extraction of hot carriers in sensitized protocols.

8.2 Boosting J_{SC} by preventing surface trapping at QD/oxide electrodes

In chapter 4 and a section of chapter 5 we discussed our attempts to prevent recombination losses in QD/oxide architectures by different passivation schemes (e.g. inorganic or organic in nature). These engineering efforts are crucial for boosting photocurrents in solar cell converters.

In chapter 4 we demonstrated that QDs can be passivated "atomically" by tuning surface stoichiometry. This can be achieved by the mean of successive ionic layer adsorption and reaction (SILAR), which allows controlling whether surfaces are terminated with cations or anions. Furthermore, we found that the boost in efficiency of a QD following a passivation treatment increased linearly with QD surface area (correlating with the number of surface trap acceptors). Notably, we established qualitative correlations between the enhanced ET efficiency in QD/oxide interfaces by stoichiometry control inferred by ultrafast THz spectroscopy and the short circuit (J_{SC}) enhancement in complete QDSSCs devices. In chapter 5 the passivation of QD surfaces by organic molecules was correlated with the one inferred by stoichiometry, obtaining a similar passivation efficiency for both treatments for a given QD size. Fully inorganic or organic passivat**ed** QD schemes

are thus equally suitable for boosting QDSSCs performances; selecting among them can allow improved flexibility on the design for future sensitized cells.

While passivation of QD surfaces is vital for device performance, preventing recombination processes between the electron and hole contacts is also critical. In a collaborative effort with partners from Spain and China on exploiting TiO_2 surface capping by ZnS/SiO_2 (J. Am. Chem. Soc., 2015, 137 (16), pp 5602–5609), we demonstrated by THz spectroscopy that back electron transfer recombination was inhibited in proportion to the TiO_2 over-coating treatment. By following this approach, ~8.2% world record efficiency QD sensitized solar cells were developed.

In conclusion, provided that recombination losses can be in principle circumvented by rational engineering of interfaces, in order to increase the efficiency of QDSSCs one should target a reduction of thermal energy losses at electrodes. In this respect, several novel strategies have been addressed in this thesis, e.g. reducing interfacial donor-acceptor energetics by QD dipolar capping, multiexciton collection and interfacial extraction of hot carriers. From a kinetic point of view, all of these results share a common aspect – boosting QD/oxide coupling strength represents a key aspect towards high performing devices.

List of publications

This thesis is based on the following publications and manuscripts (# denotes equal contributions):

(1) Tuning Electron Transfer Rates through Molecular Bridges in Quantum Dot Sensitized Oxides,

Hai Wang, Erik R. McNellis, Sachin Kinge, Mischa Bonn and Enrique Cánovas, , ***Nano Letters***, 2013, 13 (11), 5311–5315; (Chapter3)

(2) Interplay between Structure, Stoichiometry, and Electron Transfer Dynamics in SILAR-based Quantum Dot-Sensitized Oxides,

Hai Wang#, Irene Barceló#, Erik McNellis, Teresa Lana-Villarreal, Robertó Gomez, Mischa Bonn and Enrique Cánovas, , ***Nano Letters,*** 2014, 14 (10), pp 5780–5786; (Chapter 4)

(3) Fermi Level Pinning at QD Sensitized Oxide Interfaces Precludes Tuning of Donor-Acceptor Energetics by QD Dipolar Molecular Capping,

Hai Wang, Yuki Nagata, Mischa Bonn and Enrique Cánovas, *in preparation;* (Chapter 5)

(4) Interplay between Multiexciton Generation and Collection Efficiency at Quantum Dot-Oxide Interfaces,

Hai Wang, Mischa Bonn and Enrique Cánovas, *in preparation;* (Chapter 6)

(5) Unity Hot Electron Transfer Yield in Quantum Dot Sensitized Oxides at Room Temperature

Hai Wang, Ivan Infante, Mischa Bonn and Enrique Cánovas, *in preparation;* (Chapter 7)

Other publications

(6) On the Origin of Ferromagnetism in CeO2 Nanocubes,

MY Ge, H Wang, EZ Liu, JF Liu, JZ Jiang, YK Li, ZA Xu, HY Li, ***Applied Physics Letters*** 93(2008), 062505;

(7) Surface Magnetism in Amine-Capped ZnO Nanoparticles,

J F Liu, En-Zuo Liu, H. Wang, N H Su, J Qi and J Z Jiang, ***Nanotechnology*** 20 (2009), 165702;

(8) Anomalous compressive Behavior in CeO2 Nanocubes under High Pressure,

M.Y. Ge, Y.Z. Fang, H. Wang, and J.Z. Jiang, ***New Journal of Physics*** 10 (2008), 123016;

(9) Electrochemical Charging of CdSe Quantum Dot Films: Dependence on Void Size and Counterion Proximity,

S. Boehme#, H. Wang#, L. Siebbeles, D. Vanmaekelbergh, and A. Houtepen, ***ACS Nano***, 2013, 7 (3), 2500–2508 ;

(10) Boosting Power Conversion Efficiencies of Quantum-Dot-Sensitized Solar Cells Beyond 8% by Recombination Control,

Ke Zhao, Zhenxiao Pan, Iván Mora-Seró, Enrique Cánovas, Hai Wang, Ya Song, Xueqing Gong, Jin Wang, Mischa Bonn, Juan Bisquert, and Xinhua Zhong, ***Journal of the American Chemical Society***, 2015, 137 (16), 5602–5609;

(11) Hot Electron Transfer from PbSe Quantum Dots Molecularly Bridged to Mesoporous Tin and Titanium Oxide Films,

Enrique Cánovas, Hai Wang, Melike Karakus and Mischa Bonn, ***Chemical Physics (invited)***, 2016 471, 54–58

(12) Enhanced kinetics of hole transfer and electrocatalysis during photocatalytic oxygen evolution by cocatalyst tuning,

Ela Nurlaela, Hai Wang, Tatsuya Shinagawa, Sean Flanagan, Samy Ould-Chikh, Muhammad Qureshi, Zoltan Mics, Philippe Sautet, Tangui Le Bahers, Enrique Canovas, Mischa Bonn, Kazuhiro Takanabe, ***ACS Catalysis***, 2016, 6 (7), pp 4117–4126

(13) Sulfur-Enriched Conjugated Polymer Nanosheet Derived Sulfur and Nitrogen co-Doped Porous Carbon Nanosheets as Electrocatalysts for Oxygen Reduction Reaction and Zinc–Air Battery,

Yuezeng Su, Zhaoquan Yao, Fan Zhang, Hai Wang, Zoltan Mics, Enrique Cánovas, Mischa Bonn, Xiaodong Zhuang, Xinliang Feng, ***Advanced Functional Materials***, 2016, accepted.

Acknowledgments

Yes, I know! Everyone starts reading a thesis from the acknowledgments! ☺ And I can also understand this part is probably the most, if not the only interesting section for you! For me, the last four years in Mainz have been a wonderful time, partially for my work in science but more importantly for my personal development. I will take this chance, to thank whoever has contributed to make me a more open-minded, happier and better person than I was: a hug to you who have chosen to be my friend, to show me the greatness of friendship; a big smile to you who have demonstrated me the power of optimism; a "hai-5" to you who make me open-minded, to appreciate and respect the differences, and to be happy with who I am; a bow to you who has given me wise suggestions about important issues in my life and work; and many thanks to you who have introduced me in great detail about European life and culture (still much to learn, such as to be "Europeanly" humorous): especially to those who have brought different tasty cheeses from different places, and kept me choppy and may eventually "trap" me here.

When I think of individuals, I realize this is going to a long list. Of course , you deserve to be on top of the list! Thanks a lot for all scientific discussions, suggestions, support and help for paper writing, talk preparations and finishing my thesis. My naive attempts to prove "my project leader is almost definitely wrong" (although often failed), have actually pushed myself to be more strong and confident, and to think and to work independently - thank you for the freedom you have given to me. As a person with the idea of "more-or-less-OK is totally-OK" before joining the group, you have trained me to be more critical in science. , thanks for giving me the chance to work in such an outstanding and also social group. Thank you for your suggestions about how to focus on my work and how to develop myself in science. Also thank you for supporting me to join the MAINZ graduate school, from which I have benefited a lot in my scientific development. From time to time, your optimism just came in time for charging me up again during group meetings. You have proven to me that, a great scientist can be also a great person☺!

For colleagues who have directly involved in my projects: thank you all for your contributions to this thesis. , I have learnt much chemistry from you: you were here only three months, but laid a solid platform for me to study many interesting physics for more than three years. I wish you the best for your future carrier, in academia or in industry. , thanks a lot for your suggestions and initial idea for our linker paper. I appreciate your comments and discussions during group meetings. , without your calculations, we won't understand hot electron transfer as deep as we do now. I hope we can cook a nice paper out of it together in the coming months. , thank you for your input and discussion on the dipole paper. , I benefited from the discussion with you

regarding the common mistakes made by Asian PhD students in scientific writing, and encouragement on proceeding with a scientific carrier, and many help for reading the manuscripts. , thank you for sending us quantum dots. For me, you are the one who opened me the door to science: it was a very special time for me to work with you in Delft. I have learnt a lot from you and : how to collaborate with other people in science, scientifically and socially.

In our nanostructured photovoltaics group, I was lucky to work with many nice colleagues with different backgrounds over the last four years. , thank you for sharing with me very honestly, how you thought about my "pushing" working behavior during our conference trip to Lausanne. That has helped me much for being more constructively helpful during collaborations and discussions. I wish you my best luck for finishing your thesis smoothly, in time and a bright future after your PhD. , I have learnt many things about the THz setup from you. Thank you for your patience, and help for realigning/maintaining the setup. I hope you have a good time in NREL. , thanks a lot for your many comments on my projects from the chemistry point of view: this knowledge is necessary in my project. I hope you find a good position in science/industry that you like now/or soon. , all my lovely QDs will be transferred to you: I wish you all the best in the coming years, and a fruitful PhD time in Mainz.

, I don't know how many thaa------aaanks I have to say out loudly for showing my acknowledgement for what you have done for me: I am sure every one of us feels the same. Besides all the help (work related or personal matters) I enjoy a lot the little chats from time to time in your office. I would like to thank for reading my thesis and giving comments and feedback. I would like to acknowledge the great financial and organizational support from the MAINZ graduate school.

When I think about my office mates, I am wearing a big smile in my face: what a great bunch of funny, friendly, social people you are. Ciao, , come stai? Man, you are almost as "old" as me in the group! Thank you my friend: yes, you are the one who made me want to be an Italian - although if you think about topics like "food, Mama, social networking, and emotions", there is not much difference between a Chinese and an Italian anyway! ☺ I enjoy our time together talking nonsense, or sharing personal feelings or little complains - it does not matter where we are: ufficio, caffè, o ristorante. Thanks for showing us around your hometown and introducing your family to us, helping me to choose a perfect suit for my big day etc. I wish everything will go well with finishing your thesis and defending it 434 km away. , "thank you" for teasing us around and keep me laughing. Also I do appreciate many "seems-small" things you have done for the office when the heads of PhD students were fully occupied by science (it is not only your responsibility, but you are always so responsible): installing the printer, get new paper from supermarket etc. Dank je wel voor het leren van een paar "heel nuttige" woorden (bijvoorbeeld luie aap). I still have to laugh when I think

about your quiz result on "how Dutch you are". I am not leaving yet, but I will definitely think of you when someone says “A~~nyway”. “Good morning”, [redacted]: I like your sense of humor and relaxing attitude at work, which makes our office a place very living and social. I hope everything goes well with your projects and you can finish your PhD smoothly. [redacted], thank you for being such a nice office mate who is willing to listen but also share stories. Being an organized person, it must be difficult to sit next to a messy desk full of paper☺.

For the [redacted]: I will mention all of you (or us) as an group rather than individuals here, as it is going to be a very long list and I will have a big chance to miss someone’s name that I don’t intend to. One thing is for sure, that I have enjoyed every single day during my stay in this group, because of you, you and you, who, who and who are nice and social from different cultures: thanks for bringing a cake for certain reasons, or voting for gently asking/pushing someone to bring one for no reasons; thanks for giving us a nice photo book as our wedding gift: I have never seen so many funny and ridiculous pictures of mine (but I love them ☺); thanks for the nice time having a drink in Baron or at festivals. I have to mention the Christmas show, one of the highlights in my PhD time: it was a great success, and more importantly, I felt really proud to be one of the group, and I got to know some of you much better through it. Thanks again and I wish you all the best for the future.

Friends out of lab: [redacted], I enjoyed all the great time we have spent together! Thank you for your support over the last 6 years. You are my “living legend” full of life wisdom, positive energy and humor. How lucky I am to know you, to become a great friend with you (with 60 years age difference), and how much I have learnt from you! Whenever I feel something is difficult and try to find *smoesjes*, your words like “tomorrow is another day”, “so what”, “just do it” appear in my mind: if like you, grandma, who still keeps herself up-to-date, learns new things at age 91 (I guess you are most likely the oldest computer user in NL?), no one has excuses to stop learning. [redacted], thank you for all the support over years. I wish you happy and peaceful, and enjoy your life every day. [redacted], you opened an European window for me. Starting from being curious about culture differences, I have asked, naively many questions to you when we were master students together in Delft, and you were always so patient to tell me the reasons behind the differences. You are always so nice, social, open, smart and positive, and I felt so lucky, and sometimes even proud to have a friend like you. [redacted]: you don’t have a brother, I don’t have a brother neither - we are brothers of each other ☺. It is just so natural to talk about/share almost everything with you and Claudia. I have learned a lot from you, to be nice (and nicer) and moderate.

感谢所有曾经支持过, 关心过我的朋友. 豆子, 不管隔着有多远,或者一时忙碌没有联系, 我们之间的兄弟情谊都没有变化－遇上你这样一个“坏人”, 一辈子都毁了; 赛, 谢谢你这些年对我还有我的家人的帮助和照顾. 一直非常内疚夏天的事情, 一辈子很长, 向着阳光前进; 黄伟, 感谢这些年的友谊, 我们继续赤道行走. 头儿, 愿你内心平静找到让自己开心的人, 事, 听从自己的内心.

Finally, I would like to thank the support from [redacted]. From my first day with [redacted] visiting [redacted], I have felt being home: warm, free and relaxed. Grown up as the only child in my own family, it is so great to have so many nice brothers and sisters “for free” (as my board game victims☺). I had also a great time with the big [redacted] family: how often you meet and how close you are, remind me of a Chinese family!!! 谢谢爸妈很多年来, 无论在如何艰苦 的生活环境下给予我教育的机会. 谢谢爷爷奶奶, 阿公一直对我的支持与关爱. 希望你们为我骄傲. [redacted], thank you for all your love and everything you have done. I am looking forward to new life experiences ahead of us.